ENHANCED FUNCTIONALITIES ACHIEVED BY A VERTICALLY ALIGNED NANOCOMPOSITE APPROACH

A Dissertation

by

WENRUI ZHANG

Submitted to the Office of Graduate and Professional Studies of
Texas A&M University
in partial fulfillment of the requirements for the degree of

DOCTOR OF PHILOSOPHY

Chair of Committee,	Haiyan Wang
Committee Members,	Hong Liang
	Tahir Cagin
	Xinghang Zhang
Head of Department,	Ibrahim Karaman

December 2015

Major Subject: Materials Science and Engineering

ABSTRACT

Vertically aligned nanocomposite (VAN) thin films have emerged as a new thin-film platform which is composed of at least one strongly correlated metal oxide coupled with another synergistically selected oxide. Self-assembled, heteroepitaxial VAN films form as a consequence of several key attributes, including the growth kinetics, thermodynamic stability, crystal chemistry and thin film epitaxial constraint. The VAN films have exhibited various morphologies depending on specific material system and growth parameters, such as nanomaze, nanocheckerboard, and vertical nanopillars embedded in a planar matrix. Owing to tunable vertical lattice strain and novel interface coupling, the VAN films have been exploited as a very effective platform for enhancing physical properties and exploring novel functionalities.

In this dissertation, we have achieved highly textured growth of $La_{0.7}Sr_{0.3}MnO_3$:ZnO (LSMO:ZnO) VAN film on the semiconductor silicon substrate with a $SrTiO_3$ (STO)/TiN bilayer buffer. By tuning the film composition and associated spin-dependent tunneling and scattering across the structural boundaries, we have demonstrated enhanced and tunable low-field magnetoresistance (LFMR) effects.

Different interface couplings between ferromagnetic (or ferrimagnetic)-antiferromagnetic (FM-AFM) spins have been created in the VAN structure. $BiFeO_3$ (BFO) has been selected as the AFM, while $CoFe_2O_4$ (CFO) and LSMO have been selected as the ferrimagnet and ferromagnet, respectively. Either rotatable or pinned AFM spins have been formed at the vertical interfacial region of BFO:CFO and

BFO:LSMO VAN film, respectively. As a result, enhanced perpendicular magnetic anisotropy and perpendicular magnetic exchange bias have been achieved from these two interface couplings, respectively. The magnetic exchange coupling at the vertical interfaces in the VAN architecture has been exploited to explore a novel way to control the magnetotransport property in VAN films. FM LSMO and AFM NiO have been selected to form the vertical FM-AFM exchange coupling in the prepared VAN architecture. A dynamic and reversible switch of the resistivity between two distinct exchange biased states has been achieved through a field cooling procedure with a magnetic field bias.

Using BFO:CFO VAN films as a model system, we demonstrate an effective method to modulate the vertical heterointerface and the morphology of nanocomposite films by adjusting the laser repetition frequency during deposition. Both vertical and gradient interfaces have been obtained through the film thickness, which strongly correlates with strain tuning and interface coupling, and thus modifies the magnetic anisotropy, coercive fields and FE switching behavior.

The studies in this dissertation demonstrate several examples of enhanced performance using the benefits of the unique VAN architecture. The huge vertical interfacial area for functional coupling and the effective vertical strain control independent of the substrate in the VAN films, as well as the simple self-assembly, provide a new dimension to tune the properties of metal oxides.

DEDICATION

To my parents, my sister and my wife

ACKNOWLEDGEMENTS

I would like to express my deepest appreciation to my advisor, Dr. Haiyan Wang, for her great care and professional guidance during my Ph.D. study. I benefited a lot from her insightful mind, highly passionate research attitude, and solid knowledge background. She always encourages me to pursue high quality research and provides us a very supportive research environment to explore new fields and deepen the understanding of our research topics. Her hard-work style also impresses me a lot and convinces me that it is something that should be kept not only in our Ph.D. study, but also in our future career. I feel so grateful and lucky for the precious training opportunity under her supervision during my Ph.D. study.

I want to thank my committee members, Dr. Hong Liang, Dr. Tahir Cagin, and Dr. Xinghang Zhang for their great help and continuous attention on my research. I also thank Dr. Andreas Holzenburg for his excellent classes of Transmission Electron Microscopy. I would like to acknowledge help from Dr. Wilson Serem and Dr. Jing Wu at Materials Characterization Facility on materials characterization and measurements.

Special appreciation goes to our collaborators Dr. Judith Driscoll at University of Cambridge and Dr. Quanxi Jia at Los Alamos National Lab for fruitful discussion and great suggestions. I have learned a lot from the exciting collaboration with them.

I would like to thank all my colleagues for their teaching, help and fruitful discussions: Dr. Aiping Chen, Dr. Joon-Hwan Lee, Dr. Chen-Fong Tsai, Dr. Yuanyuan

Zhu, Dr. Li Chen, Dr. Qing Su, Dr. Fauzia Khatkhatay, Dr. Liang Jiao, Jie Jian, Clement Jacob, Leigang Li, Meng Fan, Jijie Huang and Han Wang.

Finally, I want to thank my parents for their love, care and encouragement. I also want to thank my sister for the continuous encouragement and support. I want to thank my wife, Chengyan Yang for her love and care. I would never achieve this much without their care, support and encouragement.

NOMENCLATURE

AC	Alternative current
AFM	Antiferromagnetic
AMR	Anisotropic magnetoresistance
BSE	Back-scattered electron
CMR	Colossal magnetoresistance
CVD	Chemical vapor deposition
DC	Direct current
DE	Double exchange
DME	Domain matching epitaxy
EB	Exchange bias
EDX	Energy dispersive X-ray
FC	Field cooling
FE	Ferroelectric
FM	Ferromagnetic
GMR	Giant magnetoresistance
HAADF	High angle annular dark field
IP	In-plane
LFMR	Low-field magnetoresistance
MBE	Molecular beam epitaxy
ME	Magnetoelectric

MR	Magnetoresistance
MTJ	Magnetic tunnel junction
OP	Out-of-plane
PEB	Perpendicular exchange bias
PFM	Piezoelectric force microscopy
PLD	Pulsed laser deposition
PM	Paramagnetic
PMA	Perpendicular magnetic anisotropy
PPMS	Physical property measurement system
PVD	Physical vapor deposition
R_a	Root mean square roughness
RSM	Reciprocal space map
SE	Secondary electron
SEM	Scanning electron microscopy
STEM	Scanning transmission electron
T_c	Curie temperature (ferromagnetic or ferroelectric)
TEM	Transmission electron microscopy
TMR	Tunnel magnetoresistance
VAN	Vertically aligned nanocomposites
VSM	Vibrating sample magnetometer
ZFC	Zero field cooling

TABLE OF CONTENTS

Page

LIST OF FIGURES

Page

LIST OF TABLES

Page

CHAPTER I

INTRODUCTION

This chapter presents the research background, motivation and objectives of the research in this dissertation. Heteroepitaxial vertically aligned nanocomposite (VAN) oxide thin films have emerged as a new platform to explore enhanced or novel functionalities, which have attracted increasing research interests. In this chapter, a short overview on the crystal structure and functionalities of complex oxides are introduced first. Detailed introduction of functionalities is followed, which includes magnetoresistance (MR), magnetic anisotropy, exchange bias, ferroelectric and multiferroic properties. Last, strain engineering on functional oxide thin films and research work on VAN have been reviewed, before proposing future directions.

1.1 Functional oxide thin films

1.1.1 Overview of functional oxides

Oxide materials have become smart functional materials beyond their traditional roles as dielectric and structure materials. They have exhibited a wide variety of emerging functionalities ranging from magnetic, electric, optical, thermal properties as well as fascinating multifunctionalities. Driven by the advancement of materials fabrication methods and microstructure characterization techniques, the study on function oxides has been boosted with a better control from microstructure, chemical composition and ultimate physical properties. Complex functional oxides provide an ideal playground for exploring the interplay among the fundamental degrees of freedom:

structural (lattice), electronic (orbital and charge), and magnetic (spin). In the past decades, a wide range of complex oxides have been studied and completely unexpected phenomena, including high-temperature superconductivity,[1] magnetoelectrics (MEs),[2] MR,[3] thermoelectrics [4] and ionic effects,[5] have been reported.

1.1.2 Functional oxide thin films

The study of functional oxides in conventional bulk materials has already achieved significant progress by tuning the phase composition and microstructure for enhanced functionalities. The development of advanced thin film growth techniques allows more flexible control of microstructures in the form of epitaxial films, multilayers, superlattices and vertically aligned nanocomposite films, which represents a significant step forward in the study of functional oxides.[6-9] The thin film epitaxy offers a powerful pathway for exploration and stabilization of new states of matters or enhanced functionalities that are difficult to be accessed in conventional bulk materials even in a single-crystal form. One highly topical example that has been widely explored is the polar interface in $LaAlO_3/SrTiO_3$ (LAO/STO) heterostructures.[7] A highly conducting two-dimensional electron gas is formed at the interface between two insulators, which exhibits great potential for high-frequency transistors. Another important example is the significantly larger ferroelectric (FE) polarization stabilized in epitaxial $BiFeO_3$ (BFO) film, which shows almost an order of magnitude higher than that of the bulk counterparts.[8]

1.1.3 Crystal structure of functional oxides

Transition metal oxides have been most commonly studied because the strong interplay between structure, chemistry and physics provides powerful ways for exploration of novel phenomena and enhanced functionalities. The change of the crystal structure, coordination or bonding types may enable the evolution of electronic structure and the physical properties. In general, transition metal oxides can be categorized into binary, ternary and more complex derived oxides. Materials in this category are mostly used in dielectric, optoelectronic and memristor devices. Common binary oxide structures include Rock Salt, Wurtzite, Fluorite, Rutile and Corundum. Specific examples are listed in Table 1.1. Common ternary oxide structures include ilmenite, spinel, perovskite and perovskite derived structures such as Ruddlesden-Popper phases, Aurivillius phases and Dion-Jacobson phases. Figure 1.1 shows the crystal models of the above structures.[9,10]

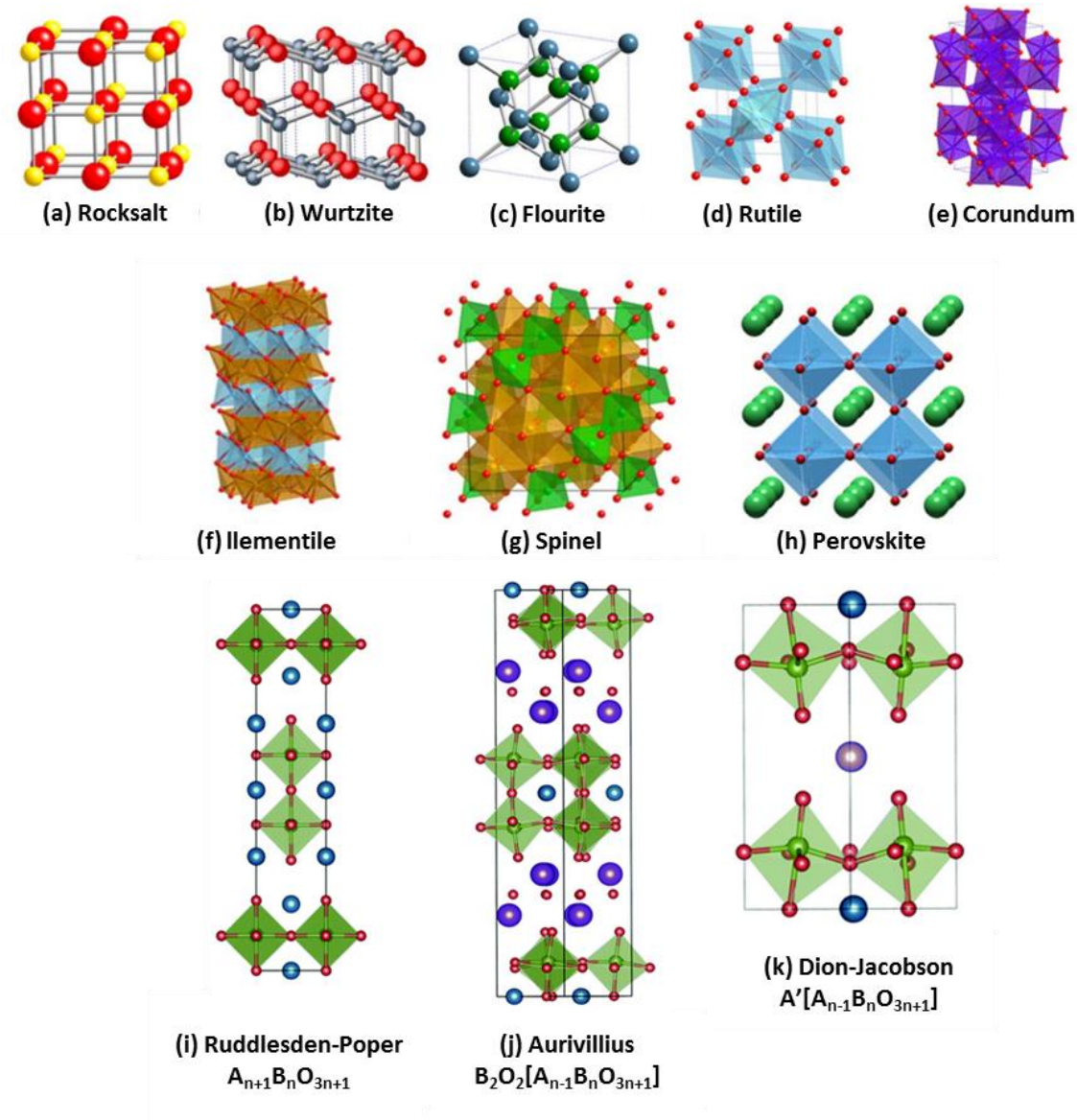

Figure 1.1. Schematic illustrations of binary, ternary and layered oxide crystal structures.[9,10]

Table 1.1. Category of common binary, ternary and layered oxides

System	Crystal Structure	Representative oxides
Binary oxides	Rock salt	MgO, MnO, Eu_2O_3, Sm_2O_3, Nd_2O_3, ZrO, CoO, NiO, VO, TiO
	Fluorite	CeO_2, ZrO_2,PrO_2,TbO_2,
	Cuprite	Cu_2O, Ag_2O, Pb_2O
	Rutile	TiO_2, IrO_2, MoO_2, RuO_2, SnO_2, WO_2, β-MnO_2
	Corundum	Al_2O_3, V_2O_3, Cr_2O_3, α-Fe_2O_3
	Wurtzite	ZnO, BeO
	Antifluorite	Li_2O, Na_2O, K_2O, Rb_2O
Ternary oxides	llmenite	$MTiO_3$ (M= Co, Ni, Fe, Mn), $NiMnO_3$, $CoMnO_3$, $LiNbO_3$
	Perovskite	$SrTiO_3$, $BaTiO_3$, $LaMnO_3$, $La_xSr_{1-x}MnO_3$, $BiFeO_3$, $SrRuO_3$, $CaTiO_3$,$BaZrO_3$
	Spinel	MFe_2O_4 (M=Co, Ni, Fe, Mn), $MgAl_2O_4$, $LiTi_2O_4$
Layered oxides	Layered perovskites	$YBa_2Cu_3O_{7-x}$
	Ruddlesden-popper series	$A_{n+1}B_nO_{3n+1}$ (n = 1, 2, … ∞) (Sr_2RuO_4, $Sr_3Ti_2O_7$)
	Aurivillius phases	$[Bi_2O_2]$-$[A_{n-1}B_2O_7]$ (Bi_2WO_6, Bi_3TiNbO_9)
	Dion-Jacobson	$A[A_{n-1}B_nO_{3n+1}]$ ($KLaNb_2O_7$, $CsLaNb_2O_7$)

Among the above oxides, BFO is one of the most widely studied functional oxides because of its room-temperature magnetic and strong FE properties.[6] It is also one of the main material systems studied in this thesis. With the development of material

synthesis techniques for high-quality samples, BFO, either in thin film or single crystal, exhibits a large remanent polarization of 60 μC cm^{-2} along [001] and 100 μC cm^{-2} along [111] directions. The room temperature phase of bulk BFO is rhombohedral with a point group of *R3c* (Figure 1.2(a)). It can be described as a distorted perovskite with a lattice constant of 5.63 Å and a rhombohedral angle of 59.35°. In thin film, the structure is distorted into a tetragonal structure based on the cubic phase with a lowered symmetry of P4mm (Figure 1.2(b)).[8] The pseudocubic lattice parameter is 3.960 Å. In epitaxial compressively-strained films, BFO undergoes a structural transition from monoclinic to tetragonal, as seen from BFO films grown on $LaAlO_3$ and $YAlO_3$ substrates. For magnetic properties at room temperature, BFO is a G-type antiferromagnet with each Fe^{3+} spin surrounded by six nearest antiparallel spins. The magnetic Neel temperature is 643 K. The antiferromagnetic spins are aligned in a long-range spin cycloid superstructure along a [110] propagation vector with a repeatable distance of 62-64 nm. The AFM spins are completely cancelled out in the cycloid, yielding miniscule magnetization at room temperature.

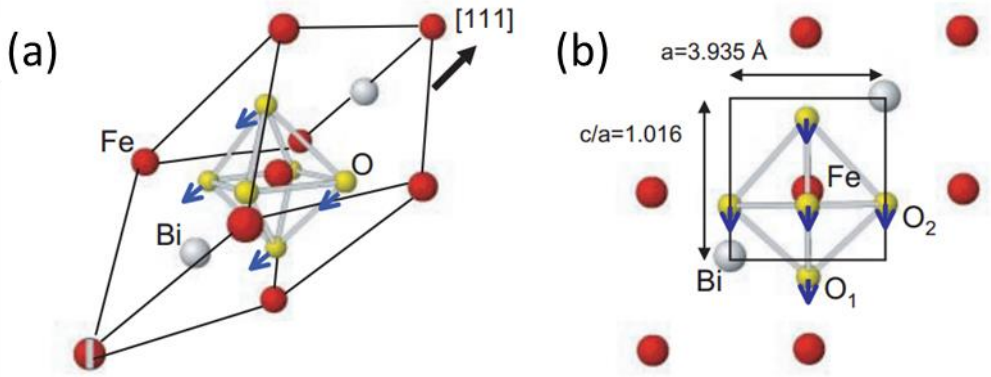

Figure 1.2. Schematic crystal models of (a) rhombohedral and (b) tetragonal $BiFeO_3$ unit cell.[8]

Manganites are another important class of oxides in the form of $RE_{1-x}AE_xMnO_3$, where RE is the trivalent rare earth cation (La, Pr, Sm, Nd) and AE is the divalent alkaline earth cation (Sr, Ca, Ba).[3] In $La_{1-x}Sr_xMnO_3$, three distinct ground states are observed depending on Sr doping. The perovskite $LaMnO_3$ is a representative parent compound of lanthanum manganites, which is antiferromagnetic insulator at room temperature. The spin-canted insulator is present for $x < 0.1$, which is followed by a ferromagnetic insulator for $0.10<x<0.17$. At the threshold value of 0.175, there is an orthorhombic to rhombohedral transition, which also couples with a magnetic phase transition and gives rise to a ferromagnetic metal phase, which is accompanied with a sharp drop in resistivity near the transition temperature. As x increases up to 0.3, the ferromagnetic phase increases sharply and then saturates after that value. The ferromagnetic behavior in mixed valence manganite compound can be explained by a double exchange (DE) model proposed by Zener in 1951,[11] which describes that the existence of Mn^{3+}-O-Mn^{4+} interaction in doped manganites favors electrons

delocalization and ferromagnetic alignment of magnetic spins for a more energetically stable state. The 30 mol% doping of Sr in $LaMnO_3$, the so-called $La_{0.7}Sr_{0.3}MnO_3$ (LSMO), is the optimized condition for largest DE interaction, which shows highest Curie temperature (T_c) of ~350 K and very high spin polarization of almost 100 %. The pseudocubic lattice parameter of LSMO is 3.870 Å.

$CoFe_2O_4$ (CFO) belongs to the spinel family with a general formula of AB_2X_4, where A and B are cations (Fe, Co, Ni, Mn, Cr, Al), and X is an anion (O, S). It has an inverse spinel structure and a bulk lattice parameter of 8.392 Å. The tetragonal sites are occupied by Fe cations and octahedral sites by both Fe and Co cations. CFO is a room temperature ferrimagnetic insulator with a Curie temperature of 793 K. The ferrimagnetic ordering in CFO can be understood by Neel's two sub-lattice model,[12] where two internal Weiss fields are assigned to A and B sublattices, respectively. The total magnetization comes from a sum of exchange interactions between A-A, B-B and A-B sites. CFO has a room-temperature saturate magnetization of 350 emu/cm^3, magnetocrystalline anisotropy of (~2 $\times 10^6$ erg/cm^3) and magnetostrictive coefficient of ($\lambda_{001}=3.50\times10^6$).

1.1.4 Epitaxial growth of oxide thin films

The exploration of functional oxides has largely been driven by the advancement of new growth and characterization techniques. The new development of thin film deposition techniques provides more accessible routes to explore and stabilize non-equilibrium, metastable, or new states of matters. Representative thin film fabrication

techniques include physical vapor deposition (PVD), chemical vapor deposition (CVD) and solution-based methods.

PVD techniques use the vacuum-based systems to deposit thin films by condensing a vaporized phase of desired thin film materials onto various substrates. They include molecular beam epitaxy (MBE), pulsed laser deposition (PLD), sputtering, e-beam physical vapor deposition, thermal evaporation. CVD techniques deposit thin films by chemical reactions of volatile precursors and surface absorptions of reacted products onto the substrate surface. They include aerosol-assisted CVD, plasma-enhanced CVD, atomic-layer CVD, metal organic CVD and others. Solution-based growth methods include liquid phase epitaxy, sol-gel method and polymer assisted deposition.

The thin film growth process can be described by three modes: Volmer-Weber or island growth, Frank-Van der Merwe or layer-by-layer growth and Stranski-Krastanov growth.[9] The island growth usually occurs between dissimilar materials, where the smallest stable thin film clusters nucleate on the substrate and grow into island features. The layer-by-layer growth occurs when the deposited atoms or molecules form two-dimensional sheets continuously on the substrate, which is typically seen in epitaxial growth of semiconductors and oxide materials. Stranski-Krastanov growth is a combination of the Volmer-Weber growth and Frank-Van der Merwe growth, which is more common in the growth of metal-metal and metal-semiconductor systems.

Despite the different growth process, the fundamental growth mechanism can be described with thermodynamic models for the nucleation and growth process. Figure 1.3

shows a schematic model of the atomistic nucleation process of adatoms on the substrate surface during film growth.[9] The equilibrium among the horizontal components of the interfacial tension between the component phases yields Young's equation:

$$\gamma_{sv} = \gamma_{fs} + \gamma_{fs} cos\theta, \tag{1.1}$$

where γ is the interfacial energy, subscripts *s*, *f*, and *v* represent substrate, film and vapor, respectively, and θ is the wetting angle. For island growth, $\theta > 0$, and $\gamma_{sv} < \gamma_{fs} + \gamma_{fs}$, which suggests island growth since surface extension of the film exceeds that of the substrate. For layer-by-layer growth, $\theta > 0$, and $\gamma_{sv} \geq \gamma_{fs} + \gamma_{fs}$, which favors a complete wet of film materials on the substrate and achieves the layer-by-layer stacking. For Stranski-Krastanov growth, the film growth initially follows a layer-by-layer stacking until the substrate-induced strain energy becomes large enough to trigger the island growth typically after 5-6 monolayers.

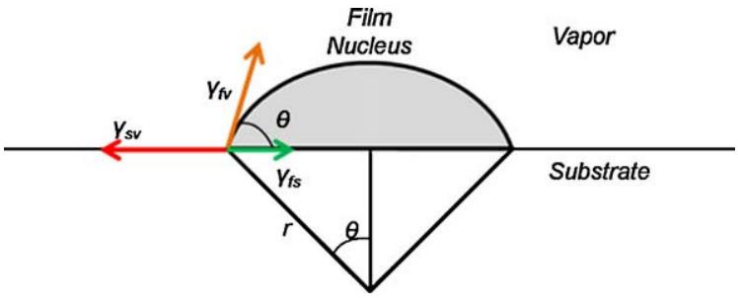

Figure 1.3. Schematic model of the atomistic nucleation process on a substrate surface during film growth.[9]

In the film-on-substrate geometry, thin film growth depends strongly on the nucleation process and growth environment. There are a number of factors that can be used to control the film growth, which includes substrate structures like substrate orientation, crystal structure and lattice parameter, substrate surface defects like step edges, defects, seed layers, growth kinetic factors like the rate of adatom arrival, growth temperature and pressure. These provide the most common ways for researchers to achieve the desired level of film growth.

1.2 Functionalities in complex oxide thin films

1.2.1 Magnetoresistance

MR is the property of a material to change its electric resistivity when an external magnetic field is applied to it. Since its first discovery in 1856 by Thomson,[13] the MR effect has been widely used in commercial magnetic storage devices and sensors. So far, several important types of MR effects have been observed and studies depending on materials systems, geometries and structures, which include giant magnetoresistance (GMR) effect, tunneling magnetoresistance (TMR), anisotropic magnetoresistance (AMR), colossal magnetoresistance (CMR) and LFMR. These MR effects have been discussed in more detailed in the following sections.

1.2.1.1 Giant magnetoresistance

The GMR effect was first discovered by A. Fert and his co-workers in 1988 in the study of Fe/Cr multilayers.[14] Almost at the same time, P. Grünberg reported similar effect in Fe/Cr/Fe trilayers.[15] The key structure consists of ferromagnetic layers separated by a thin non-magnetic metal. The spin alignment in two neighboring

ferromagnetic layers can be tuned independently because of the non-magnetic spacing, as shown in Figure 1.4(a) and (b).[16] The GMR effect can be understood spin-dependent scattering effect, which is explained qualitatively based on a two-fluid mode of the electron conduction in the multilayer structures.[17] In brief, conduction electrons can be divided into two classes: electrons with spin parallel to the local magnetization, and ones with antiparallel spin. When the magnetization direction of two neighboring FM metal layers changes, two different resistance states are observed, where $R_{\uparrow\downarrow}$ is the electric resistance in the antiparallel state and $R_{\uparrow\uparrow}$ is the resistance in the parallel state. The GMR is calculated by

$$\mathrm{GMR} = \frac{R_{\uparrow\downarrow} - R_{\uparrow\uparrow}}{R_{\uparrow\uparrow}} \times 100\ \% \tag{1.2}$$

The observation of the GMR effect requires the change of spin alignment in neighboring FM layers and the non-magnetic spacing thickness no less than the mean free path of electrons. By tuning the thickness of the spacing layer, large GMR values up to 80 % have been observed in Fe (3 nm)/Cr(0.9 nm) multilayer measured at 4.2 K, as shown in Figure 1.4(c).[15] Recent studies have observed the GMR effects in two different measurement geometries: current-perpendicular-to-plane (CPP) geometry and current-in-plane geometry, which correspond to the electric current flowing orthogonal to the layers and along the layers, respectively. The CPP geometry is more favorable to memory application, which allows higher device density integration.

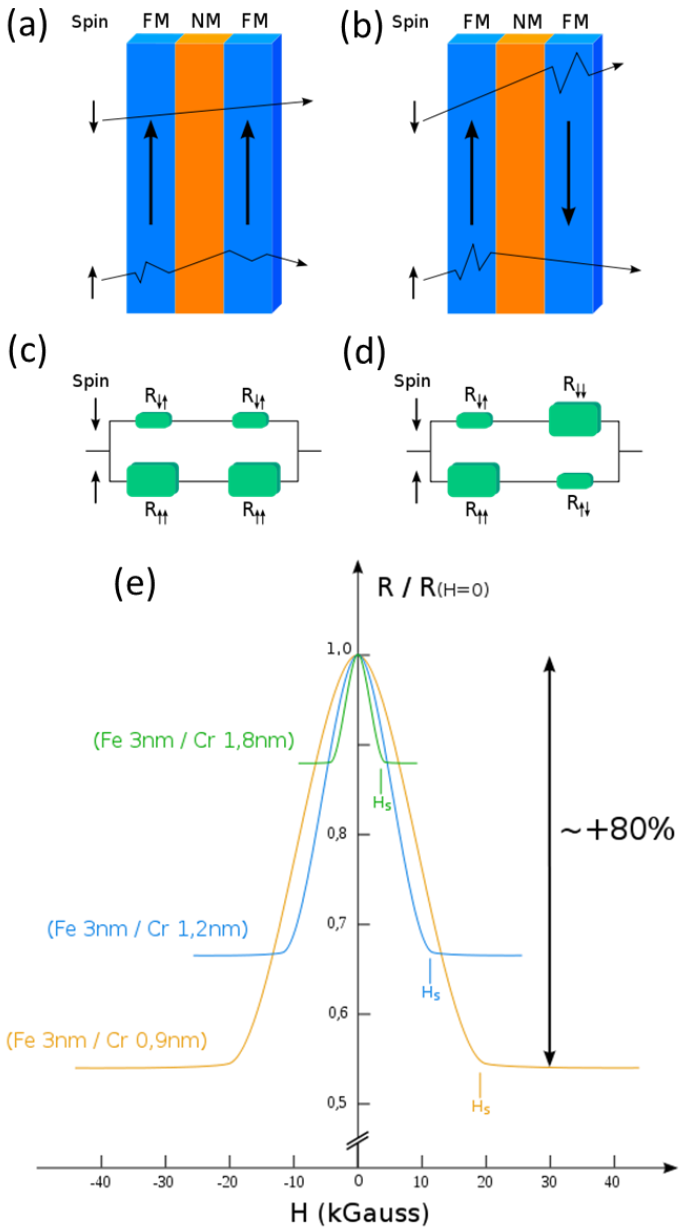

Figure 1.4. Schematic illustrations of electrons with up and down spins transport in FM/NM/FM structures with (a) parallel and (b) antiparallel spin alignment in two neighboring FM electrodes. (c) and (d) Corresponding equivalent circuits of the electron transport in the structures. (e) Normalized resistivity of Fe/Cr multilayers as a function of magnetic field measured at 4.2 K.[15,16]

1.2.1.2 Tunnel magnetoresistance

TMR occurs in multilayer structures consisting of two ferromagnetic materials (metal: Fe, Co, CoFe, CoFeB; oxide: LSMO, $La_{0.7}Ca_{0.3}MnO_3$(LCMO)) separated by an ultrathin insulating layer (~1-2 nm; MgO, Al_2O_3, STO), in which electrons can tunnel through the insulating barrier and conserve the spin under an applied electric field. Although this effect was proposed by Julliè re in 1975,[18] the first real application of TMR was realized till 1995 with the development of deposition and nanopatterning techniques.[19] Figure 1.5(a) shows the schematic illustration of the tunnel effect happened in the magnetic tunnel junction (MTJ) with parallel and antiparallel spin alignment in the adjacent ferromagnetic layers.[20] The tunnel resistance can be switched between two stable states by applying an external magnetic field, which yields a TMR ratio as

$$\mathrm{GMR} = \frac{R_{ap} - R_p}{R_p} \times 100\ \% \tag{1.3}$$

Where R_{ap} and R_p are the electric resistance in the antiparallel and parallel state, respectively. First MTJs used an amorphous Al_2O_3 layer as the tunnel barrier and a limit TMR ratio up to 70 % can be obtained at room temperature.[21] In later studies, the single-crystalline MgO layer has been demonstrated as a better tunnel barrier which actively selects symmetry states with high spin polarization and thus leads to significantly enhanced TMR effect. For example, a TMR ratio of 1010 % at 5 K and 500 % at room temperature have been observed in the $(Co_{25}Fe_{75})_{80}B_{20}$ (4 nm)/MgO (2.1 nm)/$(Co_{25}Fe_{75})_{80}B_{20}$ (4.3 nm) magnetic tunnel junction, as shown in Figure 1.5(b).[22] Recently, the record TMR ratio has further been improved over 600% at room

temperature for CoFeB/MgO/CoFeB MTJs with simple sputtering and annealing process have been reported.[23] The rapid development of MTJs indeed shows immediate impact on magnetic memory devices and TMR-based read heads have already been used in commercial devices (Figure 1.5(c)).[24]

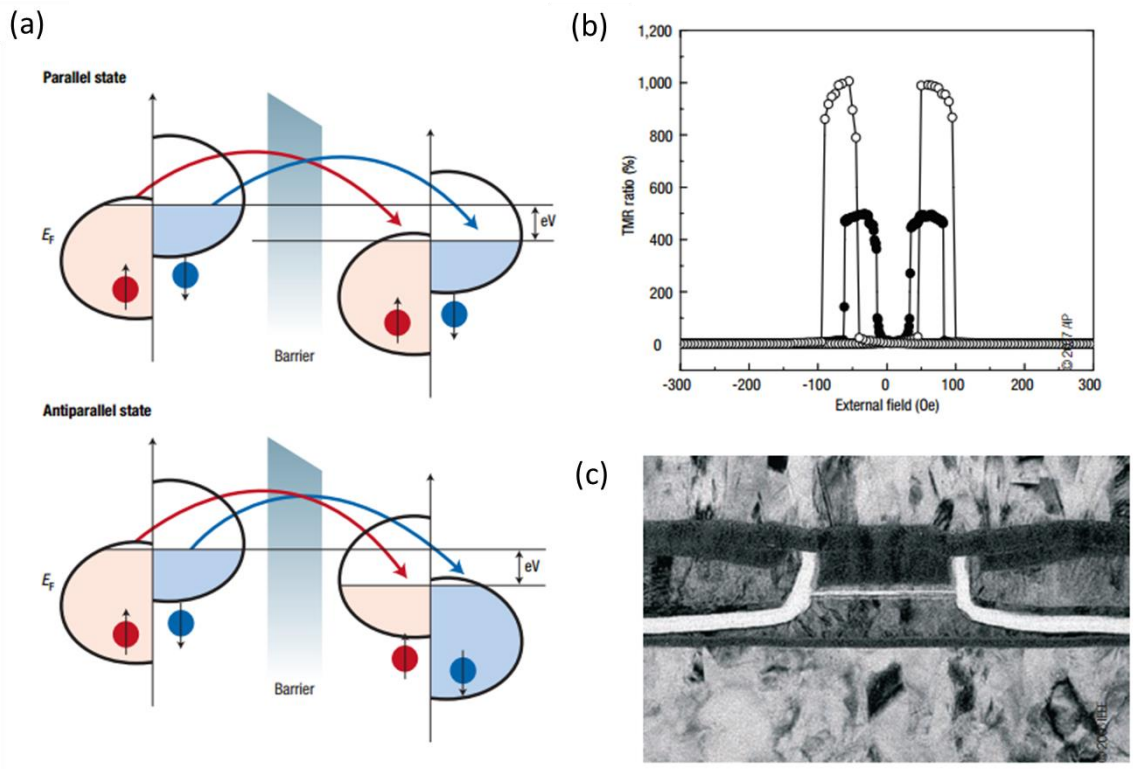

Figure 1.5. (a) Schematic illustrations of the tunnel magnetoresistance (TMR) in a typical structure of two ferromagnetic layers separated by a non-magnetic insulator layer.[20] (b) The TMR ratio of a $(Co_{25}Fe_{75})_{80}B_{20}$ (4 nm)/MgO (2.1 nm)/$(Co_{25}Fe_{75})_{80}B_{20}$ (4.3 nm) magnetic tunnel junction as a functional of external field measured at room temperature (filled circle) and 5 K (open circle).[22] (c) Cross-sectional TEM image of a commercial TMR read head.[24]

In parallel with increasing the TMR ratio, to enhance the perpendicular anisotropy in MTJs is necessary for achieving high-density magnetic memory application with high thermal stability and low critical current for current-induced magnetization switching.[25] Using interfacial perpendicular magnetic anisotropy, perpendicular MTJs based on conventional material system but with ultrathin CoFeB layer have been fabricated (Figures 1.6(a) and 1.6(b)).[26] The CoFeB/MgO-based MJTs have exhibited a perpendicular magnetic easy axis (Figures 1.6(c) and 1.6(d)), a high TMR ratio over 120 % and high thermal stability at a dimension as low as 40 nm (Figure 1.6(b)).

Recently, tunnel anisotropic magnetoresistance (TAMR) provides an alternative route to fabricate novel spintronic devices based on strong spin-orbital coupling. The TAMR effect relies on spin manipulation in a single magnetic electrode instead of the stringent requirements of controlling the relative spin directions of two or multiple magnetic electrodes in conventional spin valve devices.[27,28] A TAMR tunnel device consists of a thin tunnel barrier sandwiched by an AFM (in contact with a FM) and a non-magnetic electrode. By tuning the AFM moment with an external magnetic field, a 130 % spin-valve-like MR signal has been obtained in a NiFe/IrMn/MgO/Pt multilayer structure.[28]

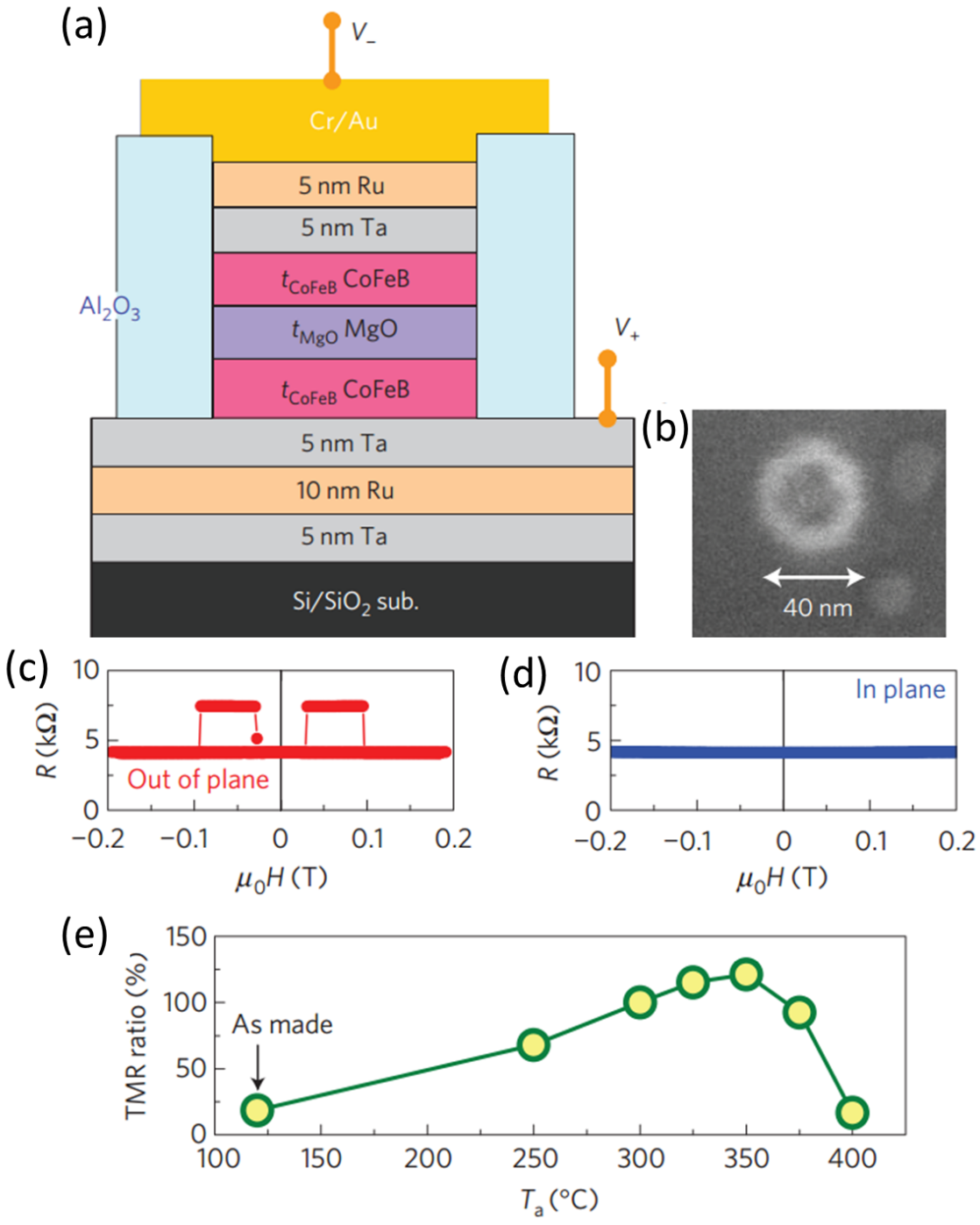

Figure 1.6. (a) Schematic of a CoFeB/MgO based MTJ device for TMR measurement. (b) Top view SEM image of a MTJ pillar. TMR curves for an annealed MTJ with (c) out-of-plane magnetic field and (d) in-plane magnetic field. (e) Anneal temperature dependence of TMR ratio.[26]

1.2.1.3 Colossal magnetoresistance

CMR is a MR effect associated with a ferromagnetic-to-paramagnetic (PM) phase transition. Near the phase transition temperature, large MR effect is observed, which involves rich physics phenomena and receives significant research interests in the field of condensed matter physics. Since its discovery in 1950 by Jonker and coworkers, much research efforts have been devoted to understand the fundamental physics,[29] which relates to a strong interplay among the spin, charge, orbital and lattice degrees of freedoms. In an ideal cubic perovskite structure, the five d orbitals of a free Mn ion undergo a crystal field splitting into a t_{2g} triplet (d_{xy}, d_{xz} and d_{yz}) and an e_g double ($d_{x^2-y^2}$, $d_{3z^2-r^2}$), as shown in Figure 1.7.[30] Due to tetragonal distortion of the MnO_6 octahedra, the degeneracy of the levels is further lifted, the so-called Jahn-Teller distortion,[31] which forms three lower-lying t_{2g} orbitals and two higher-lying e_g orbitals. Besides the Jahn-Teller distortion, another important origin to cause the lattice deformation relates to the tolerance factor (t) of a structure,[32] which is calculated as

$$t = \frac{r_B + r_O}{\sqrt{2}(r_A + r_O)} \ , \tag{1.4}$$

where r_i (i=A, B and O) represents the ionic sizes of each element.

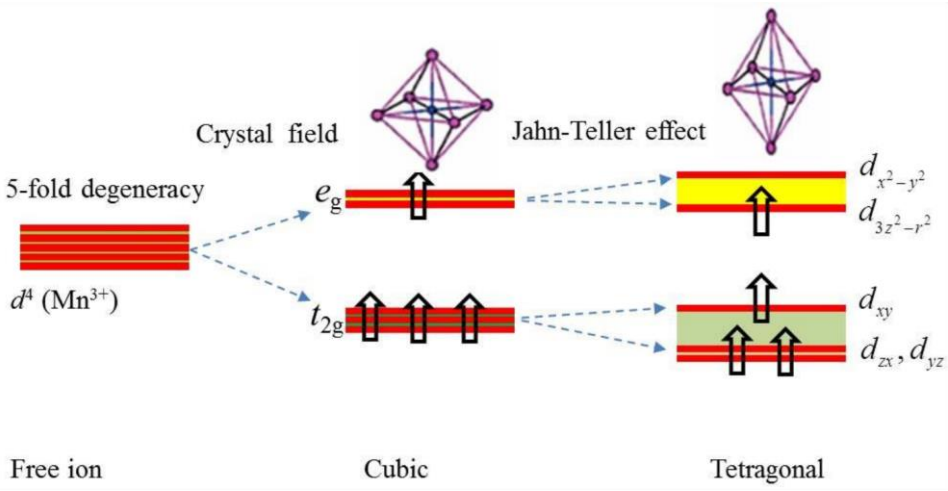

Figure 1.7. Schematics of crystal field splitting and Jahn-Teller effect on lift of the original fivefold degeneracy.

The parent $LaMnO_3$ is an antiferromagnetic insulator because of the antiferromagnetic coupling between Mn^{3+}-O-Mn^{3+} chain and strong electronic repulsion. When doped with Ca or Sr in La sites, the valence states of Mn ions become a mixture of Mn^{3+} (with three t_{2g} and one e_g electrons) and Mn^{4+} (with three t_{2g} electrons only).[33] The hopping of e_g electrons from Mn^{3+} to Mn^{4+} is the basic mechanism for the conduction behavior and the ferromagnetic coupling in doped manganites, which is governed by double exchange (DE) interaction (the simultaneous jumps of the e_g electron of Mn^{3+} to O p-orbital and the electron with the same spin form O p-orbital to the empty e_g orbital of Mn^{4+}).[10,34] The electron hopping probability varies as the cosine of angle (θ) between two spins in neighboring e_g orbitals, which allows larger mobile electron transfer at a lower θ.[35] The external magnetic field aligns the core spins in a higher order from a pristine disorder states and facilities the electron hopping, thus leading to a drop in

resistivity. The largest CMR usually occurs near T_c because this effect is strengthened by the field-induced magnetic phase transition.

Doped manganites have exhibited a rich phase diagram as a function of dopant concentration, as shown in the example of Ca doped $LaMnO_3$ in Figure 1.8(a).[36] A thousandfold resistivity change has been observed in this material system (Figure 1.8(b)), which makes the CMR effect very interesting both for fundamental physics and possible applications.[37] A comprehensive understanding of such effect requires continuous research efforts in clarifying the synergic contribution of DE interaction, Jahn-Teller distortion, super-exchange interaction and Hund's coupling. Recent research effort trying to quantitatively explain the observed resistivity change suggests the important role of the electron-phonon interaction besides the DE interaction.[3] There are other oxides including $Tl_2Mn_2O_7$ with no mixed valence in Mn ion, and thus cannot be explained with DE interaction and Jahn-Teller distortion.[38] The observed CMR effect in such oxides may be attributed from usually large incoherent scattering from spin fluctuations accompanied with the magnetic phase transition.[39] Research efforts are still needed for a full understanding of the basic mechanism.

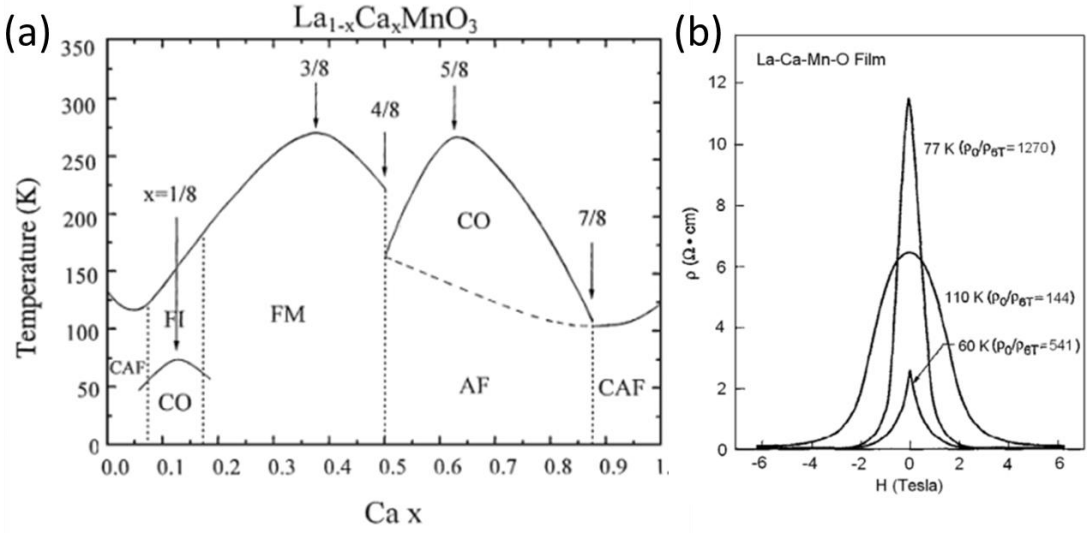

Figure 1.8. (a) Magnetic and electronic phase diagram of $La_{1-x}Ca_xMnO_3$. The various states are ferromagnetic insulating (FI), ferromagnetic (FM), canted antiferromagnetic (CAF) and charge-ordered (CO). (b) Magnetic field dependence of resistivity of $La_{0.67}Ca_{0.33}MnO_3$ thin film measured at different temperatures.[36,37]

1.2.1.4 Low-field magnetoresistance

LFMR describes the property that shows a large MR effect at a low magnetic field. It can be calculated as

$$\text{LFMR} = \frac{R_0 - R_H}{R_0} \times 100\ \%, \tag{1.5}$$

Where R_0 and R_H represent the resistance measured under a zero and a non-zero magnetic field. The LFMR mainly relies on extrinsic transport effect and is increased by spin-polarized tunneling through electronic barrier across structural disorders such as grain boundaries and phase boundaries.[40,41] Thus a variety of work to enhance the LFMR effect has been done by creating artificial boundaries in polycrystalline films or introducing secondary phases in nanocomposite films. Representative studies in this

aspect include the growth of $La_{0.7}Ca_{0.3}MnO_3$ (LCMO) films on bicrystal substrates,[42] the creation of artificial boundaries in nanopatterned devices,[43] and LSMO or LCMO-based nanocomposite thin films.[44,45]

1.2.2 Magnetic anisotropy

Magnetic anisotropy describes the directional dependence of a material's magnetic property like magnetic susceptibility. It strongly affects the shape of magnetic hysteresis (M(H)) loop and has a wide application in commercial magnetic memory devices. Figure 1.9 shows representative Out-of-plane (OP) and in-plane (IP) M(H) loops of a $BFO_{0.67}$:$CFO_{0.33}$ VAN film.[46] Three parameters are usually used for a quantitative characterization of magnetic anisotropy, which are saturate magnetization (M_s), remanent magnetization (M_r) and coercive field (H_c). A perpendicular magnetic easy axis is observed from the square shape of the OP M(H) curve, which shows larger M_r/M_s ratio and H_c values. There are several important sources of magnetic anisotropy, which include magnetocrystalline anisotropy, shape anisotropy, stress anisotropy and exchange anisotropy. Only the magnetocrystalline anisotropy is an intrinsic property of a material, which relates to the crystal structure of the materials.[47] Extrinsic anisotropies are introduced by the shape, external stress and interface exchange coupling.[48]

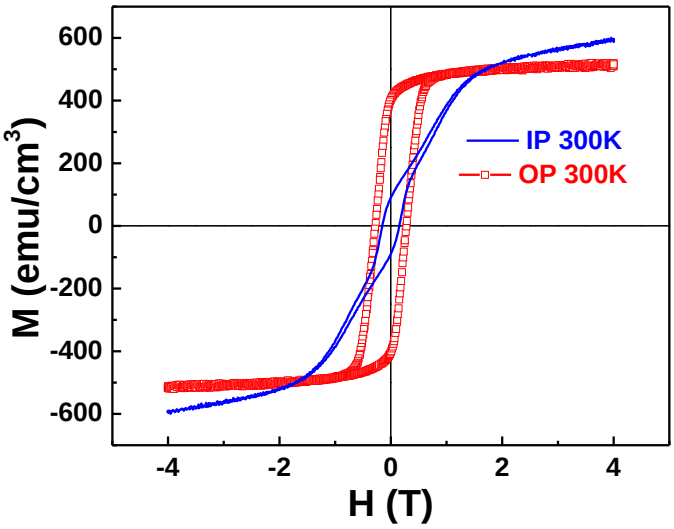

Figure 1.9. Out-of-plane and in-plane magnetic hysteresis loop of a $BFO_{0.67}$:$CFO_{0.33}$ VAN film measured at 300 K.[46]

1.2.2.1 Magnetocrystalline anisotropy

Magnetocrystalline anisotropy describes the energy required to deflect the magnetization in a single crystal from an easy direction to a hard direction. The formation of the magnetically easy axis results primarily from the spin-orbit interaction, which depends strongly on the spatial configuration of cations and anions. When an external magnetic field is applied to rotate the spin of an electron, the coupling between spin and orbit resists the spin rotation and generates the crystal anisotropy energy. The magnetic easy axis varies in different material systems and crystal structures. For example, in body-center-cubic Fe, the easy axis is [100] and the hard axis is [111]. In face-center-cubic Ni, the [111] is the easy axis with the [100] as the hard axis. In a cubic system, the magnetocrystalline anisotropy energy (K_m) can be calculated as

$$K_m = K_0 + K_1(\alpha_1^2\alpha_2^2 + \alpha_2^2\alpha_3^2 + \alpha_3^2\alpha_1^2) + K_2(\alpha_1^2\alpha_2^2\alpha_3^2) + \cdots, \qquad (1.6)$$

where K_0, K_1, K_2… are constants associated with specific materials at a given temperature, $\alpha_1, \alpha_2, \alpha_3$ are the consines of the angle between Ms and a, b, c axis in the cubic crystal, respectively.[49] The CFO in this study has a large K_m of 2.0×10^5 J/m^3,[50] which is so-called hard ferrimagnet. The LSMO is a soft ferromagnet with a K_m of 1.6×10^3 J/m^3.[51]

1.2.2.2 Shape anisotropy

The shape anisotropy results from dipole-dipole interactions in ferromagnet/ferrimagnet.[52] It is described by the demagnetization tensor N, which is the magnetic field within a magnetic body produced by the intrinsic magnetic moments. For a homogeneous magnetic film, the shape anisotropy contributes to an in-plane easy axis. The shape anisotropy energy (K_s) is calculated as

$$K_s = -2\pi M^2, \tag{1.7}$$

where M is the saturate magnetization.[53] For a cylinder structure, its shape anisotropy (K_s) favors a perpendicular easy axis. K_s is calculated as

$$K_s = -2\pi(N_x - N_z)M_s^2, \tag{1.8}$$

where N_x and N_z are the demagnetization tensors, and $N_x = (1 - N_z)/2$.[54]

1.2.2.3 Stress anisotropy

Stress anisotropy occurs in magnetostrictive materials, which changes the dimension under a magnetic field. All pure substrates exhibit the magnetostrictive effect but with different magnitudes. The inverse magnetostrictive effect, which is the change of magnetic properties by applying a stress, is commonly used to incorporate stress

anisotropy (or magnetoelastic anisotropy) to tune the magnetic properties. The magnetoelastic energy (K_{me}) is estimated by

$$K_{me} = -\frac{3}{2} \times \lambda_{001} \times \mathrm{Y} \times \varepsilon_{001}, \quad (1.9)$$

where λ_{001} is the magnetostrictive coefficient, Y is the Young's modulus, and ε_{001} is the strain of the material.[55]

1.2.2.4 Exchange anisotropy

Exchange anisotropy is caused by the spin interaction between FM and AFM across their interface. Based on a microscopic Heisenberg model, frustrated FM spins tends to align perpendicular to the AFM easy axis and form spin-flop coupling.[56] For a flat interface, this coupling does not yield a unidirectional anisotropy and the associated exchange bias (EB) effect. Instead, it gives rise to uniaxial anisotropy which in turn causes enhanced H_c and changes the shape of M(H) curve. The calculation of exchange anisotropy energy based on current models always yields much higher values than the practical ones, which depend strongly on the properties of FM, AFM materials and their interface structure, such as the AFM anisotropy energy, spin canting, interface roughness, dislocation density and so on.[57,58]

1.2.3 Exchange bias

1.2.3.1 Overview of EB

Since its early discovery by Meiklejohn and Bean in 1956,[59] EB has received significant research interests because of the rich physics inside and the core application in magnetic memory applications. EB usually occurs at the interface of a FM in contact with an AFM material. When such FM-AFM interface is cooled through the Néel

temperature of the AFM, a unidirectional anisotropy is introduced along the direction of pinned AFM spins, which is characterized by a shift of the magnetic hysteresis loop along the field axis.[60] Figure 1.10 shows a schematic mode of EB, which give an intuitive picture for the EB occurrence as a result of the FM-AFM interface coupling.[61] In brief, when the magnetic field is applied along the same direction with major AFM interface spins, FM spins are easily aligned aided by the exchange coupling under a relatively small field (i). As the field reverses, the interfacial AFM spins exert a blocking torque on FM spin rotation until the field becomes large enough to overcome the microscopic torque (ii). The difference between the initial and reversed fields leads to the bias field observed in their magnetization curves. The same 'aid and drag' effect on FM spins happens when the field is reversed ((iii) and (iv)).

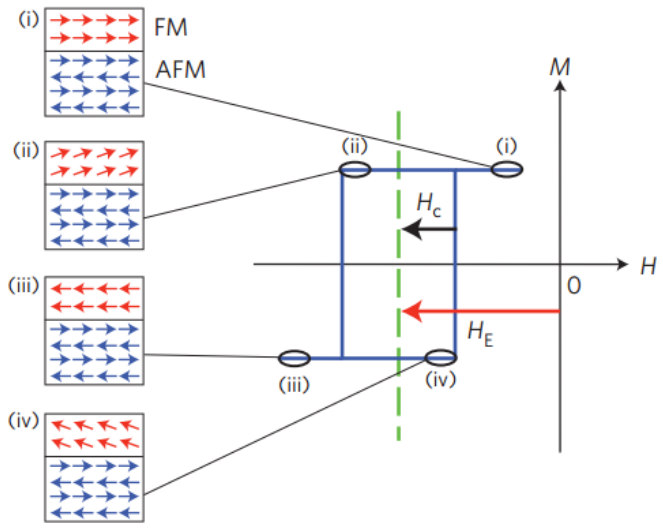

Figure 1.10. Schematic mode of exchange bias.[61]

The increased H_c and the bias shift (the so-called exchange bias field, H_{EB}) are two prominent features of the EB effect. Because FM spins can be "pinned" by AFM spins, this effect has been widely used in device applications that need manipulate the relative spin directions in neighboring layers such as spin valves.[62] So far, EB has been studied in a variety of FM-AFM coupled systems in the form of bulk, nanoparticles, polycrystalline nanocomposites, bilayer or multilayer thin films.[63] Different theory models have been proposed to quantitatively understand the relationship of H_{EB} and the interface coupling. Different assumptions have been made, ranging from ideal interface, interfacial AFM domain wall formation, random field model, spin-flop perpendicular interfacial coupling and uncompensated interfacial AFM spins due to interface roughness or reconstruction.[64,65] Here we discuss the first simple mode which examines the exchange coupling across an ideal interface.[66,67] The H_{EB} is estimated as

$$H_{EB} = \frac{\Delta\sigma}{M_{FM}t_{FM}} = \frac{2J_{ex}S_{FM}\cdot S_{AFM}}{a^2 M_{FM}t_{FM}}, \tag{1.10}$$

where $\Delta\sigma$ is the interfacial exchange energy density, J_{ex} is the exchange parameter, S_{FM} and S_{AFM} are the spins of interfacial atoms, and a is the cubic lattice parameter of AFM. Although it provides a direct way to estimate the exchange coupling strength and $H_{EB,}$ this simple ideal model cannot realistically represent the real FM-AFM interface condition because of interface contamination or roughness.

Recent advance in thin film deposition and characterization techniques has broadened the EB research. Interesting EB effects have been exhibited in unconventional coupled material systems where a FM is layered with spin glass of CuMn,[68] paramagnetic $LaNiO_3$,[69] non-magnetic MgO[61] and multiferroic oxides.[70]

1.2.3.2 Electric field control of EB

Electric field control of EB is interesting from an application perspective because it provides an additional degree of freedom for device operation. Single-phase ME multiferroics, such as $GdFeO_3$, $YMnO_3$ and Cr_2O_3, have been used for a direct control of magnetization by the electric field,[71] which can be incorporated for electric control of EB. But the limited material selection and weak ME coupling strength can be a problem for practical applications. A more common approach is to couple AFM/FE multiferroic with a FM material so that a mutual coupling between FE and FM can be created through the AFM medium, where the interfacial spin interaction of AFM and FM, and intrinsic coupling of AFM and FM have been bridged. Figure 1.11(a) shows a representative BFO/LSMO field effect device for electric control of exchange bias, where BFO is the AFM/FE material and LSMO is the FM material.[72] With an applied 10 ms gate voltage (V_G) varying from -50 V to + 50V, the device H_c has been modulated accordingly and reached saturated states at +17 V and -17 V (Figure 1.11(b)). The H_{EB} is defined by the magnitude of peak shift in MR hysteresis loops. As shown in Figures 1.11(c)-1.11(g), when a voltage-pulse sequence is applied to the device, the normalized H_{EB}/H_c is modulated systematically. This study demonstrates a unipolar electric control of EB with no need of field cooling and temperature cycling. When the measurement geometry is changed, EB is reversibly switched by FE poling between two distinct states with opposite EB polarities, exhibiting a bipolar modulation effect.[73]

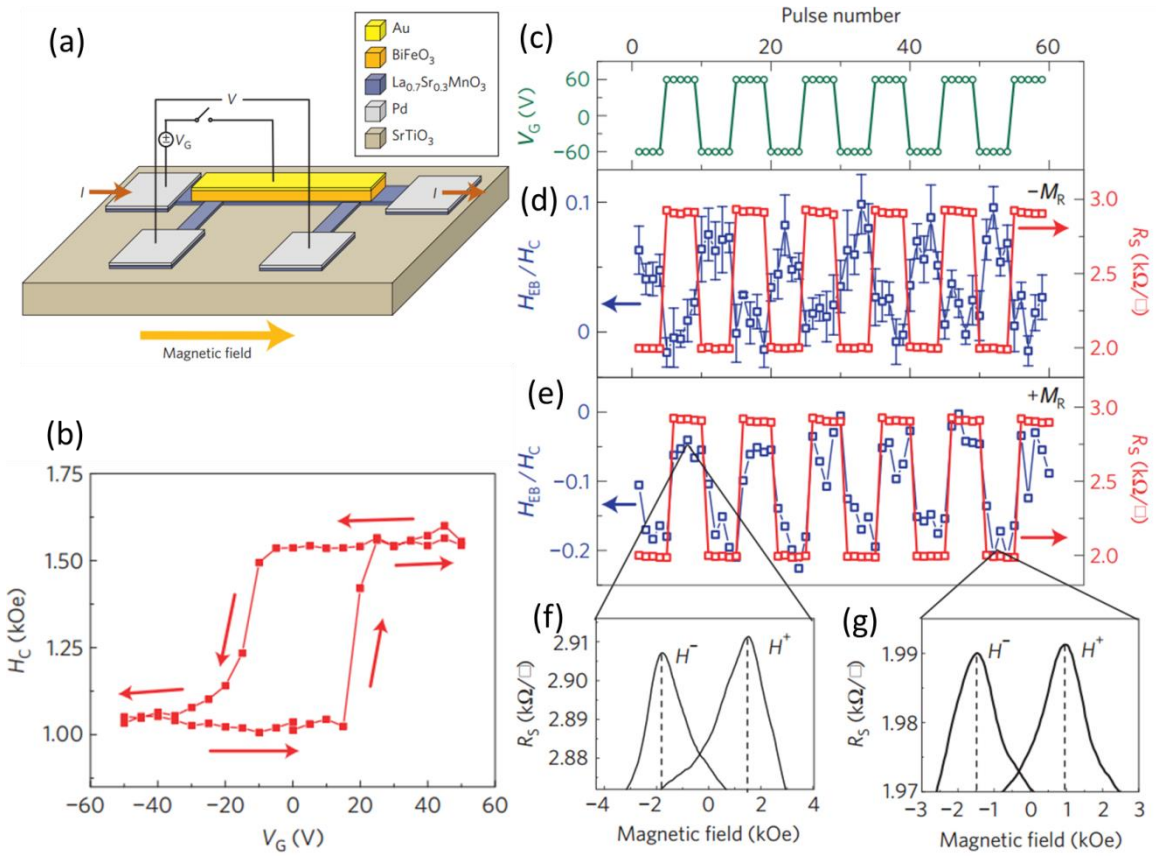

Figure 1.11. (a) A schematic configuration of the BFO/LSMO field-effect device. (b) Hysteresis of magnetic coercivity of the field device as a function of gate voltage. (c) The gate-voltage-pulse sequence for the measurements. Normalized exchange bias and sheet resistance of the device applied with a gate pulse under (d) positive remanent magnetization and (e) negative remanent magnetization. Example MR curves for the (f) upper and (g) lower states based on which exchange bias fields are calculated.[72]

1.2.3.3 Perpendicular exchange bias (PEB) and new EB systems

EB with in-plane anisotropy has been widely studied in layered structures which allow high quality growth of interfaces with easy control of layer dimension. EB with perpendicular anisotropy, the so-called perpendicular exchange bias (PEB), is more desirable for applications requiring high thermal stability at reduced dimension.[26,74]

Research efforts to achieve PEB have mostly been realized in bilayers/multilayers consisting of noble metals with high spin-orbital interaction, such as Co/(Pd,Pt) multilayers,[75] $DyCo_5$-[74] and CoFeB-based[26] spin valves. For the occurrence of PEB, the ferromagnetic layer thickness has to be confined within a few nanometers to avoid the perpendicular axis relaxation. The limited material selection, as well as the strict thickness limitation, may be challenging for the practical applications based on PEB effects. In our study, we have explored the PEB in VAN structures, which enables the exchange coupling out-of-plane and gives rise to enhanced and tunable PEB in micrometer-thick films.[76] More detailed discussion is included in Chapter V.

1.2.4 Ferroelectric properties

Ferroelectrics are a group of materials that have noncentrosymmetric crystal structure and possess spontaneous polar orientations. A spontaneous electric polarization can be switched between different polar states, yielding ferroelectric polarization and strain hysteresis loops, as seen from Figure 1. 12.[77,78]

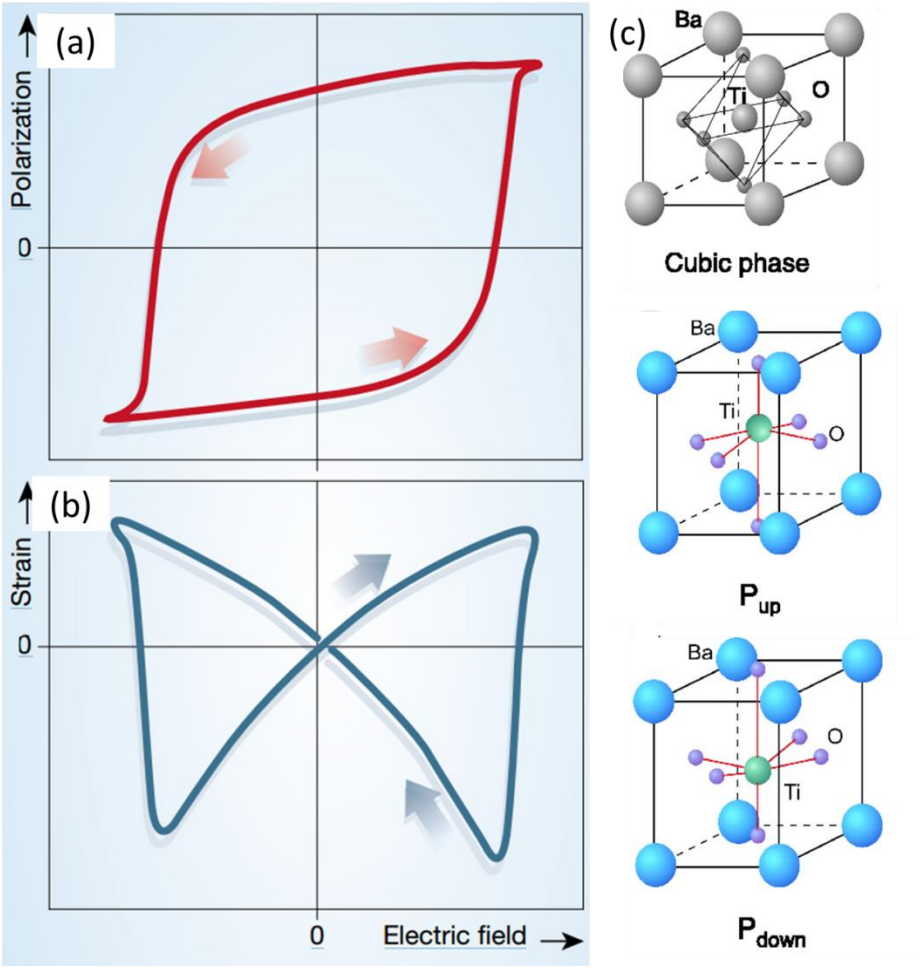

Figure 1.12. Schematic ferroelectric (a) polarization and (b) strain hysteresis loops. P represents the induced polarization, and E is the external electric field. (c) The original state and two spontaneous polarization states indicated by the displacement of central Ti atoms in $BaTiO_3$.[77,78]

Among all the ferroelectric materials, perovskite ferroelectrics are mostly studied and widely used in commercial devices. The ideal perovskite can be expressed with the formula of ABO_3, where A represents a divalent or trivalent cation, and B is a tetravalent or trivalent cation. Representative examples are $BaTiO_3$ (BTO), $PbTiO_3$ (PTO), $PbZr_xTi_{1-x}O_3$. The observation of ferroelectricity can be explained by two

complementary phenomenological models. The first model is the so-called soft (phonon) mode,[79] which suggests the spontaneous polarization results from instability of one of the normal lattice vibration modes. At a temperature below the ferroelectric phase transition temperature (the ferroelectric Curie temperature, T_c), the B atom displacement is stable because the short range ionic coulomb force cancels out with the long range dipole interaction force. Another mode is based on thermodynamic (Laudau-Ginzburg-Devonshire) theory,[80] which emphasizes on correlating the macroscopic properties such as polarization, dielectric properties and temperature. A characteristic "double-well" potential energy is formed as a function of the B cation between the oxygen ions in perovskite ferroelectrics.

Ferroelectric properties can be dramatically tuned when the ferroelectrics are grown in the form of thin films. The progress of thin film fabrication techniques provides a powerful pathway to create high-quality ferroelectrics without detrimental defects such as misfit dislocations and oxygen vacancies, so that enhanced ferroelectric performance is obtained in terms of polarization fatigue, frequency dependence of polarization, piezoelectric and dielectric properties and so on. In addition, novel ferroelectric phase and state can be obtained and stabilized with the thin film epitaxy technique. A one magnitude enhancement of polarization has been observed in epitaxial BFO thin film compared to its bulk phase, which has aroused tremendous research interests.[8]

1.2.5 Multiferroic properties

Multiferroics refers to the material that simultaneously possesses two or three "ferroic" parameters such as ferromagnetism, ferroelectricity and ferroelasticity.[2,81,82] ME coupling typically refers to the interaction of ferromagnetic and ferroelectric properties, as shown in Figure 1.13.[9] In the past decade, multiferroic and ME coupling has received significant research interests because of the promise of manipulation of polarization through an external magnetic field or in the opposite way. Unfortunately, there are very few single-phase multiferroics with sizeable ME coupling because of the conventional contradictory requirements: the tradition metal d electrons are essential for magnetism but detrimental for off-center polarization distortion.[83]

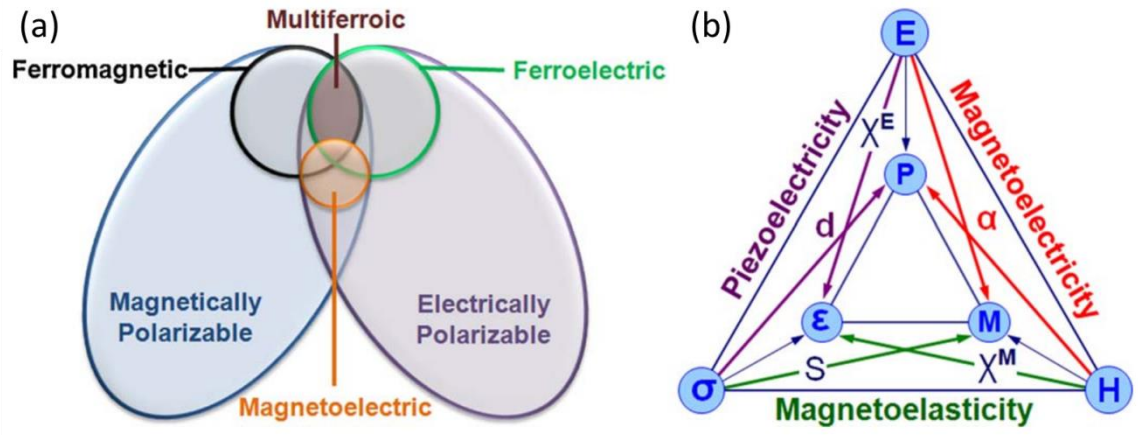

Figure 1.13. (a) Relationships among multiferroic, ferromagnetic and ferroelectric. (b) Schematics of different types of coupling of ferroic parameters.[9]

Research on multiferroics and ME coupling can be traced back to the study of $Ni_3B_7O_{13}I$ in 1960s.[84] However, it was halted for many years because of weak ME coupling. In 2003, the discoveries of strong ME coupling effect in $TbMnO_3$[85] and enhanced room-temperature polarization in BFO[8] have rekindled research interests in this field. So far, prototypical single-phase multiferroic oxides are mainly two class of materials: Bismuth-containing compounds ($BiReO_3$ (Re = Fe, Mn, Cr)) and rare-earth manganites ($ReMnO_3$ (Re = Y, Tb, Dy, Lu)).[71] It should be noted that BFO is probably the most widely studied multiferroic material. Figure 1.14 shows the seminal work by Ramesh et, al. in 2003.[8] The heteroepitaxial constrained BFO thin films have been fabricated on single-crystal STO substrates (Figure 1.14(a)), which exhibits enhanced polarization by almost one order of magnitude than that in bulk phase (Figure 1.14(b)). More importantly, the films also exhibit enhanced magnetization and promising ME coupling effect with a dE/dH coefficient of 3 V/cm·Oe.

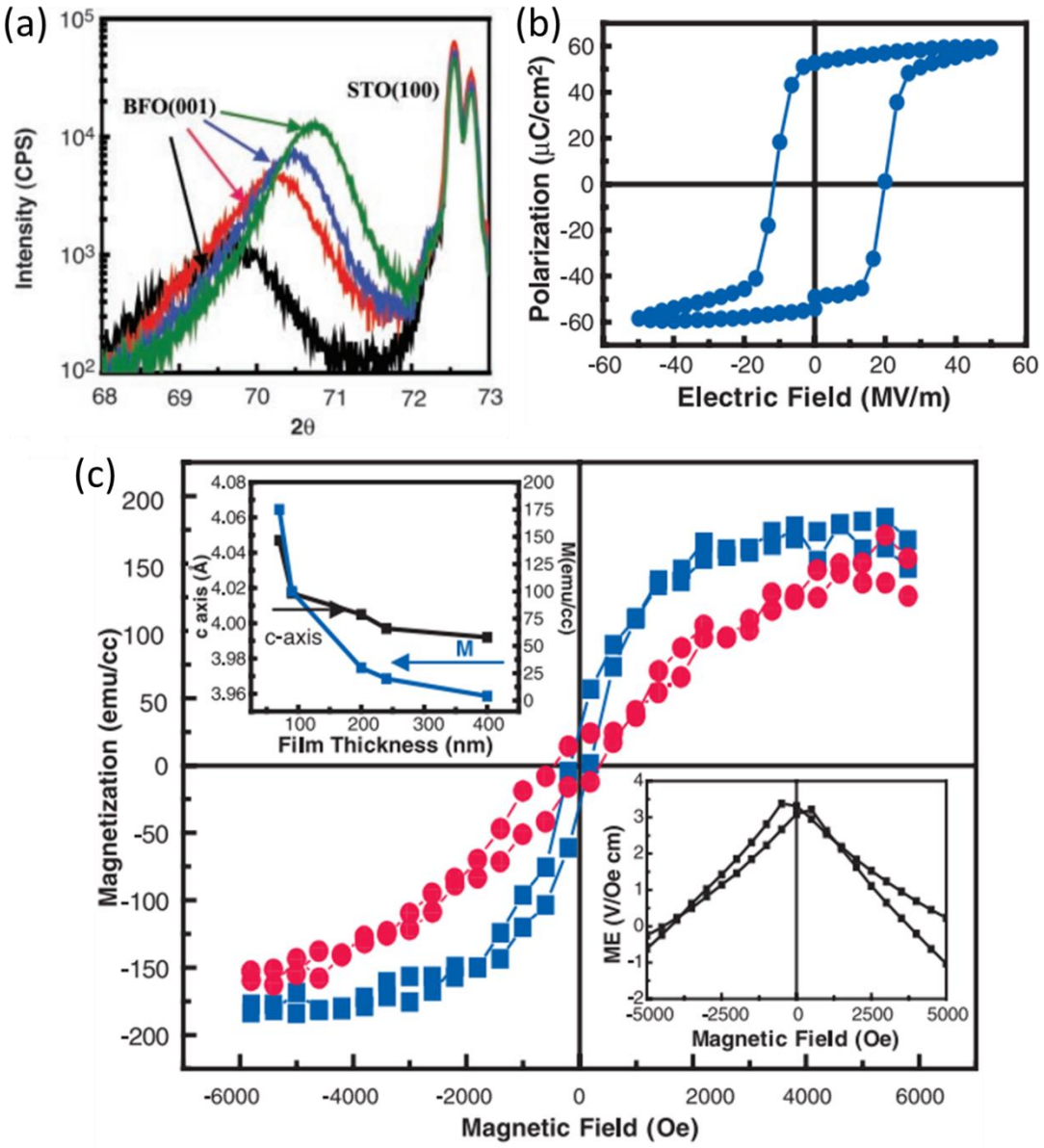

Figure 1.14. X-ray θ-2θ scans of epitaxial BFO films showing the effect of film thickness on strain. (b) A polarization versus electric field loop of a 200-nm-thick BFO films measured at 15 kHz. (c) Magnetic hysteresis loops measured by vibrating sample magnetometer for a 70-nm-thick BFO film. Inset (a) shows the thickness dependence of strain and saturate magnetization. Inset (b) shows a preliminary ME coupling strength measurement.[8]

1.3 Strain engineering in epitaxial oxide thin films

1.3.1 Thin film epitaxy and lattice mismatch strain

Thin film epitaxy refers to the extended formation of a singly-crystal film on top of a single-crystal substrate where the film maintains a preferred and fixed orientation with respect to the substrate.[86] Homoepitaxy and heteroepitaxy are two major types of epitaxy. Homoepitaxy means the film and the substrate are the same material, such as the growth of a Si layer on a Si substrate. Heteroepitaxy refers to the growth of a different material on a substrate, such as the growth of a GaN film on a Si substrate. With the advance of materials fabrication methods, this concept has been widely realized in both semiconductor and oxide growth, which provides a powerful way to fabricate high quality films and manipulate the structural defects.

Strain refers to structural deformation of a material under an external pressure. In thin film epitaxy, strain measures the deviation of the actual film lattice parameter from its free state. In the simplest case, we can assume the film and the substrate have the same cubic structure but different lattice parameters. When grown on the substrate, the film can be under compressive or tensile strain with a "strained" lattice parameter. The lattice mismatch strain *f* is calculated as

$$f = 2 \times (a_f - a_s)/(a_f + a_s), \tag{1.11}$$

where a_f, a_s are the original lattice parameters of film and substrate, respectively.

When f is close to zero, almost perfect lattice matched epitaxy can be formed with little strain in the film. When f is discernable but below 7 %, strained lattice matched epitaxy can be obtained. A coherent strain can be maintained throughout the

entire film up to a critical thickness, the so-called pseudomorphic growth region, after which the excess strain energy favors generating structural defects like dislocation and boundaries for a relaxed state. When *f* is above 7 %, misfit dislocations are preferably generated at the initial growth of the film to relax the mismatch strain. A phenomenon called domain matching epitaxy (DME) is observed in many systems,[87] which allows integral multiples of lattice planes matched between the film and the substrate across the interface. By matching m planes of the film with n planes of the substrate, the initial *f* can be largely relaxed while maintaining epitaxial film growth. With DME, the residual lattice mismatch strain (f_r) can be calculated as

$$f_r = (ma_f - na_s)/\left(ma_f + na_s\right);\ \ n = m + 1, \tag{1.12}$$

where m and n are integral numbers. The DME paradigm was proposed by Narayan and coworkers in 2003,[87] which addresses the problem of epitaxial growth of high mismatched film on a substrate. Representative examples for such growth include the TiN/Si(100) with 3/4 matching, the AlN/Si(100) with 4/5 matching and the ZnO/α-Al_2O_3 (0001) with 6/7 matching.

1.3.2 Strain engineering of functionalities in oxide thin films

With the advance of new thin film growth techniques, strain engineering of existing materials and their physical properties has experienced significant development in exploring enhanced and/or novel functionalities. Compared the local and inhomogeneous strain around defects, fully coherent strain can be introduced into thin films by the differences in lattice parameter and thermal expansion coefficient between the film and the underlying substrate. The greater availability of singly-crystal substrates

spanning a wide range of lattice parameter facilities the study of strain engineering in functional oxide thin films (Figure 1.15).[88] Commonly used singly-crystal substrates include STO, LAO, MgO, $(LaAlO_3)_{0.3}(Sr_2TaAlO_6)_{0.7}$ (LSAT), $YAlO_3$ (YAO), $NdAlO_3$, $NdGaO_3$ (NGO), and $REScO_3$ (RE = Dy, Sc, Gd, Eu). By tuning the substrate lattice parameter, significant strain up to 3 % can be maintained in ultrathin films,[89] which dramatically affects the physical properties, including enhanced mobility of transistors,[90] increased catalytic properties, band structure tuning,[91] increased critical transition temperatures of superconductivity,[92] ferroelectricity [93] and ferromagnetism.[94] In this section, we emphasize on the strain engineering of FE, magnetic and magnetotransport, and multiferroic oxide thin films.

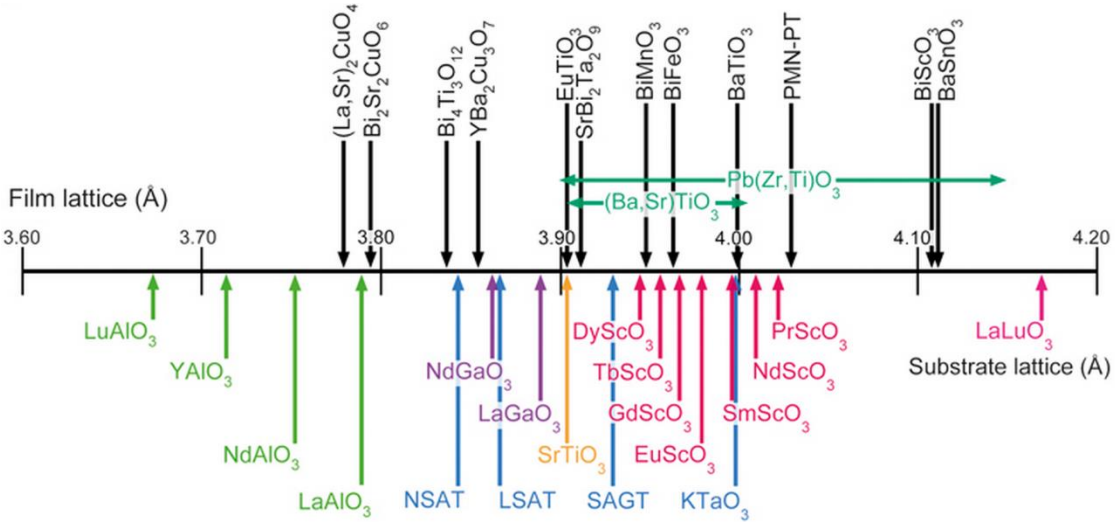

Figure 1.15. A list of perovskite and perovskite-related substrates ordered by their a-axis lattice parameter.[88]

1.3.2.1 Strain engineering of FE oxide films

The strong relationship between FE properties and strain (or hydrostatic pressure with respect to bulk) has been established for a long time. The capability of maintaining large coherent strain in FE thin films, which usually causes cracks in bulk, makes a significant step forward in the study of strain effect on FE properties. Thermodynamic calculation and phase field modeling make it possible to obtain a strain-phase diagram for FE materials, and thus suggest a guideline for the strain tuning for FE films.[95,96]

One of the major achievements is to enhance the FE transition temperature and polarization of FE oxide films. Figures 1.16(a) and (b) show the strain-phase diagrams of (001)-oriented STO[97] and BTO[98] assuming a single-domain state for all structures and phases, respectively. It can be seen that using appropriate biaxial strain, FE phase transition can be induced. Experimental observations indeed confirm the above calculation results. For example, using the substrate-induced biaxial strain, Schlom and coworkers shift the FE transition temperature by hundreds of degrees to make STO as a room-temperature FE.[99] At almost the same time, Eom and coworkers used the biaxial compressive strain to obtain a remanent polarization over 250 % higher than bulk BTO single crystals (Figure 1.16(c)) and a high transition temperature over 500 ℃ (Figure 1.16(d)).[100]

It should be noted that it is still difficult to make quantitatively accurate estimation for a variety of FE materials using theoretical methods because of the complex structure and possible domain formation. First-principle calculations can be

combined with current methods for a better understanding and utilization for stain tuning for FE thin films.

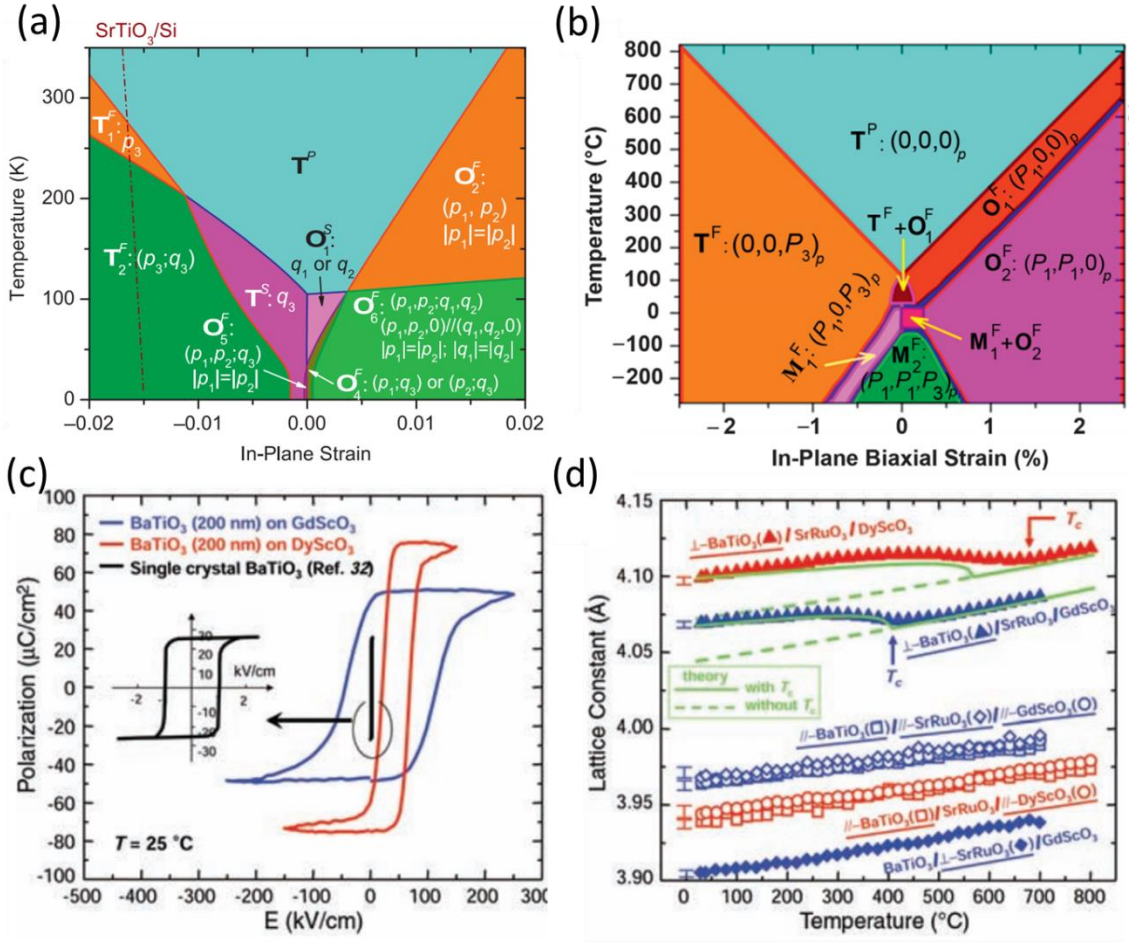

Figure 1.16. Strain-phase diagrams of (001)-oriented (a) STO and (b) BTO obtained from phase-field simulations assuming a single-domain state for all structures and phases. (c) Polarization versus electric field hysteresis loop of 200-nm-thick BaTiO3 thin film grown on $GdScO_3$ (GSO) and $DyScO_3$ (DSO) substrates with $SrRuO_3$ as bottom and top electrodes. Inset is the hysteresis loop of a bulk single-crystal $BaTiO_3$ for comparison. (d) Temperature dependence of the latter parameter of strained $SrRuO_3/BaTiO_3/SrRuO_3$ (SRO/BTO/SRO) thin film capacitor on GSO and DSO substrates. The ⊥ and // represent the out-of-plane and in-plane direction, respectively. The slope change in at high temperatures indicates a FE phase transition.[88,97,100]

Another important function of thin film epitaxial strain is stabilizing a morphotropic phase boundary in the lead free FE BFO film.[101] Through exploiting epitaxial strain introduced from the substrate, a morphotropic phase boundary through the BFO film is stabilized and enhanced piezoelectric response has been obtained. The monoclinically distorted rhombohedral BFO is maintained when grown on the single-crystal STO (001) substrate. However, when grown on substrates with large lattice mismatch, a tetragonal BFO phase is obtained, as seen from the X-ray diffraction (XRD) pattern and transmission electron microscopy (TEM) image (Figures 1.17 (a) and (b)). Upon increasing film thickness, the coexistence of tetragonal and rhombohedral phases in thick BFO films has been observed in high-resolution TEM image (Figure 1.17 (b)) and atomic force image (Figure 1.17 (d)).[102] The strain-driven morphotropic phase boundary enhances the piezoelectric response (Figure 1.17 (c)),[102] which provides a new pathway to create such boundaries other than chemical alloying in conventional studies of piezoelectrics.

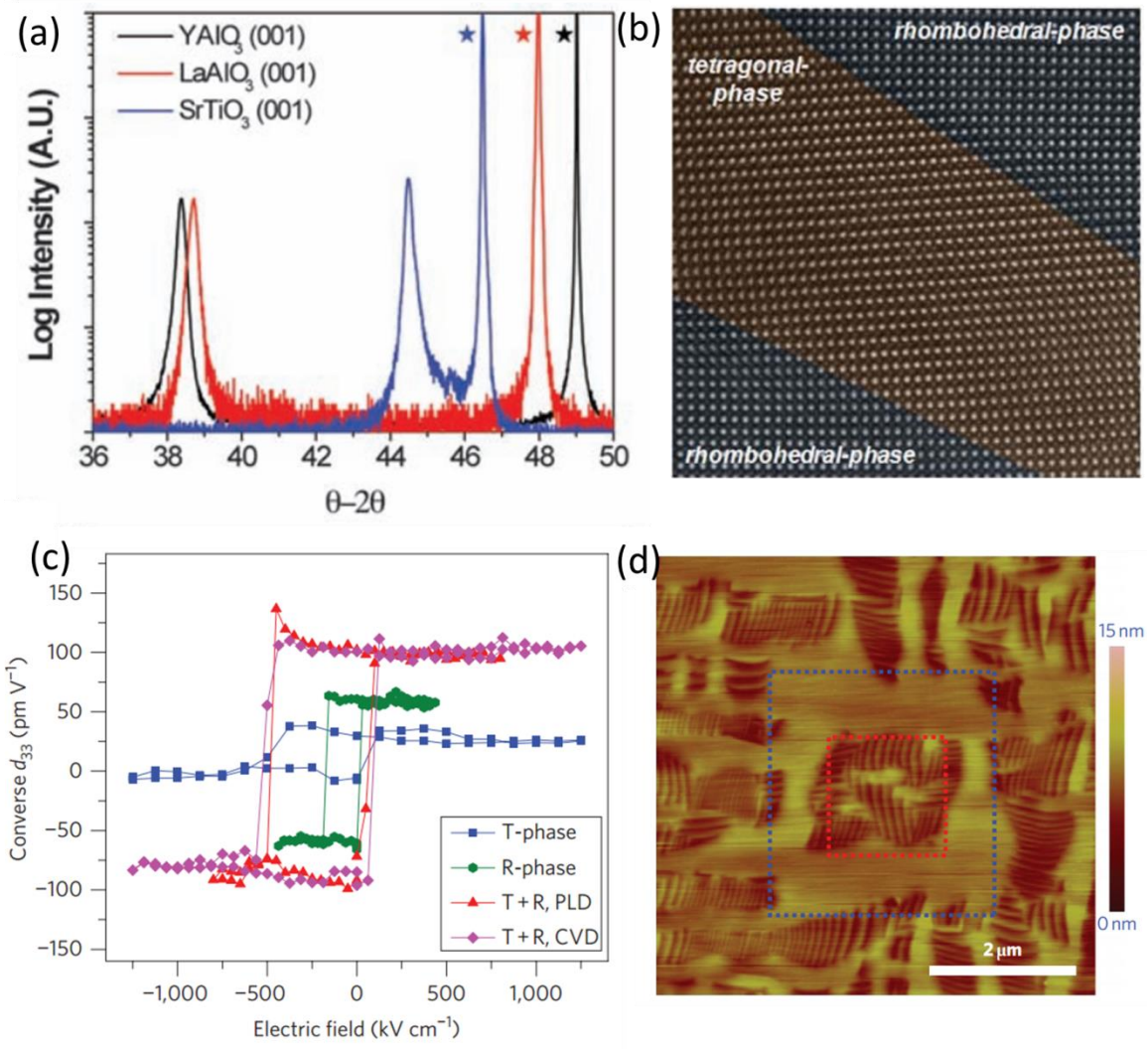

Figure 1.17. (a) X-ray diffraction results of BFO/STO(001), BFO/LAO(001), and BFO/YAO(001) showing the presence of a tetragonal BFO phase grown on YAO and LAO substrates. (b) High-resolution TEM image of a morphotropic phase boundary between the rhombohedral and tetragonal BFO phases. (c) Piezoelectric hysteresis loops from T-phase, R-phase and mixed-phase of BFO thin films. (d) AFM image of an electric-field-induced phase transition between mixed phase and T-phase.[101,102]

1.3.2.2 Strain engineering of ferromagnetic oxide films

The influence of epitaxial strain on ferromagnetic properties is achieved by structural distortions such as oxygen octahedral distortion or rotation in ABO_3 perovskite structures. The strong interplay of lattice, charge, spin and orbital degrees of freedom in correlated oxides make it possible to use strain as a key parameter to manipulate the magnetic properties of ferromagnetic oxide thin films. A representative example is the strong strain effect on magnetism of epitaxial manganite films, particularly the magnetic anisotropy,[103] phase transition temperature[94] and electron/magneto transport behavior.[104] Depending on the doping level and strain state, the DE interaction strength in hole-doped manganites show up accompanied with respective spin/optical ordered and disordered states, which includes ferromagnetic-metallic state, 2D metallic state and a chain-type state (Figure 1.18(a)).[105] By adjusting the underlying substrate parameters, different lattice parameters and variable strain from -2.3% to +3.2 % have been obtained (Figures 1.18(b) and (c)).[106] In general, larger tensile strain results in reduced phase transition temperature and increased resistivity up to several orders of magnitude. Figure 1.18(d) shows the magnetotransport behavior of LSMO films grown on GSO, LSAT and STO substrates with a $La_{0.7}Sr_{0.3}FeO_3$ as a buffer layer.[107] When the c/a ratio is over 0.98, a larger MR with a broadened peak feature has been observed with decreasing c/a ratio. Recent studies reveal that the epitaxial strain also introduces anisotropic transport in LSMO ultrathin films. Under large tensile strain, LSMO films display different in-plane resistivity behavior between orthogonal directions (schematic measurement configuration shown in the inset of Figure 1.18(e)).[108] Figure 1.18(e) shows that the

resistivity anisotropy characterized by $(\rho_b-\rho_a)/\rho_a$ is 30 % at 95 K and has a switch resistivity axis at ~130 K. The anisotropy resistivity behavior, however, is not shown in the films grown on STO, NGO and LAO.

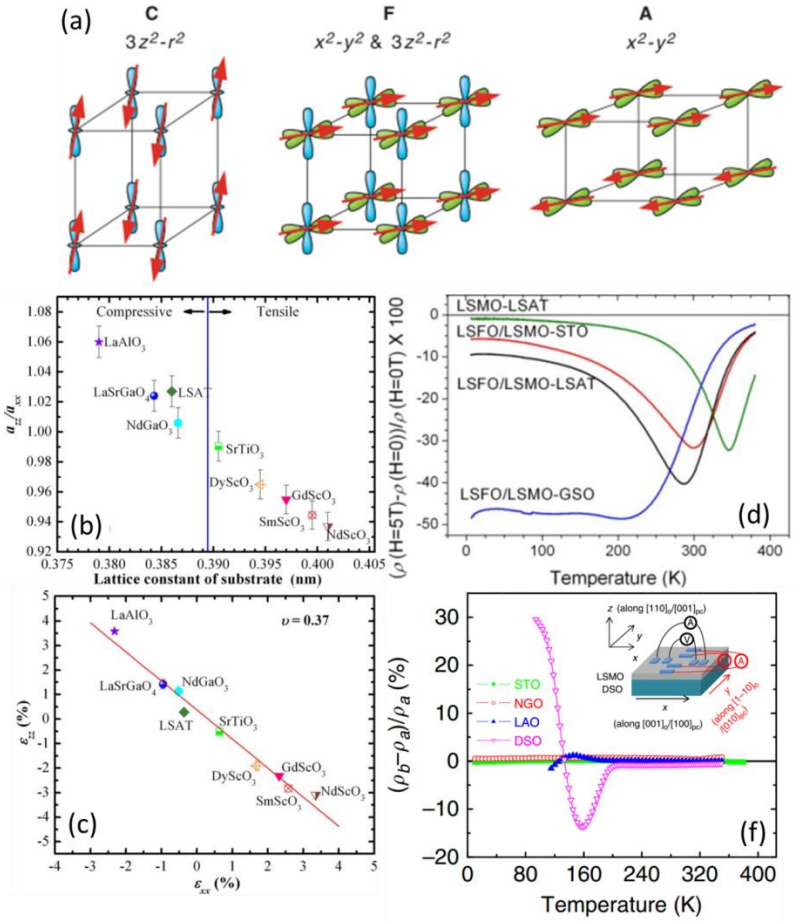

Figure 1.18. (a) A chain-type (C) state, ferromagnetic-metallic (F) state, 2D metallic (A) state in hole-doped manganites achieved by different doping concentration and strain states. (b) The ratio of out-of-plane (a_{zz}) and in-plane (a_{xx}) lattice parameter of LSMO films as a function of lattice parameter of substrates. (c) The out-of-plane lattice strain (ε_{zz}) as a functional of the in-plane strain (ε_{xx}). (d) MR of LSMO films on STO, LSAT, GSO substrates as a function of temperature. (e) The in-plane resistivity anisotropy ratio of ultrathin LSMO films on STO, LAO, NGO and DSO substrates. The inset shows the schematic experimental set-up for the in-plane resistivity measurements.[105-108]

1.3.2.3 Strain engineering of multiferroic and ME oxide films

Recently, the study of multiferroic nanocomposites flourishes, which employs extrinsic ME coupling between a FE materials and a ferromagnetic material. Effective strain coupling is achieved in the form of particulate nanocomposites, laminated nanocomposites or vertically aligned heterostructures. The ME coupling can be understood by the constitutive equations for the magnetic-mechanical-electric interactions using a direct notation for tensors,[109,110] as follows:

$$\sigma = cS - e^T E - q^T H,$$
$$S = eS + \varepsilon E + \alpha H,$$
$$B = qS + \alpha^T E + \mu H, \qquad (1.13)$$

where σ, S, D, E, B, and H are the stress, strain, electric displacement, electric field, magnetic induction, and magnetic field, respectively; c, ε, μ are stiffness, dielectric constant and permeability, respectively; $e$and q are the piezoelectric and piezomagnetic coefficients, respectively. α is the ME coupling coefficient, which is calculated as $\Delta M/\Delta E$, where ΔM is the change of magnetization by an external electric bias (ΔE).

Numerical calculations suggest that α is generally larger in vertically aligned heterostructures than other kinds of nanocomposites. Figure 1.19(a) shows the plan-view TEM image of the seminal BTO:CFO vertically aligned nanostructure.[55] Through elastically coupling between magnetostrictive and electrostrictive phases in the nanostructure, ME coupling has been observed as seen from the magnetization change in the temperature dependent magnetization around the FE transition temperature (Figure 1.19(b)).[55] After this pioneering work, significant research efforts have been devoted in

this field. A more direct ME coupling has been demonstrate in heteroepitaxial BFO:CFO nanocomposite films. Self-assembled CFO nanopillars have been obtained in this nanostructure, as shown in Figure 1.19(c), which shows distinct magnetization change by applying an electric bias (Figure 1.19(d)).[111]

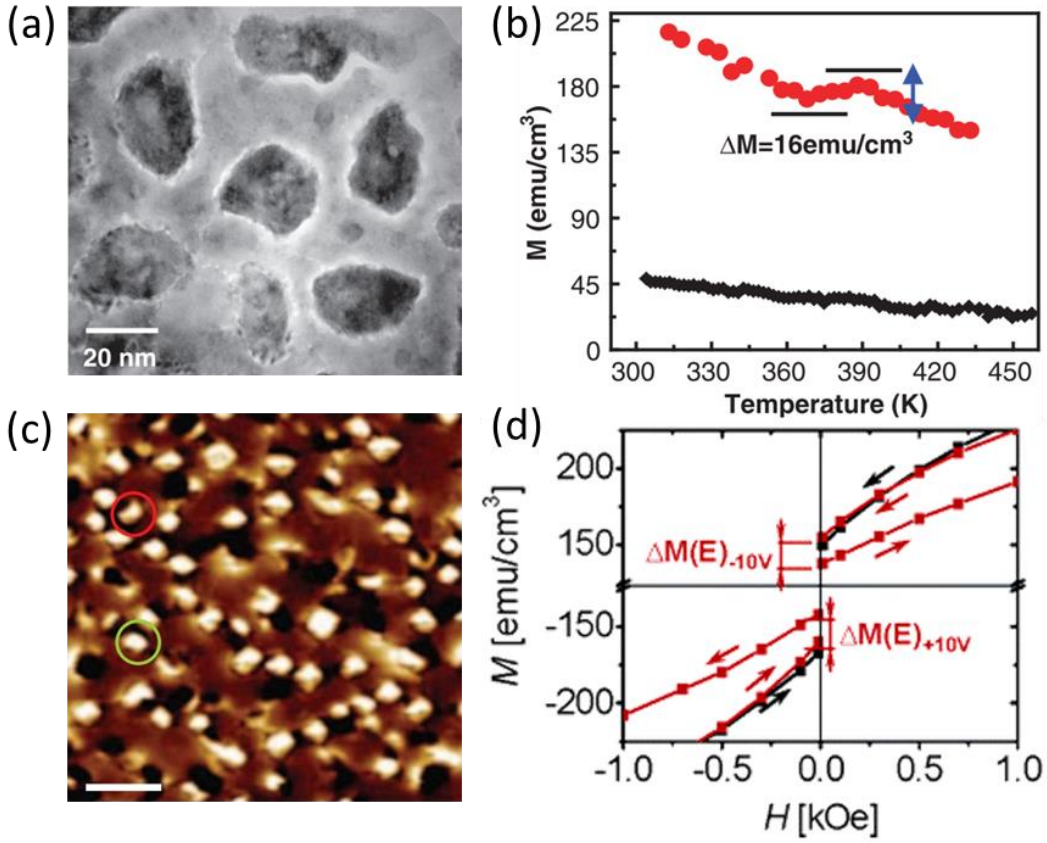

Figure 1.19. (a) Plan-view TEM image of BTO:CFO nanocomposite films showing self-assembled CFO nanopillars in the BTO matrix. (b) Temperature dependent magnetization of BTO:CFO nanocomposite film and multilayered film. A distinct magnetization change has been observed in the nanocomposite film, which is not seen in the multilayered film. (c) Magnetic force microscopy image of BFO:CFO nanocomposite films. (d) Magnetization hysteresis loop of the BFO:CFO film before (black curves) and after (red curves) an electric field poling.[55,111]

1.4 Vertically aligned nanocomposite thin films

1.4.1 Overview of VAN films

Strongly correlated oxides have been widely used to accomplish enhanced or novel multifunctionalities which arise from the interplay between structural (lattice), electronic (orbital and charge), and magnetic (spin) degrees of freedom. In parallel with particular nanocomposites (0-3 type; Figure 1.20(a))[112] and high-quality multilayered thin films (2-2 type; Figure 1.20(d)),[113] heteroepitaxial VAN thin films (1-3 type; Figures 1.20(c)[114] and (d))[115] have emerged a new thin film platform in the past decade. Here the notation number indicates where the connectivity of the pillar phase (first number) and the matrix (second) is in zero, one, two or three dimensions. In VAN thin films, at least one strongly correlated metal oxide is grown with another synergistically selected oxide in a film-on-substrate geometry. Different from conventional nanocomposite with polycrystalline quality and randomly-distributed interfaces, the VAN architecture achieves three-dimensional heteroepitaxy with self-assembled vertical interfaces, which allows cooperative coupling effects.[116-120] Easy dimensional tunability has been demonstrated in VAN films, where various pillar shape and sizes have been obtained in different materials systems (Figure 1.20(d)).[120]

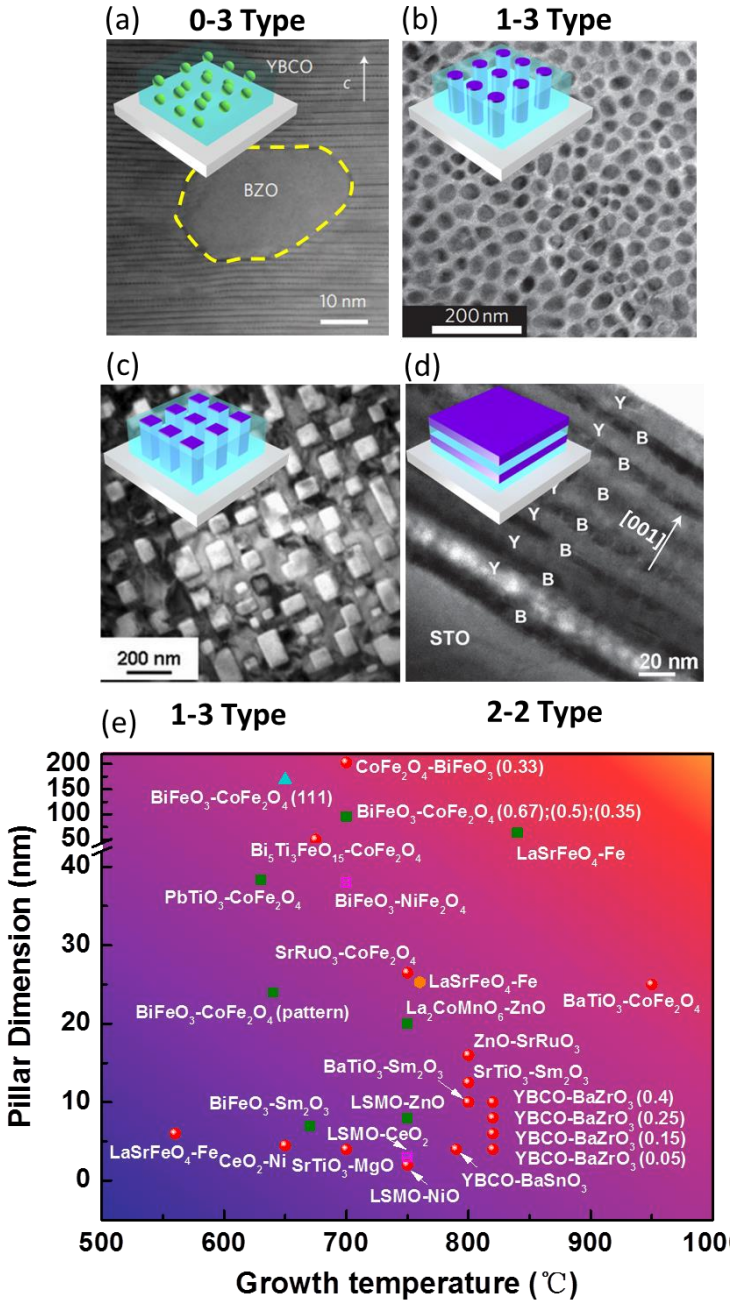

Figure 1.20. (a) 0-3 type nanocomposite of $BaZrO_3$ (BZO) nanoparticles embedded in a $YBa_2Cu_2O_{7-x}$ (YBCO) matrix. 1-3 type VAN films of (b) Sm_2O_3 nanopillars in a BTO matrix and (c) CFO nanopillars in a BTO matrix. (d) a 2-2 type laminated YBCO-BZO nanocomposite film. Insets show the schematic microstructure of the nanocomposite films. (e) Pillar dimension of vertically nanopillars in VAN films as a function of growth temperature.[112-115,120]

Table 1.2. Summary of representative VAN systems fabricated in the past decade. The phase listed first is phase 1, usually a perovskite. Phase 2 is listed in the latter. The calculated strain for non-perovskite phase is not given, since their strain relationships is highly orientation dependent.

VAN systems	**Crystal structure**	**Bulk lattice parameter (Å)**	**Calculated IP strain[†] (%)**	**Calculated OP strain[§] (%)**	**Ref.**
$BiFeO_3$:Sm_2O_3	Perovskite–Rocksalt	a_1=3.962 a_2=10.927/4*√2=3.863	1.15	2.56 (*1.51*)[‡]	122-124
$BiFeO_3$:$CoFe_2O_4$	Perovskite–Spinel	a_1=3.962 a_2=8.392/2=4.196	-7.18	-5.79	111, 125
$BiFeO_3$:$NiFe_2O_4$	Perovskite–Spinel	a_1=3.962 a_2=8.339/2=4.170	-6.55	-5.15	126
$BiFeO_3$:Nd_2O_3	Perovskite–Rocksalt	a_1=3.962 a_2=11.08/4*√2=3.917	-0.31	1.09	118
$BiFeO_3$:Eu_2O_3	Perovskite–Rocksalt	a_1=3.962 a_2=10.868/4*√2=3.842	1.63	3.02	118
$BiFeO_3$:$BaZrO_3$	Perovskite–Perovskite	a_1=3.962 a_2=4.193	-7.11	-5.72	118
$BaTiO_3$:Sm_2O_3	Perovskite–Rocksalt	a_1=3.994 a_2=10.927/4*√2=3.863	1.16	3.41	114
$BaTiO_3$:$CoFe_2O_4$	Perovskite–Spinel	a_1=3.994 a_2=8.392/2=4.196	-7.18	-4.93	55
$BaTiO_3$:$NiFe_2O_4$	Perovskite–Spinel	a_1=3.994 a_2=8.339/2=4.170	-6.55	-4.30	127

Table 1.2. Continued

VAN systems	**Crystal structure**	**Bulk lattice parameter (Å)**	**Calculated IP strain[†] (%)**	**Calculated OP strain[§] (%)**	**Ref.**
$La_{0.7}Sr_{0.3}MnO_3$: ZnO	Perovskite–Wurtzite	a_1=3.870 a_2=3.242, c_2=5.207	-----	(*0.50*)	122, 128, 129
$La_{0.7}Sr_{0.3}MnO_3$: CeO_2	Perovskite–Fluorite	a_1=3.870 a_2=5.41/√2=3.825	2.07	1.17 (*0.33*)	130
$La_{0.7}Sr_{0.3}MnO_3$: Mn_3O_4	Perovskite–Spinel	a_1=3.870 a_2=8.42/2=4.210	-7.51	-8.42	131
$La_{0.7}Sr_{0.3}MnO_3$: NiO	Perovskite–Rock salt	a_1=3.870 a_2=4.17	-6.56	-7.46	132
$La_{0.7}Sr_{0.3}MnO_3$: $BiFeO_3$	Perovskite–Perovskite	a_1=3.870 a_2=3.96	-1.40	-2.30	76
$La_{0.7}Ca_{0.3}MnO_3$: MgO	Perovskite–Rock salt	a_1=3.820 a_2=4.211	-7.54	-9.73	121
$La_{0.7}Ca_{0.3}MnO_3$: NiO	Perovskite–Rock salt	a_1=3.820 a_2=4.170	-6.56	-8.76	133
$PbTiO_3$: $CoFe_2O_4$	Perovskite–Spinel	a_1=3.961 a_2=8.392/2=4.196	-7.18	-5.76	134
$BaZrO_3$: $YBa_2Cu_3O_{7-x}$	Perovskite–Layered perovskite	a_1=4.193 a_2=3.852 c_2=11.680/3=3.894	1.37	8.48	135
$BaSnO_3$: $YBa_2Cu_3O_{7-x}$	Perovskite–Layered perovskite	a_1=4.193 a_2=3.852 c_2=11.680/3=3.894	1.37	6.63	136

Table 1.2. Continued

VAN systems	**Crystal structure**	**Bulk lattice parameter (Å)**	**Calculated IP strain[†] (%)**	**Calculated OP strain[§] (%)**	**Ref.**
$SrTiO_3$:MgO	Perovskite–Rocksalt	a_1=3.905 a_2=4.211	-7.54	-7.54	118
$SrTiO_3$: Sm_2O_3	Perovskite–Rocksalt	a_1=3.905 a_2=10.927/4*√2=3.863	1.16	1.16	137
$SrZrO_3$: RE_2O_3 (RE=Sm, Eu, Gd, Dy, Er)	Perovskite–Rocksalt	a_1=4.090 a_2=(4.110~4.170)	-5.11~-6.56	-0.49~-1.93	138
$Ba_{0.6}Sr_{0.4}TiO_3$: Sm_2O_3	Perovskite–Rocksalt	a_1=3.965 a_2=10.927/4*√2=3.863	1.16	2.68	139
$SrRuO_3$: $CoFe_2O_4$	Perovskite–Spinel	a_1=3.930 a_2=8.392/2=4.196	-7.18	-6.54	140
$LaSrFeO_4$:Fe	Perovskite-Body-centered cubic	a_1=3.880, c_1=1.276 a_2=2.870*√2=4.058	-3.84	-4.48	141
CeO_2: Ni	Fluorite-Face-center-cubic	a_1=5.410 a_2=3.52	10.4	8.3	142
($Ce_{0.9}Gd_{0.1}O_{1.95}$): ($Zr_{0.92}Y_{0.08}O_{1.96}$)	Fluorite-Tetragonal	a_1=5.418/√2=3.832 a_2=5.147/√2=3.640	7.02	5.13	143
($Ce_{0.9}Gd_{0.1}O_{1.95}$): ($La_{0.5}Sr_{0.5}CoO_3$)	Fluorite-Perovskite	a_1=5.418/√2=3.832 a_2=3.810	2.46	0.57	144

Table 1.2. Continued

VAN systems	**Crystal structure**	**Bulk lattice parameter (Å)**	**Calculated IP strain[†] (%)**	**Calculated OP strain[§] (%)**	**Ref.**
($Ce_{0.9}Gd_{0.1}O_{1.95}$): ($PrBaCo_2O_{5+x}$)	Fluorite-Double-perovskite	a_1=5.418/√2=3.832 a_2=3.908	-0.08	-1.97	145

[†] The calculated in-plane strain on STO in this figure represents the value of phase 2. The in-plane strain for phase 1 ($BiFeO_3$, $BaTiO_3$, $La_{0.7}Sr_{0.3}MnO_3$, $La_{0.7}Ca_{0.3}MnO_3$, $PbTiO_3$, $BaZrO_3$, $BaSnO_3$, $SrTiO_3$, $SrZrO_3$, $Ba_{0.6}Sr_{0.4}TiO_3$, $SrRuO_3$, CeO_2, $LaSrFeO_4$, $Ce_{0.9}Gd_{0.1}O_{1.95}$) is -1.40%, -2.25%, +0.90%, +2.20%, -1.42%, -7.11%, -5.26%, 0, -4.62%, -1.52%, -0.64%, +2.07%, +0.64% and +1.90%, respectively. The sign of "-" represents compressive strain, and the "+" singe is for tensile strain.

[§] The calculation of out-of-plane lattice strain is based on the lattice constant of phase 1.

[‡] The values in the parentheses are the real domain-matching strain evidenced by TEM study.

The first work on epitaxial two-phase nanocomposite films was introduced in the study of the LCMO:MgO system in 2002.[121] As the MgO concentration varies, a stress accommodation through s structural phase transition has been observed, which results in a drastic change in the resistivity and magnetotransport properties. In 2004, ME coupling has been accomplished in BTO:CFO nanocomposite films through the elastic interactions between magnetostrictive CFO and electrostrictive BTO.[55] This study has aroused much research interests to create sizeable ME coupling with this nanocomposite approach. Later, systematic vertical strain control has been demonstrated in spontaneously phase-ordered BFO:SmO and LSMO:ZnO VAN systems,[122] which provides a new route to achieve vertical strain state in thick films. After that, lots of

VAN structures have been prepared by selecting appropriate materials systems, which are summarized in Table 1.2.[55,76,111,122-145] There are several guidelines to be considered when selecting possible constitutes to grow the VAN structure. First, a close lattice match between two phases, as well as a crystal-symmetry-based inter-relationship between them (for example, perovskites and spinels), should be satisfied. Second, the epitaxial relationship of the two phases with the substrate, particularly the matrix phase, should be satisfied in order to epitaxially seed the initial growth of the film. Third, a low solubility and close growth kinetics of two phases should be pursued for the epitaxial growth of both phases with minimum inter-diffusion. Last, preferably similar crystal chemistries and/or different elastic constants are required in some systems for strong elastic couplings between two phases.

1.4.2 Growth and microstructure of VAN thin films

To design various VAN architectures with desired functionalities, a fundamental understanding of the growth mechanisms is needed. The equilibrium microstructure and film morphology of a two-phase nanocomposite is largely determined by the thermodynamic stability of the two component phases at a given deposition condition. Different chemical miscibility determines the formation of VAN film from the starting target mixture either by (i) nucleation and growth or (ii) (pseudo-)spinodal decomposition growth. In the following section, we discuss the above formation mechanism of the VAN films grown by PLD with representative examples.

1.4.2.1 Nucleation and growth

In the case of the film-on-substrate geometry, the film morphology is controlled by several important factors, including surface and interfacial energy of each single phase, the growth temperature and the growth rate, the mixture composition ratio, and lattice matching between the substrate and the film phases.[120] Various pillar shapes and dimensions have been observed depending on specific material systems and growth parameters. The growth of most nanocomposite systems is dominated by the mechanism of nucleation and growth, as shown in the schematic of Figure 1.21.[117] In brief, the VAN films with two immiscible phases start the growth from forming the nuclei and growing into pillars for the phase with a higher interfacial energy γ_1 (lower wettability) with the substrate, while the other phase with a larger interfacial energy γ_2 adopts the layer-by-layer growth and becomes the planar matrix. The pillar size (d) can be estimated by a standard two-dimensional diffusion model:

$$d^2 = 4D_0 e^{-Ea/kT}(1/v)\,, \tag{1.14}$$

where D is the diffusion coefficient, E_a is the activation energy, k is the Boltzmann constant, T is temperature and v is the growth rate. Therefore, tuning the growth temperature and grow rate are two common ways to manipulate the pillar size in VAN nanostructures.

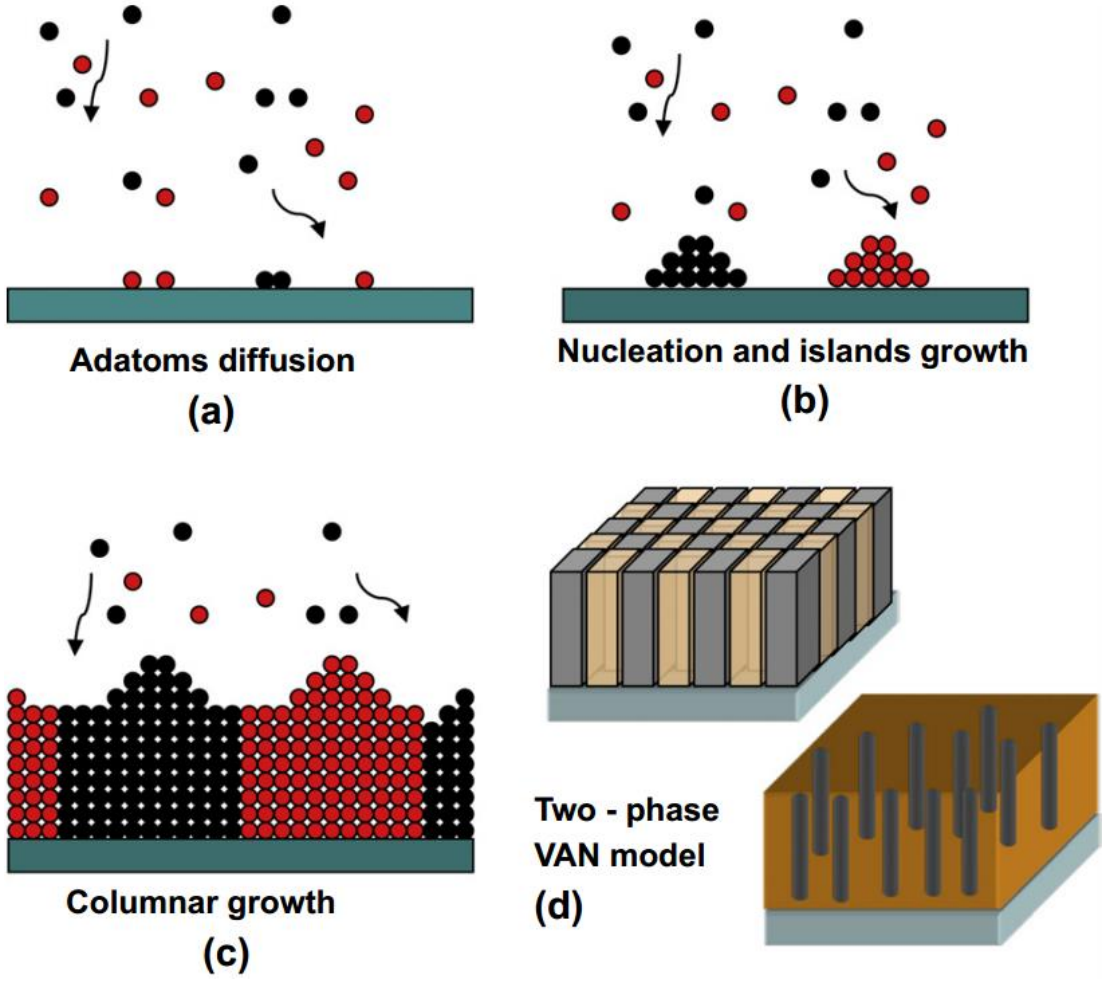

Figure 1.21. Schematic of the growth process in the formation of VAN thin films. (a) Atomic diffusion. (b) Nucleation and island formation. (c) Columnar growth. (d) Different final morphology.[117]

A well-studied example of nucleation and growth is the multiferroic BFO:CFO system. Through the careful control of surface/interface energy associated with substrate orientations, the role of phases forming nanopillars and the surrounding matrix has been exchanged for the minimization of the overall γ: rectangular CFO(001) pillars in a BFO(001) matrix, triangular BFO(111) in CFO(111), and striped BFO(110) in

CFO(110). The morphology of rectangular, triangular and striped nanopillars has been explained by Wulff shapes based on the Winterbottom construction, as shown in the atomic force microscopy (AFM) image and schematic models in Figure 1.22. Besides this surface energy/wetting consideration, several important factors should also be included to determine the final morphology of the VAN nanostructures, including the kinetic energy of adatoms, the activation energy for diffusion and lattice strain confinement between the substrate and two phases. For example, the role of CFO, formed as nanopillars on $SrTiO_3$ (STO) (001) substrate because of its higher γ ($\gamma_{CFO(001)}$=1.486 J/m^2), becomes the planar matrix when deposited with increased laser energy density.[46] Meanwhile, when growing with $BaTiO_3$ (BTO), $\gamma_{BTO(001)}$=1.26 J/m^2) on STO (001), the original rectangular CFO nanopillars change to faceted ones in the BTO matrix,[55] which could be attributed to the different elastic strain energies between CFO and BTO.

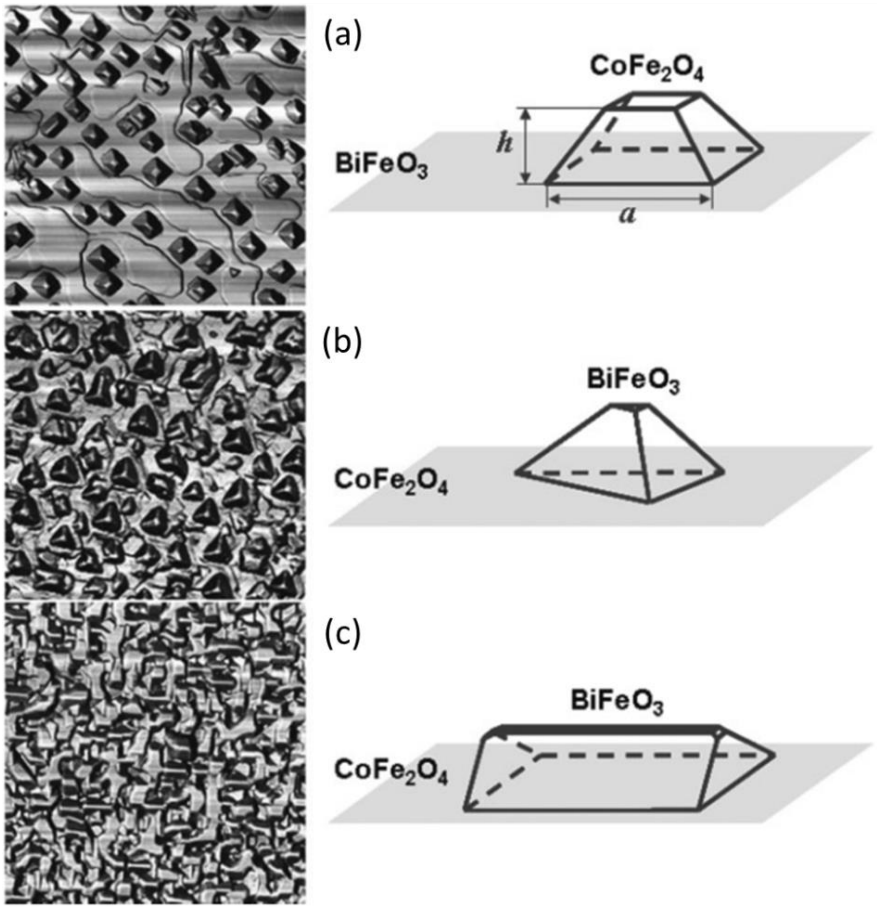

Figure 1.22. AFM phase-contrast images and schematic morphology models of BFO-CFO VAN films grown on (a) (001), (b) (111) and (c) (110) oriented STO substrates.[115]

Only in the YBCO/BZO system has a switch from vertical nanocomposite geometry to planar multilayer geometry been observed, so far (Figure 1.23).[113] This switch occurs when the phase fraction of one phase increased from a low value to around half. Using an interface energy analysis, it has been predicted that the planar horizontal 2:2 structure formed only when the phases in the composite have the same crystallographic structure and hence relatively low interface energies, and when they are

present in approximately the same fraction. Pseudo-spinodal decomposition effects (see more below) were also believed to play a role in stabilizing the planar geometry.

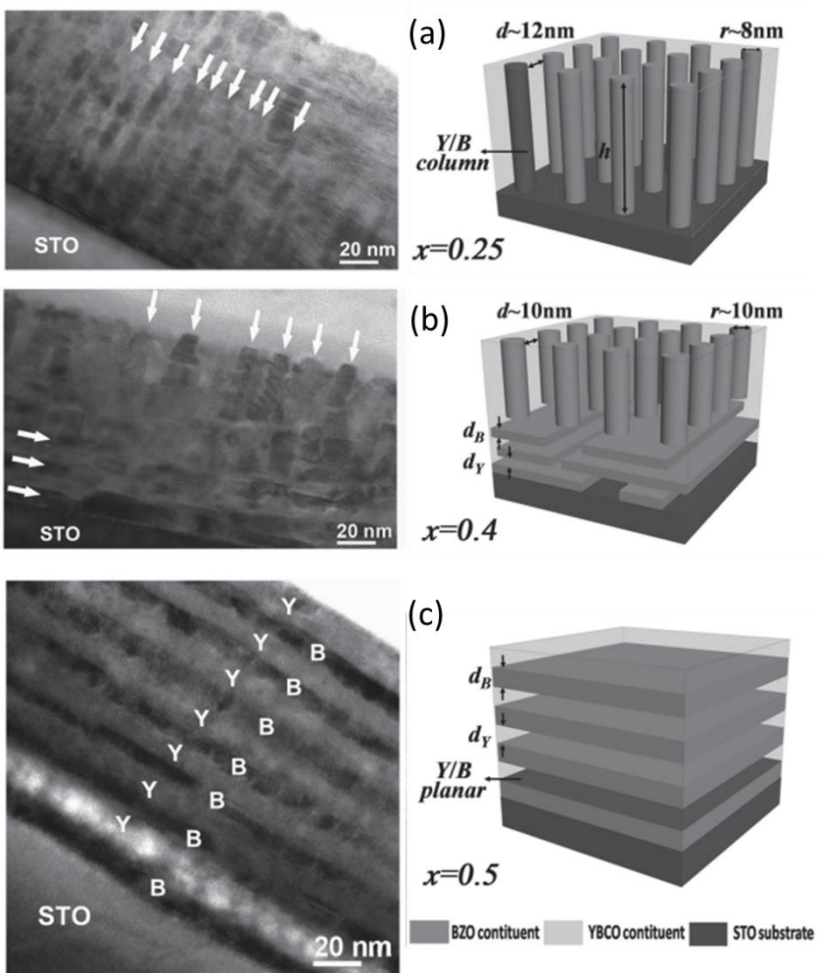

Figure 1. 23. Cross-sectional TEM images of $YBCO_{1-x}$:BZO_x thin films with x = (a) 0.25, (b) 0.4, (c) 0.5, showing a composition-modulated microstructure transition from vertically aligned nanostructure to self-assembled layered structure.[113]

1.4.2.2 (Pseudo-)spinodal decomposition

Spinodal or pseudo-spinodal decomposition growth occurs in certain systems, and gives rise to spatially ordered structures.[147] The spinodal mechanism usually occurs in composite systems where one or more cations intermix between the phases in the composite during growth. Two key examples are BFO:SmO and LSMO:ZnO films grown on STO.[122] In the BFO:SmO system, owing to the relatively low melting point of BFO, well faceted square grains were achieved with a good degree of spatial ordering, whereas in LSMO:ZnO the much higher melting points of the phase means that irregular, more classic spinodal structures without clearly defined spatial ordering were formed.

The pseudo-spinodal mechanism is similar to conventional spinodal decomposition in that gradually develops product phases from a parent solid solution phase, but is distinguished from spinodal decomposition by the requirement of a symmetry-lifting crystal lattice rearrangement. A representative example is in $ZnMnGaO_4$ films where a very fine (4-6 nm), highly regular nano-chessboard structure was formed with a transition layer of ~50 nm (Figures 1.24(a) and (b)).[148] Unlike in the two spinodal examples listed above, the two phases forming the checkerboard in the $ZnMnGaO_4$ system are compositionally and structurally more similar, which consists of rotated tetragonal and orthorhombic domains illustrated from the reciprocal space map (RSM) result (Figure 1.24(c)) and the schematic diagram (Figure 1.24(d)). Phase-field, microelastic modeling shows a strong competition between the geometric lattice strain confinement and the thermodynamic and kinetic energy minimization in forming the final structure.[149] This mechanism is mainly controlled by three important parameters: the film composition

variation, crystallographic anisotropy and the lattice mismatch accommodation between two phases and the substrate. More work is now needed both to further understand the fundamental growth mechanisms of (pseudo)-spinodal thin film systems, and to predict and experimentally verify new highly-ordered composite nanostructured film compositions.

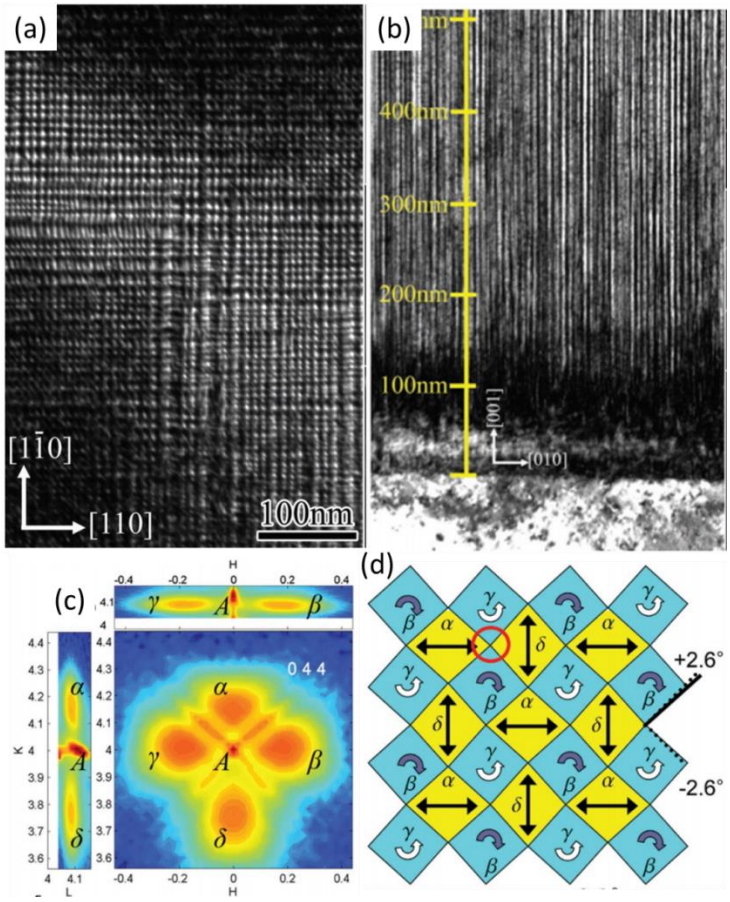

Figure 1.24. (a) Plan-view and (b) cross-sectional TEM images of a $ZnMnGaO_4$ film showing a highly ordered nano-chessboard structure. (c) Reciprocal space map near MgO (022) reflection and (d) a schematic diagram representing the CB domain formation. Rotated tetragonal (α, δ) and orthorhombic (β, γ) domains are represent blue and yellow squares, respectively.[148]

1.4.3 Vertical strain tuning in VAN thin films

In the film-on-substrate geometry, strain naturally occurs as a result of lattice mismatch between the film and the underlying substrate. The substrate-induced biaxial strain, either compressive or tensile depending on the relationship between the lattice parameters of the film and the substrate (Figure 1.25(a)),[118] can be maintained in ultrathin film up to several percent. It should be also noted that the substrate-induced coherent strain only exits up to a few tens of nanometers, after which structural boundaries appear and relax strain. While still using the lattice mismatch as the source of strain, the VAN architecture creates a high density of vertical interfaces that allow the high strain states maintained in thick films (Figure 1.25(b)).[118]

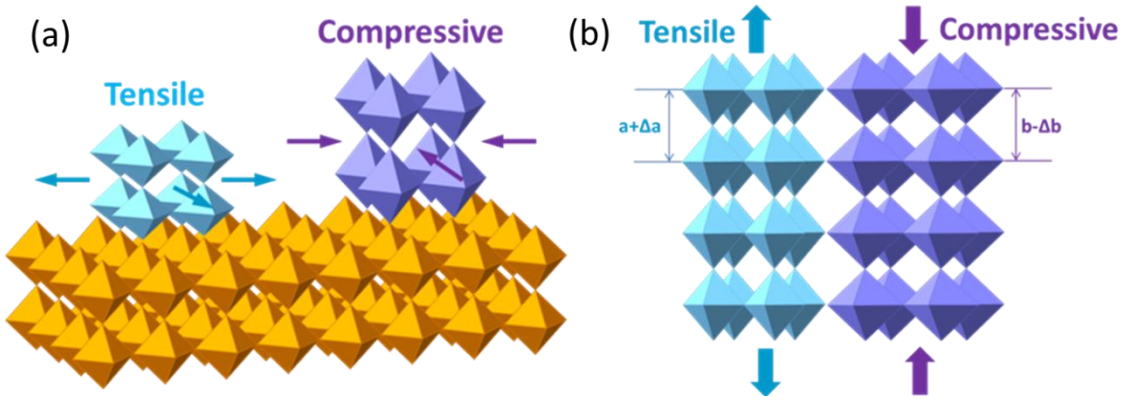

Figure 1.25. Schematics of (a) substrate-induced biaxial strain and (b) vertical lattice strain. a (or b) and Δa(or Δb) represent the original lattice parameter and the strained lattice parameter variation of individual phases.[118]

The vertical strain in VAN thin films can be tuned by adjusting the coupling phase, film composition, column width and deposition parameters. For example, the

vertical strain state of the LSMO (a_{LSMO}=3.87 Å) undergoes a transition from compressive in a pure film to tensile in LSMO:ZnO VAN films.[122] In another system of BFO:SmO VAN system (a_{BFO}=3.96 Å, a_{SmO}=10.93 Å), as the deposition frequency increases, the BFO column width decreases and so the vertical phase boundary density increases.[124] A more effective interface coupling occurs between BFO and SmO, which results in a vertical strain state transition in BFO from compressive to tensile with the increase of deposition frequency. It should be noted that vertical domain matching usually occurs at the vertical interface and partially relaxes the vertical strain. The three-dimensional heteroepitaxial geometry of the VAN thin films is favorable for maintaining a fully coherent strain from the matrix phase to the pillar phase, which may compensate the strain loss due to vertical domain matching at the interface. A vertical strain state as high as 2.35 % has been observed in the BTO:SmO VAN films.[114]

1.4.4 Functionalities of VAN thin films

Unique VAN architectures provide a new platform for functional oxide thin films and exhibit several key advantages, including simpler self-assembled growth, a higher density of vertical heterointerface and associated defects in some cases, effective vertical strain control and strong coupling effects. Thus a wide range of functionalities have been explored using the above VAN features. Table 1.3 summarizes representative examples using specific characteristics in VAN structure to achieve enhanced functionalities,[120] which include enhanced flux pinning in superconductors,[150,151] strain-enhanced ferroelectricity,[114] strain- and charge-coupled magnetoelectrics,[55,139] tunable

magnetotransport,[128-130,153] novel electric/ionic transport,[154,138] memoristors[137] and tunable dielectrics.[139]

Table 1.3. Epitaxial nanocomposite heterostructures grouped by crystal structure and functionalities

VAN Characteristics	**Defects engineering**	**Vertical strain control**	**Strong coupling effects**	**Vertical heterointerface**	**Vertical strain control & coupling**
Nanocomposite family/Functionalities	**Superconductors**	**Ferroelectricity**	**Multiferroics**	**Electronic and ionic transport**	**Dielectric and Optical**
Perovskite-related	$BaZrO_3$-$YBa_2Cu_3O_{7-\delta}$ (YBCO); $BaSnO_3$- YBCO; $BaHfO_3$-YBCO; Ba_2YTaO_6-YBCO; Ba_2YNbO_6-YBCO	$BaTiO_3$-Sm_2O_3; $BaTiO_3$-CeO_2; $BiFeO_3$-Sm_2O_3	$BiFeO_3$-$CoFe_2O_4$; $BaTiO_3$-$CoFe_2O_4$; $BiFeO_3$-$NiFe_2O_4$; La_2CoMnO_6-ZnO	$La_{0.7}Sr_{0.3}MnO_3$ (LSMO)-ZnO; LSMO-CeO_2; LSMO-Mn_3O_4; LSMO-NiO; $La_{1-x}Ca_xMnO_3$ -MgO, $SrTiO_3$-Sm_2O_3, $SrRuO_3$-ZnO	$Ba_{0.6}Sr_{0.4}TiO_3$ -Sm_2O_3 $SrRuO_3$-$CoFe_2O_4$
Layered oxides			$Bi_5Ti_3FeO_{15}$-$CoFe_2O_4$,		

1.4.5 Research challenges and future directions

Unique VAN thin films have provides new opportunities for enhanced performance and creation of multifunctional devices because of its great benefits as a novel thin film architecture: the self-assembly, the huge interfacial area for functional

coupling, and the vertical epitaxial strain control independent of the substrate. Research challenges in this area encompass three major subjects: materials architectonics (designing and growing the appropriate nanocomposite structures with tunable dimensions), materials chemistry (selecting appropriate materials system and compositions and understanding their chemical interactions) and materials physics (understanding the way how the materials couple, e.g. via strain, charge or others, and the impact on the physical properties). These three sub-areas need to feed into one another in a highly interdisciplinary way to ensure rapid progression of the field. Particularly important goals under these sub-areas are achieving a desired level of structural, chemical and electrical perfection, and manipulating the fundamental interactions ruling the physical properties.

Looking to the future, a huge scope is expected in this field and many other new phenomena and applications to be explored and exploited in future, some examples of which are illustrated in Figure 1.26. These involve mutual coupling between ferromagnetic/ferrimagnetic, FE/piezoelectric/dielectric, optical/plasmonic, thermal and strain effects, so that integrated multifunctionalities can be obtained. Careful elucidation of the operative coupling mechanisms of electronic, magnetic, thermal and optical order parameters will be very important in these systems.

Some applications will require highly-ordered arrays of phases in the nanocomposite. As well as bottom-up approaches to achieve this, namely (pseudo-)spinodal decomposition as discussed earlier, nanopatterning could also be incorporated for directed assembly.[155-157] Also, architectonic structures with 0D, 1D and 2D

dimensions could be explored to incorporate further functionality and tunability.[132,158] It should be further note that although most experience to date has been with functional oxides, non-oxide materials like metals or semiconductors with all their additional wide-ranging functionalities, should be explored.[159,160]

In addition to coupling of properties *across* interfaces, directed charge transport (electronic and ionic) channels *along* interfaces could lead to new forms of exchange and tunneling effects, ionitronic and phase transition effects, and thermal and optical modulation effects. To accelerate the understanding of the interface effects, probing of local charge carrier transport controlled by external stimuli should be explored.

Finally, functionalities are not limited to the listed ones in Figure 1.26.[120] Given the simple self-assembly and fascinating functionalities achievable, heteroepitaxial nanocomposite films offer a novel platform in designing advanced solid state devices, from macro/nano capacitors to nanoscale tunnel junctions and many others besides. There are very many unknown aspects to the field, and hence, even though we have come a very long way in the last 10 years, there are many avenues still to be explored, from theory to modeling to growth, and ultimately to practical device demonstrations in new systems with wide functional possibilities.

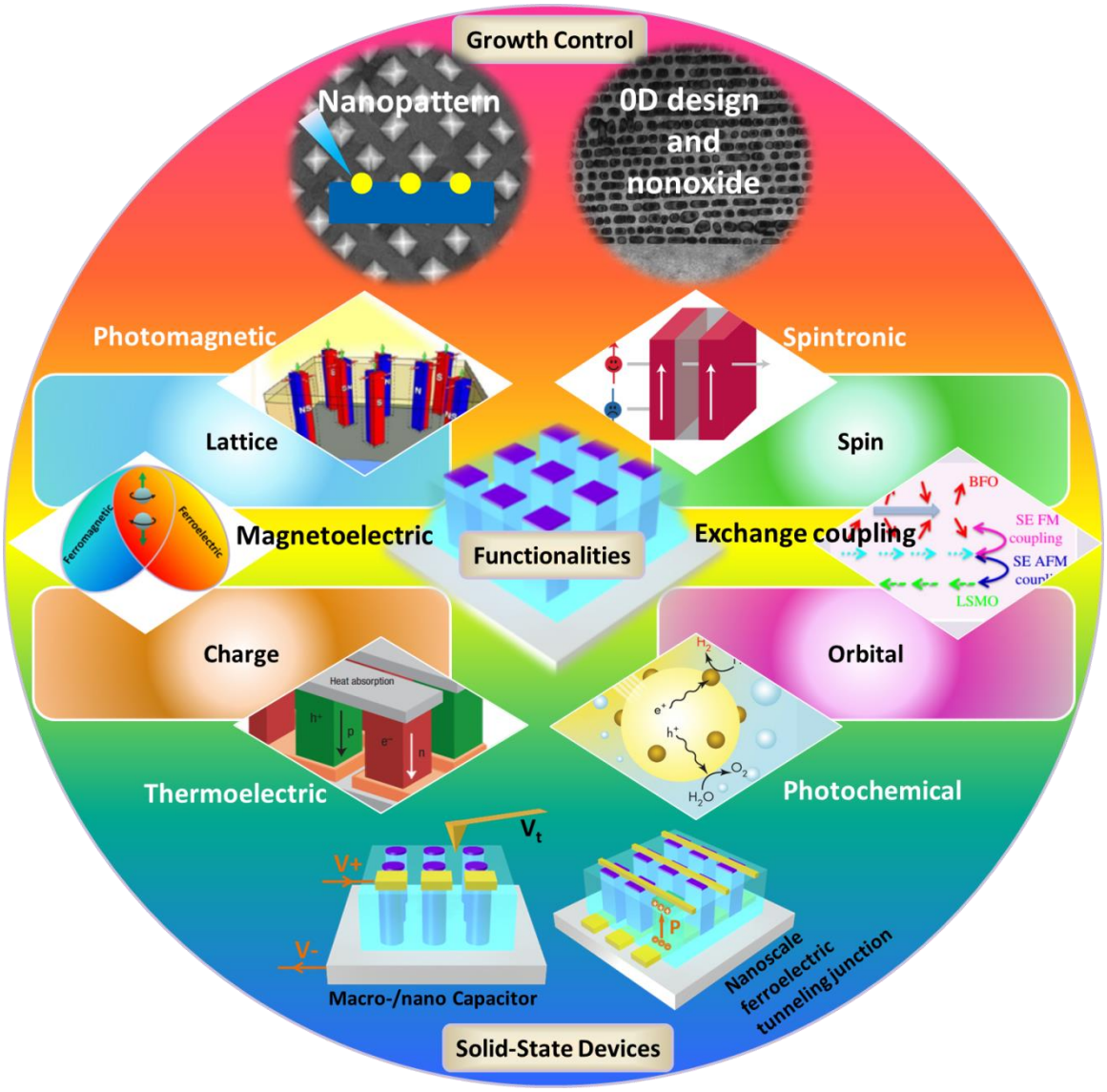

Figure 1.26. Research prospects for multifunctional heteroepitaxial nanocomposite films with a focus on the vertically aligned nanoarchitectures. Special emphasize is given from directed growth control, exploration of new materials to multifunctionalities and solid-state devices. Note: AFM, antiferromagnetic; FM, ferromagnetic; SE, superexchange. P is the FE polarization, V_t is the tip bias. V^+ and V^- represent the external positive and negative voltage applied on the VAN film, respectively.[120]

CHAPTER II

RESEARCH METHODOLOGY

2.1 Pulsed laser deposition

PLD is one of the major PVD methods for thin film growth.[161] It has been demonstrated as a powerful method for the high-quality growth of complex oxide films like YBCO. PLD has been used as the thin film growth technique in our work. Figure 2.1 shows the schematic set-up of PLD, which consists of a laser system and a vacuum chamber with a substrate holder and a rotating target holder. Excimer lasers with different wavelengths (157 nm, 193 nm, 248 nm, 308 nm and 351 nm) are commonly used in thin film deposition. Usually the laser with a short wavelength leads to more effective ablation. The parameters of the laser used in our work are 248 nm in wavelength, 1-10 Hz in laser repetition frequency, 20-25 ns in pulse duration and 300-450 mJ in energy. Before the laser-ablation process, the vacuum chamber is pumped to be at least 1.0×10^{-6} mbar. Substrate temperature and oxygen pressure are adjusted for optimum film growth condition, which are 650-750 ℃ and 20-200 mTorr of oxygen in our experiments. A bulk ceramic target is placed at an angle of 45 ºto the incident laser beam and right in front of the substrates with a distance of ~5 cm. When the temperature and oxygen pressure are ready, a high-energy laser beam is focused onto the rotating target by focus lens in the optical path. The laser-ablated portion in the target absorbs the laser energy, and materials are dissociated from the target surface and form a plasma.

The plasma plume transfer materials from the target to the substrate surface and form the thin film.

The PLD process involves complicated physical phenomena such as collisional, thermal and electronic excitation, material evaporation, ablation, excitation, plasma formation, and exfoliation. Generally it can be described as the following four steps: (1) Interaction of the laser beam and the target surface for the evaporation of target materials; (2) Interaction of vaporized materials with the incident laser beam for an isothermal plasma formation and expansion; (3) Transportation of plasma on the substrate surface at a given growth condition; (4) Thin film growth of adatoms on the substrate surface. Thus how to control the above steps is important to grown a high-quality film in terms of surface coverage, roughness, uniformity, crystallinity and stoichiometry. The growth parameters can be optimized accordingly, which include substrate temperature, oxygen pressure, target-to-substrate distance, laser energy repetition rate and energy density. The growth temperature closely relates to the film crystallinity and phase separation in the growth of nanocomposite films. Oxygen pressure strongly affects the growth rate, film surface and phase formation in some material systems. The substrate parameters are also important for thin film growth, which include substrate orientation, surface roughness, miscut angle and atomic surface termination.

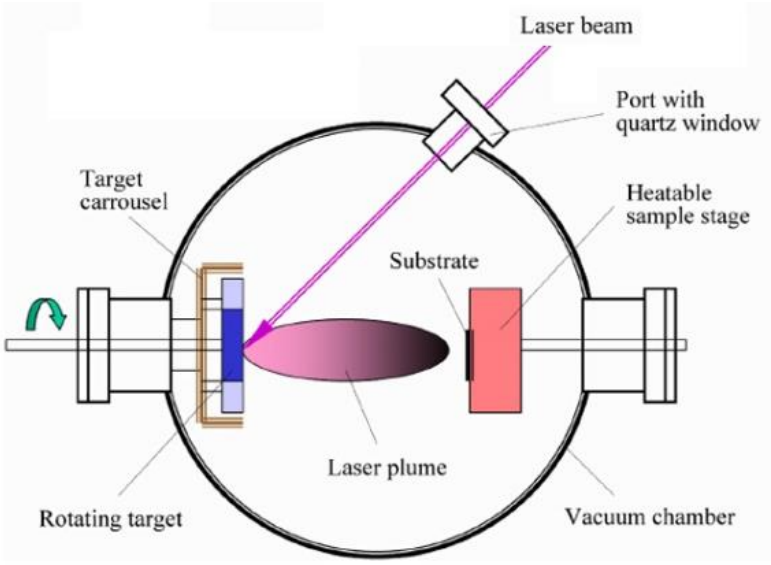

Figure 2.1. Schematic experiment set-up for a pulse laser deposition system

PLD has many advantages compared to other deposition techniques. First, it achieves a good stoichiometric transfer from the target to deposited films, because the target plume generated by the high-energy and ultrafast laser pulse is transferred instantly to the substrate and the effect of different deposition rates of each component is minimized. This capability makes PLD as a very versatile tool for the growth of a wide variety of materials, including oxides, semiconductors, metals and even polymers. Thus all required is a target of the desired composition, which is quite different from other methods like CVD or MBE requiring a good selection of precursors for each element to obtain a targeted phase. For the growth of nanocomposite films, one can tune the mixture ratio of different phases in the target in order to grow films with desired composition. A recent deposition method called the combinatorial deposition uses two single-phase targets to grow nanocomposite films, which alternatively ablates the single

target phase into the nanocomposite films. This method provides a convenient method for the composition control of the nanocomposite films compared to the conventional single target method. Second, the growth control of PLD is simple, which is mainly achieved by tuning the substrate temperature, oxygen atmosphere, laser energy density and repetition rate, so that the optimization for the deposition process is much easier. Third, PLD is a cost-effectiveness method. Multiple chambers can share one laser source by using beam splitters and lens. Last, PLD is a fast and clean process for the growth of thin films.

The disadvantages of PLD include two major parts. First, the splashing process associated with laser ablation could bring particulates or particles from the target to the substrate surface, which degrades the film quality. This can be solved by using a high-quality method, controlling laser energy and growth velocity. Second, the scaling-up capability of PLD is limited, since the laser-ablated plasma is highly directional and only covers very local area. Developments of advanced PLD systems are required.

2.2 Structural characterization

2.2.1 X-ray diffraction

X-ray diffraction (XRD) is one of the most widely used nondestructive techniques for crystal structure analysis.[162] It provides a fast and reliable analysis of crystal orientation, crystallinity and lattice constant. For the thin film analysis, it is also used for lattice strain and growth relationship between the film and the substrate. Figure 2.2(a) shows a schematic set-up for a XRD instrument, which consists of an incident X-ray source, a sample stage and a detector. Diffraction occurs when the wavelength of an

incident beam is in the same order of the repeated distance in a crystal, as shown in Figure 2.2(b). The diffraction obeys Bragg's law：

$$n\lambda = 2d\sin\theta, \tag{2.1}$$

where n is an integral, λ is the wavelength of the incident X-ray, d is the crystal lattice spacing and θ is the diffraction angle.

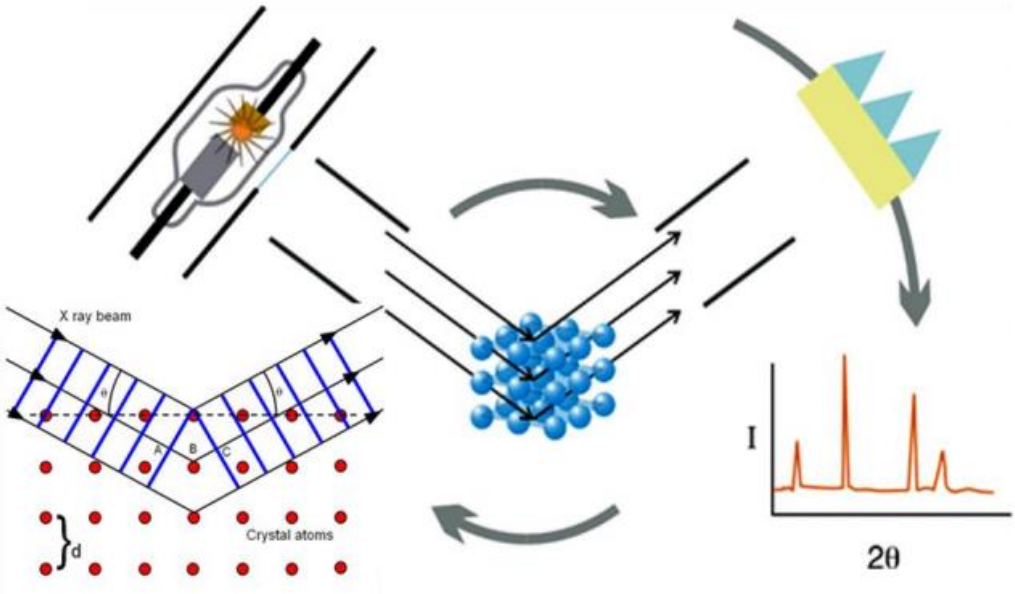

Figure 2.2. (a) Schematic set-up for a X-ray diffraction instrument containing a X-ray source, a sample stage and a X-ray detector. (b) Schematic of diffraction for a crystal with an interspacing of d. (c) A schematic XRD pattern for a crystalline sample.

The XRD pattern is very sensitive to the structure and crystallinity of the test sample. For an amorphous sample with no specific orientations, no diffraction peak is formed. For a polycrystalline sample, diffraction peaks with non-uniform or irregular

spacing appears (Figure 2.2(c)). For a single-crystal sample, a series of diffraction peaks with a periodic spacing is formed. The lattice constant can be calculated form the diffraction peak spacing. The crystallinity can be analyzed from the peak spread, where a term called the full width at half maximum (FWHM) is introduced for this purpose. A smaller FWHM means a higher crystallinity. In strained crystals or thin films, the diffraction peak shift is observed compared to that in its original state. Thus strain analysis can be conducted based on the peak shift. The major XRD techniques for thin film analysis used in this study includes θ-2θ scan, ω scan (rocking curve), phi scan, and reciprocal spacing map (RSM). θ-2θ scan is used to study the c-axis crystalline relationship of the film with respect to the underlying substrate. ω scan is used to determine film crystallinity (lattice distortion). Phi scan is used to analyze the in-plane growth relationship of the film on the substrate. RSM is a collective result of a number of ω-2θ scans, which is used to determine the lattice constant, crystallinity and strain distribution.

2.2.2 Scanning electron microscopy

When an electron beam interacts with a solid specimen, various signals are generated out of the samples, such as secondary electrons (SEs), back-scattered electrons (BSEs), Auger electrons, characteristic X-rays, visible light and heat and others, as shown in Figure 2.3.[163,164] These signals contain different sample information such as surface morphology, texture, phase distribution and chemical composition.

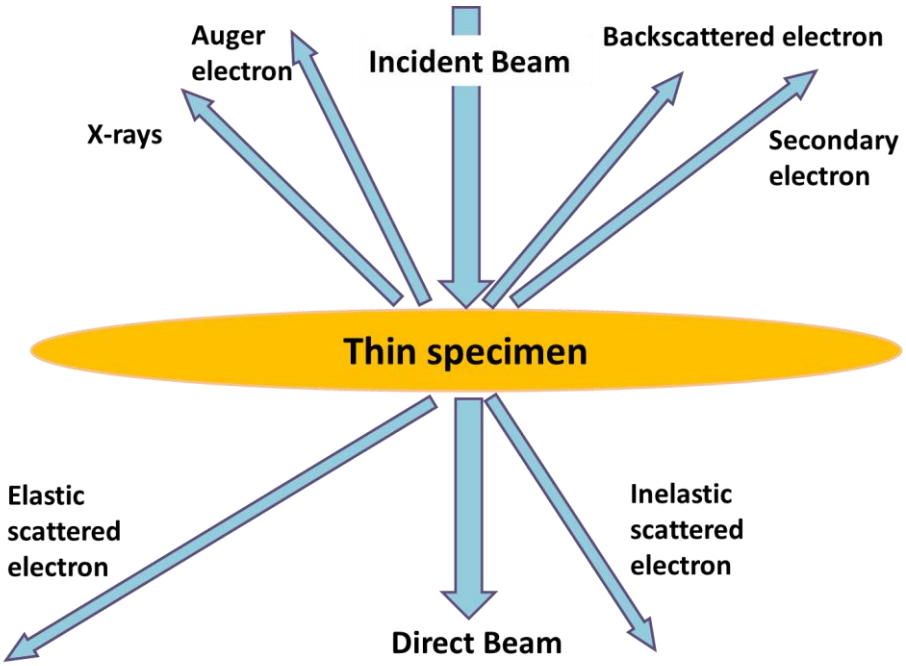

Figure 2.3. Schematic of electron beam-sample interaction for a thin specimen in both forward and back directions.

The scanning electron microscopy (SEM) uses a focused high-energy electron beam (5 kV-20 kV) to scan over a sample surface and collect a two-dimensional image. Figure 2.4 shows the schematic set-up of a SEM. SEs and BSEs are commonly collected for the SEM analysis. SE images provide valuable information of sample morphology and topography. BSE images are used for phase distribution analysis. Characteristic X-rays are generated by inelastic collision of incident electrons with electrons in the analyzed sample, which reflect elementary information. Energy dispersive X-ray analysis is also available in most SEM for the sample elemental analysis.

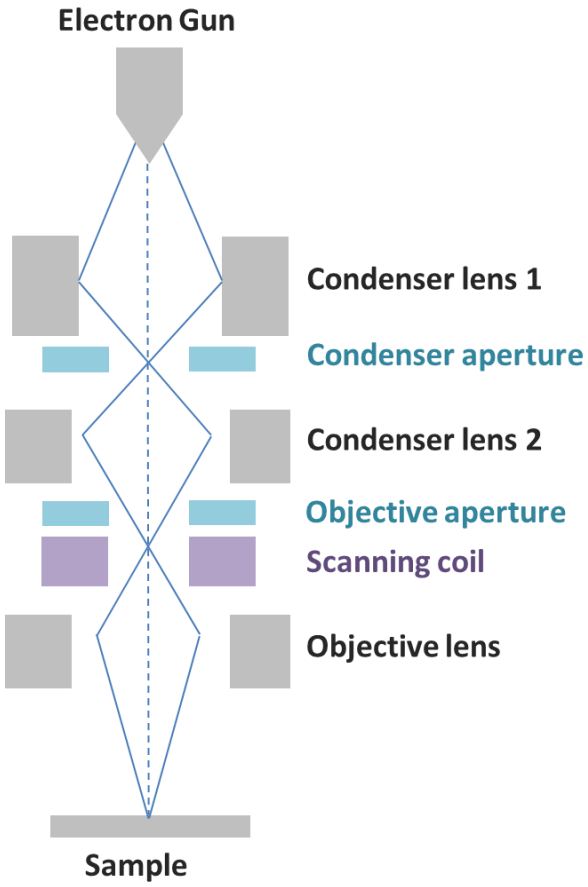

Figure 2.4. Schematic set-up of scanning electron microscopy

2.2.3 Transmission electron microscopy

TEM is a powerful tool for microstructure characterization because of its strong capability for high-resolution imaging of crystal structure.[165] Historically, TEM was developed to use an electron beam to replace the visible light source, which imposes a resolution limit because of the visible light wavelength. Figure 2.5 shows two basic operation modes of TEM: the diffraction mode and the imaging mode. The switch between two different modes is conducted by changing the focal length to first image

plane (imaging mode) or the back focal plane (diffraction mode) of the objective lens. Each mode offers a different insight about the sample. The imaging mode provides a highly magnified and thus local view of the atom-scale arrangement in the sample. To obtain high-resolution TEM images, the specimen should be titled to a correct zone axis, and the objective lens should be adjusted to have the shortest focal length. The diffraction mode provides the structural information including the crystal structure and lattice parameter. For most TEM imaging, appropriate objective apertures are inserted at the back focal plane of the objective lens to increase the diffraction contrast.

Up to today, TEM have become more versatile with more incorporated analytic techniques besides conventional imaging, such as high-angle annular dark field (HAADF) scanning transmission electron microscope (STEM), EDX and electron energy loss spectroscopy. In HAADF STEM mode, the image contrast is proportional to $\sim Z^2$, where Z is the atomic number. Thus it provides a direct interpretation of different phases.

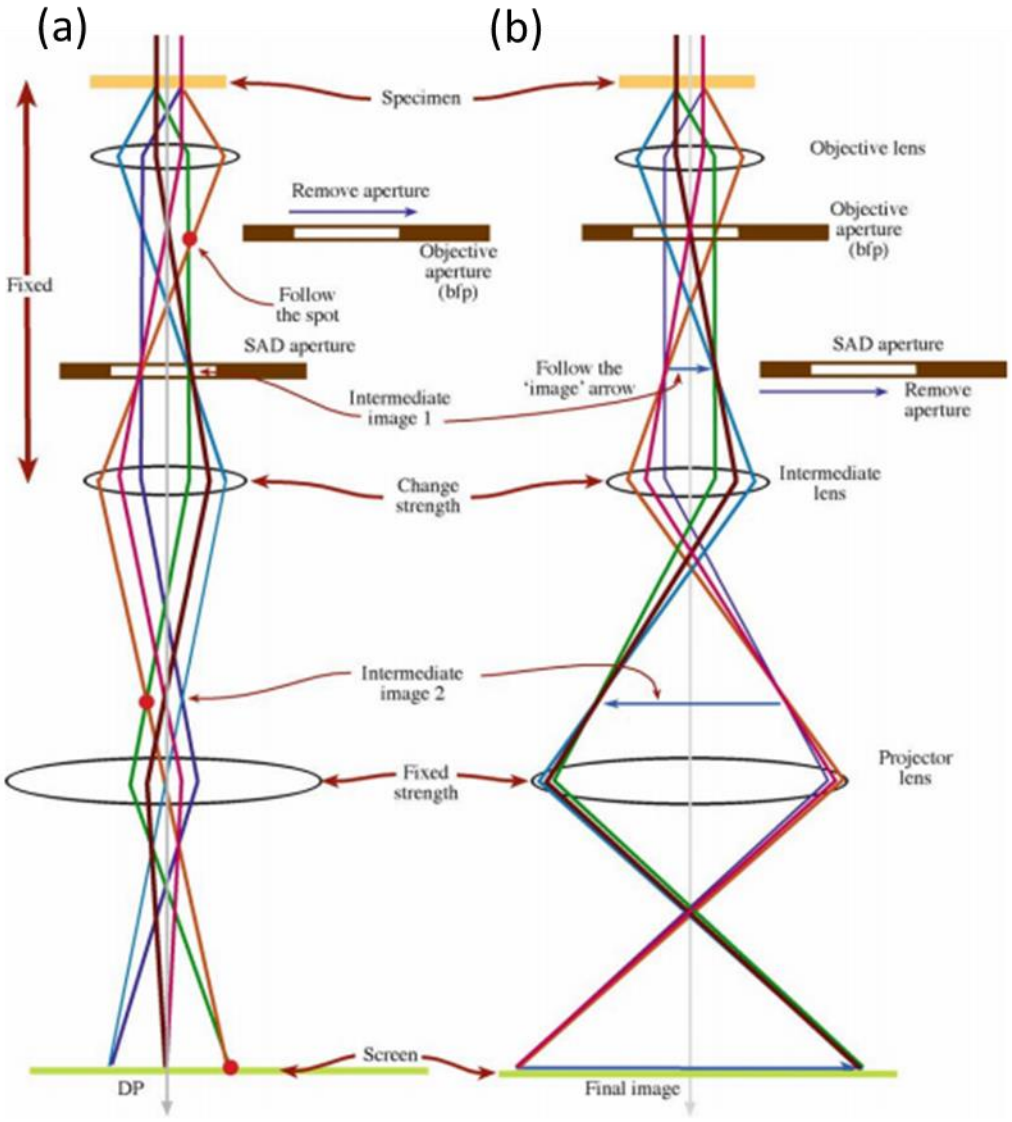

Figure 2.5. Two basic operation modes of transmission electron microscopy. (a) Diffraction mode. (b) Imaging mode.

TEM sample preparation is very important for reliable and high-effective TEM imaging. The main challenge of this work is obtain a sufficiently thin region with the thickness less than 100 nm in order to become electron transparent, while maintaining the original structure. The TEM samples in this dissertation are prepared with the

following procedure: (1) cutting thin slices from a bulk sample; (2) gluing two slice samples face-to-face with the film side sandwiched in the middle for cross-sectional sample; gluing one slice sample with the substrate facing outside for plan-view sample; (3) thinning the glued samples to ~40-50 μm; (4) grinding and polishing to ~20-25 μm; (5) ion milling to a central hole appearance. In this way, a thin area with a thickness below 100 nm has been obtained around the hole.

2.2.4 Atomic force microscopy

AFM is a high-resolution scanning probe microscopy, which has demonstrated as a fast and accurate technique for surface morphology and topography analysis.[166] Figure 2.6 shows a schematic set-up of an AFM instrument. During the AFM operation, a tip with a radius of ~20 nm positioned at the end of the cantilever is scanned over the sample surface. The tip deflects up and down when it scans on surface positions with different surface heights. At the same time, the tip deflection is detected by the laser and is recorded by the electric system for the sample surface imaging. The contact mode was commonly used for the AFM topography measurement, in which an AFM tip is in soft physical contact with the surface during the entire scanning. The continuous mechanical contact, in some cases, damages the sample surface and increases the tip wear. The tapping mode has thus been introduced. In the tapping mode, the cantilever is driven by a small piezoelectric element to oscillate up and down near its resonance frequency, which allows a very short-time interaction with the sample. When the tip comes close to the sample surface, the short-range force, including Van der Waals forces, electrostatic forces, dipole-dipole interactions and others, decreases the tip oscillation and generates a

local surface signal to the external system. In this way, the tapping mode AFM achieves a similar level of resolution on surface morphology and becomes less destructive to both sample surface and tips.

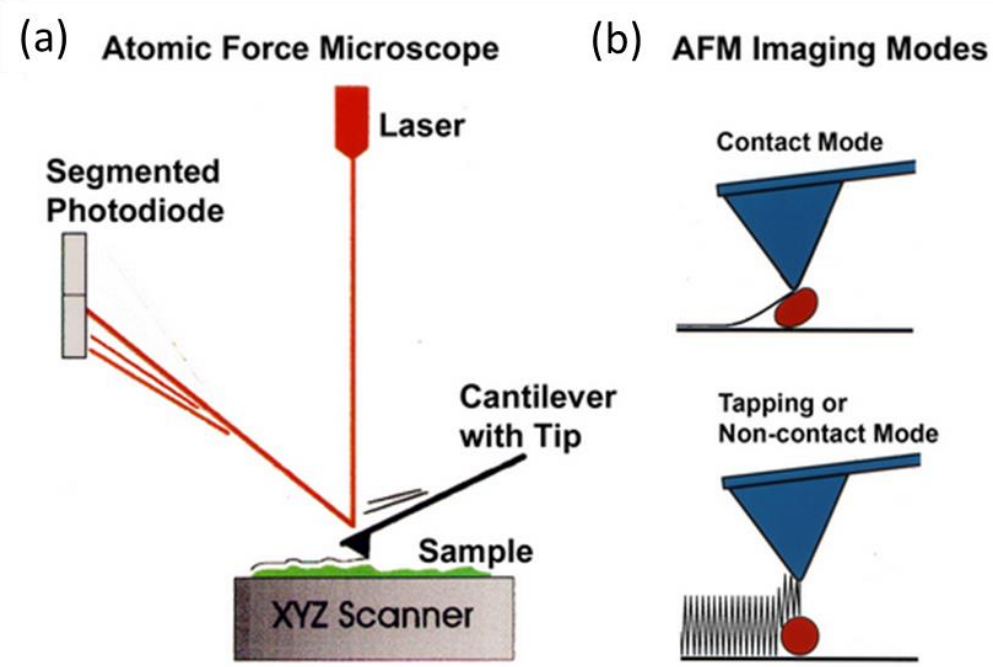

Figure 2.6. (a) Schematic set-up for an atomic force microscope. (b) Contact mode and tapping mode for AFM topography measurements.

In addition to detect the surface morphology and topography, modern AFM has integrated a lot more functionalities for a variety of measurements ranging from nanomechanical, electric/piezoelectric and magnetic characterization. A special focus is given on piezoelectric force microscopy (PFM), which has been widely used in the nanoscale mapping of FE domain structure, domain writing and piezoelectric phase and

amplitude measurements. Figure 2.7 shows the schematic of piezoelectric force measurement on a piezoelectric material with two neighboring domains with opposite phases. When the tip is scanning from position A to B, different phases cause opposite vertical deflections of the AFM tip, which give rises to a 180 degree of change in phase and the same amplitude.

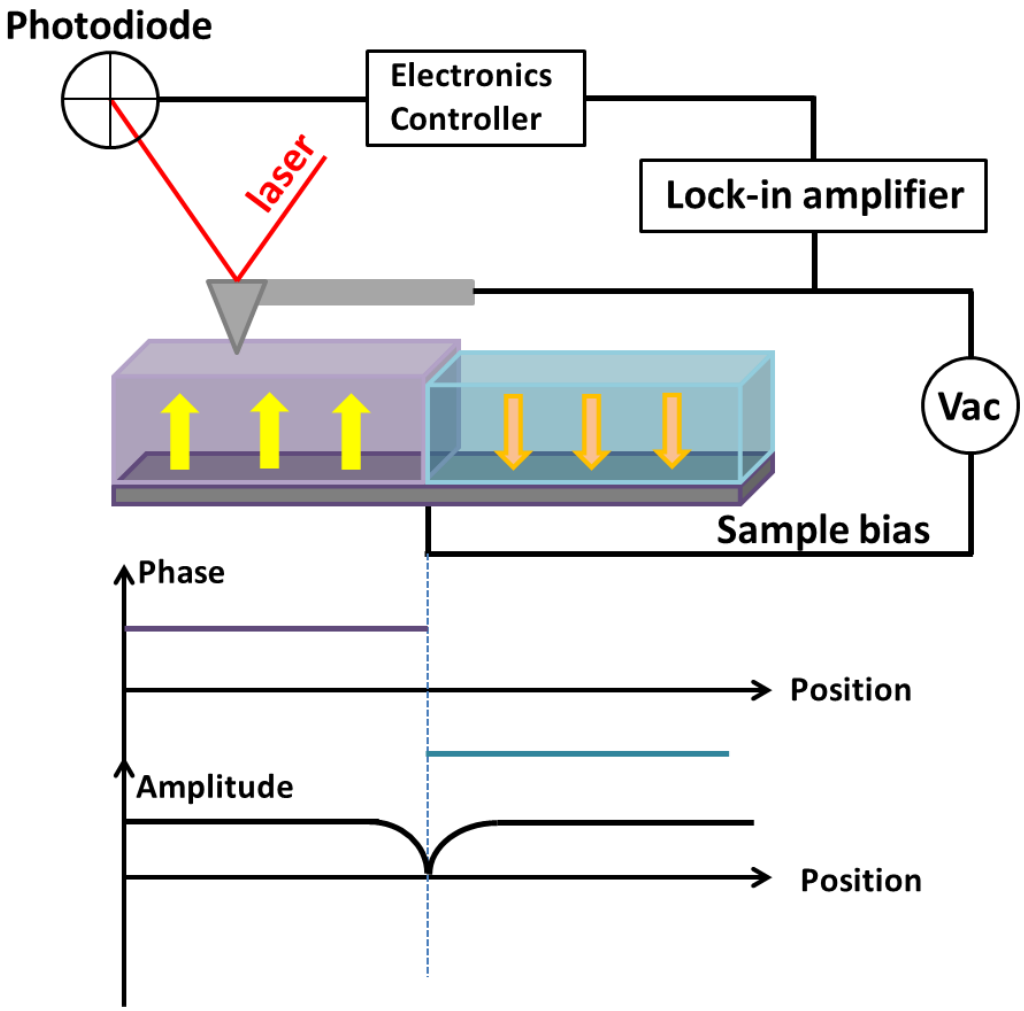

Figure 2.7. Schematic of piezoelectric force measurement on a piezoelectric material with two neighboring domains with opposite phases.

2.3 Magnetic and magnetotransport measurements

Magnetic and magnetotransport measurements have been conducted in a Physical Property Measurement System (PPMS Model 6000, Quantum Design) with vibrating sample magnetometer (VSM) and resistivity options. The PPMS provides a powerful workstation that controls magnetic fields from -9 T to 9 T and temperature from 1.9 – 400 K using liquid He and heater. The temperature sweep rate ranges from 0.01 K/min to 12 K/min. Superior temperature control within ±2 mK is achieved in this system assisted by a monitor thermometer adjacent to the sample.

The VSM option is a fast and sensitive direct current (DC) magnetometer and has a linear motor to vibrate the sample in the PPMS chamber. A pair of electromagnets is used to generate a DC magnetic field, and a pick-up coil is used to acquire the sample signal. During VSM measurements, the sample is mechanically vibrated up and down at a constant frequency (40 Hz). Such vibration generates a magnetic flux change, which is converted to an equivalent alternative current (AC) voltage in the pick-up coil. The VSM measurement sensitivity is less than 10-6 emu with 1 second averaging.

The resistivity option provides two measurement options: AC transport and DC resistivity. AC transport option is optimized for measuring highly conducting materials like metals with a typical resistance from nΩ to kΩ. DC resistivity option is preferred to measured conducting materials with a resistance of Ω to MΩ. The maximum resistance can be measured in our system is close to $5x10^6$ Ω. Both measurements support four terminal connections. For in-plane magnetotransport measurements, the resistance is

measured with four point connection in van der pauw geometry. For out-of-plane transport measurements, the resistance is conducted by a two-point connection.

CHAPTER III

INTEGRATION OF SELF-ASSEMBLED VERTICALLY ALIGNED NANOCOMPOSITE $(La_{0.7}Sr_{0.3}MnO_3)_{1-x}:(ZnO)_x$ THIN FILMS ON SILICON SUBSTRATES[1]

3.1 Overview

In this chapter, epitaxial $(La_{0.7}Sr_{0.3}MnO_3)_{1-x}:(ZnO)_x$ ($LSMO_{1-x}:ZnO_x$) in vertically aligned nanocomposite (VAN) form were integrated on STO/TiN buffered silicon substrates by pulsed laser deposition. Their magnetotransport properties have been investigated and are systematically tuned through controlling the ZnO concentration. The composite film with 70 % ZnO in molar ratio exhibits the maximum MR value of 55 % at 70 K and 1 T. The enhanced tunable LFMR properties are attributed to structural and magnetic disorders and spin-polarized tunneling through the secondary ZnO phase. The integration of LSMO:ZnO VAN films on silicon substrates is a critical step enabling the application of VAN films in future spintronic devices.

[1] This chapter is reprinted with permission from "Integration of self-assembled vertically aligned nanocomposite $(La_{0.7}Sr_{0.3}MnO_3)_{1-x}:(ZnO)_x$ thin films on silicon substrates" by W. Zhang, et al., ACS Applied Materials & Interfaces, 2013, 5, 3995-3999.

3.2 Introduction

Strongly correlated complex oxides have generated a wide spectrum of intriguing phenomena because of the interactions of charge, spin, orbital and lattice degree of freedom across their heterointerfaces, including unusual electronic reconstruction at adjoined heterointerfaces,[7] colossal MR[167] and, more recently, multiferroic interface coupling.[168] This has led to extensive research on exploration of the fundamental physics, epitaxial design of hetero-interfaces based on atomic terminations and the ultimately diversified functionalities for potential devices.[169] However, most of previous study focused on heteroepitaxial layer-by-layer assembly because of its fine control of film compositions and configurations,[170,171] and the research on vertically aligned structures and their vertical interfacial coupling effects is new and scarce. An early vertical two-phase oxide system was demonstrated in LCMO:MgO thin films in an effort to investigate the structure transition of LCMO phase.[121] Afterwards, the morphology dependence of BFO:CFO nanostructures on substrate orientations was reported, which provided an effective platform for further study of ME coupling.[115]

Self-assembled VAN thin films were first introduced in BFO:Sm_2O_3 and LSMO:ZnO systems through careful materials selection and microstructure control.[122] Unique and new functionalities also arise from such ordered structures, such as reduced clamping effect from substrates and more efficient interfacial coupling.[116,117] For example, a very large vertical tensile strain was maintained in the BFO:Fe_3O_4 VAN films, resulting in enhanced saturation magnetization compared to its bulk value.[172] Meanwhile, tunable vertical lattice strain and dielectric property control in $BiFeO_3$:Sm_2O_3,[124] LFMR

in LSMO:ZnO[128,129] and LSMO:CeO_2,[130] and multifunctionality in PTO:CFO films have also been demonstrated in VAN systems.[134] Although the research on functional oxides has made tremendous progress in the past decades, most of VAN studies focus on films grown on single crystal perovskite and perovskite-related oxide substrates, including STO, LAO, DSO, NGO, etc., to achieve high epitaxial quality.[173] Such single crystal substrates are expensive and in small dimension, thus not desirable for large-scale integration of oxide thin films with conventional semiconductor devices. Therefore, it is highly attractive to grow these unique VAN thin films on traditional semiconductor substrates such as silicon (Si) while maintaining satisfactory performance. Unfortunately, direct growth of functional oxides on Si often fails to achieve highly epitaxial films because of oxidation on Si during high temperature deposition and the large lattice mismatch. One possible solution is to grow buffer layer to provide structural compatibility, thermal stability, and chemical stability between thin films and underlying substrates.[174] The buffer layers demonstrated are STO,[175] yittra-stabilized zirconia (YSZ)/YBCO,[176] $Bi_4Ti_3O_{12}/CeO_2$/YSZ,[177] etc.

In this work, for the first time, we demonstrate the integration of epitaxial VAN films on Si substrates using a bi-layer buffer structure. For this demonstration, LSMO:ZnO VAN system has been selected for this study based on our prior success in growing $(LSMO)_{0.5}$:$(ZnO)_{0.5}$ VAN films on single crystal STO substrates with tunable LFMR property.[128] The TiN/STO bi-layer buffer layer has been deposited to avoid surface oxidation and reduce the lattice mismatch between VAN films and underlying substrates. The magnetotransport property of the as-deposited VAN thin films has been

investigated, which shows comparable performance to those grown on STO single crystal substrates. Therefore, this work demonstrates promises in bridging the gap to integrate VAN films in future spintronic devices.

3.3 Experimental method

The composite targets with different composition ratios were prepared by conventional ceramic sintering method. In brief, the stoichiometric mixture of high purity La_2O_3, $SrCO_3$ and MnO_2 powders were ground, pressed and then sintered at 1200 ℃ for 24h to synthesize LSMO powders. The calcined LSMO powders were then mixed with ZnO powders in different ratios and pressed into disks and subsequently sintered at 1300 ℃ for 12h to make the composite targets. TiN and STO buffer layers and $L_{1-x}Z_x$ thin films were deposited subsequently on Si (001) substrates by PLD at a base pressure of 1.5×10^{-6} Torr. The substrate temperature was set at 750 ℃ for all deposited films. And the TiN buffer layer and STO buffer layer were grown at vacuum and the oxygen pressure of 40 mTorr, respectively. The composite films were deposited at an optimized oxygen pressure of 200 mTorr. After deposition, the composite thin films were cooling down in 200 Torr oxygen at a cooling rate of 10℃/min.

The composition and microstructure of as-prepared films were investigated by XRD (PANalytical Empyrean XRD), TEM (FEI Tecnai G2 F20) operated at 200 kV. Cross-section samples for TEM observation were prepared by a standard manual grinding and thinning of samples with a final ion-milling step (Gatan PIPS 691 precision ion polishing system). For electrical property measurement, Au electrodes were deposited by sputtering on top of thin films with shadow mask method. The

conventional four-probe resistivity method was used to test resistivity of as-deposited samples with a commercial PPMS (Quantum Design, Model 6000). The test temperature was chosen to be in the range of 20 K-340 K and the magnetic field was up to 1 T.

3.4 LSMO:ZnO film growth and microstructure

Figure 3.1(a) shows the typical XRD pattern of a $LSMO_{0.3}$:$ZnO_{0.7}$ ($L_{0.3}Z_{0.7}$) thin film on Si substrate buffered with TiN/STO bilayer. For comparison, the XRD pattern of a pure LSMO thin film grown on Si substrates is also shown. It is obvious that the peaks from LSMO and STO in $L_{0.3}Z_{0.7}$ composite films are almost the same as those in pure LSMO film, indicating that there is no reaction or impurity phase in the composite thin films. Both the LSMO phase and the STO buffer layer have grown preferentially along [00l] orientation, while the ZnO phase has oriented along the $[11\bar{2}0]$ orientation. A small peak from TiO_2 (004) was observed which is possible from minor oxidation of TiN layer when depositing STO in oxygen atmosphere. No peak from the TiN buffer was identified in the complete XRD θ-2θ scan possibly due to the very thin TiN layer. Figure 3.1(b) gives the phi scans of Si (202), LSMO (202) and ZnO $(10\bar{1}0)$ planes. It is interesting to note that LSMO ($d_{\text{LSMO }<100>}$ = 3.87 Å) has achieved epitaxial cube-on-cube growth on Si ($d_{\text{Si}<100>}$ = 5.43 Å) without any rotation assisted by the bi-buffer layer. This is due to the big lattice mismatch of Si-TiN (24.6 %) and TiN-STO (7.9 %), which led to direct domain-matching growth of STO ($d_{\text{STO}<100>}$ = 3.96 Å) and TiN ($d_{\text{TiN}<100>}$ = 4.24 Å) on Si substrates. The vacuum-deposited TiN layer also acts as oxygen diffusion barrier and protects underlying substrates from oxidation, which usually causes serious problem for epitaxial growth of oxides on Si substrates. The phi scan of hexagonal ZnO phase

exhibits a four-fold symmetry, which suggests two possible matching relationships with the buffer layer. Thus the orientation relationships between the VAN films, buffer layers and Si substrates are determined to be

$(001)\text{LSMO} \parallel (11\bar{2}0)\text{ZnO} \parallel (001)\text{STO} \parallel (001)\text{TiN} \parallel (001)\text{Si}$ (for out-of-plane),

$[110]\text{LSMO} \parallel [0001]\text{ZnO} \parallel [110]\text{STO} \parallel [110]\text{TiN} \parallel [110]\text{Si}$, and

$[1\bar{1}0]\text{LSMO} \parallel [0001]\text{ZnO} \parallel [1\bar{1}0]\text{STO} \parallel [1\bar{1}0]\text{TiN} \parallel [1\bar{1}0]\text{Si}$ (for in-plane).

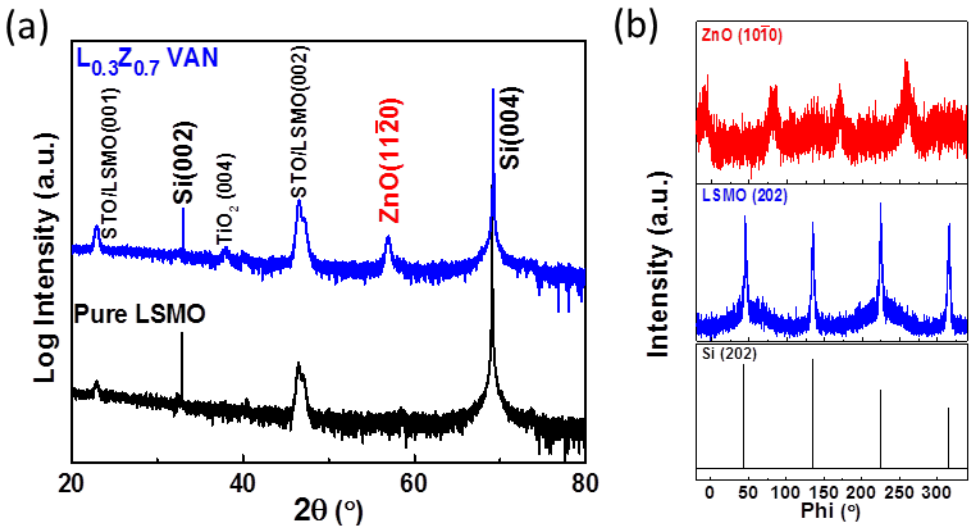

Figure 3.1. (a) XRD patterns of pure LSMO and $L_{0.3}Z_{0.7}$ composite thin films. (b) Phi scans of Si (202), LSMO (202) and ZnO (10$\bar{1}$0) planes

The low magnification bright-field transmission electron microscopy (TEM) image of $L_{0.3}Z_{0.7}$ VAN film shown in Figure 3.2(a) demonstrates that the self-assembled growth of LSMO and ZnO columns has been achieved on buffered Si substrates. And

the thickness of TiN, STO buffer layer and $L_{0.3}Z_{0.7}$ film is determined to be about 15 nm, 100 nm and 220 nm, respectively. The arrows indicate the abrupt interfaces between each layer. The corresponding selected-area electron diffraction (SAED) pattern is shown as the inset. The distinct diffraction dots from LSMO and ZnO suggest clear phase separation in VAN films. Figure 3.2(b) shows a high resolution TEM (HRTEM) image of the interfaces between buffer layer and substrates. A very thin SiO_2 layer of 3 - 5 nm was observed, which is possible due to minor oxidation of Si substrates as they approached to target deposition temperature. And the TiN and STO layers have maintained epitaxial growth on Si substrates and no diffusion was observed between these layers. The high resolution TEM (HRTEM) image in Figure 3.2(c) reveals high quality epitaxial growth of the LSMO and ZnO nanocolumns on the Si substrates. Both LSMO and ZnO phases have been marked out based on their lattice parameter, indicating clear phase separation. Figure 3.2(d) gives a plan-view TEM image of the $L_{0.3}Z_{0.7}$ composite thin film, which shows ordered alternative growth of LSMO and ZnO domains. Therefore, all the above results demonstrate that epitaxial LSMO:ZnO VAN films have been successfully grown on Si substrates.

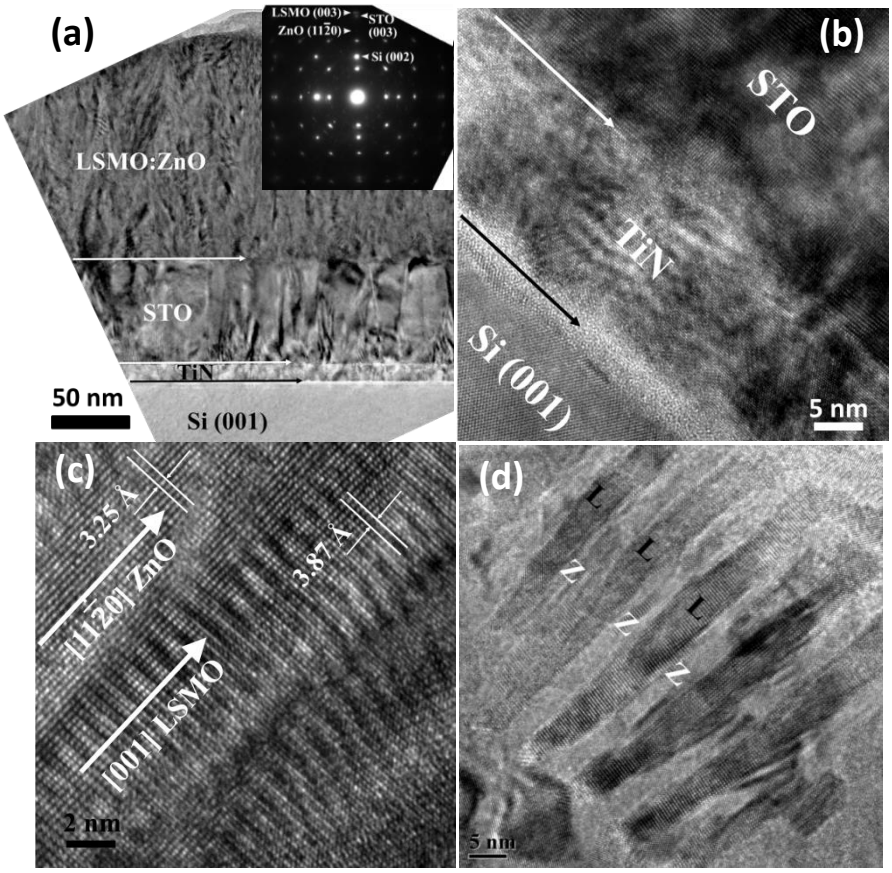

Figure 3.2. (a) Cross-sectional TEM image of $L_{0.3}Z_{0.7}$ VAN film; Inset: the corresponding SAED image of $L_{0.3}Z_{0.7}$ VAN film. (b) HRTEM image of interfaces between Si substrate and buffer layers. (c) Representative high resolution cross-sectional and (d) plan-view TEM image of $L_{0.3}Z_{0.7}$ VAN film. LSMO and ZnO are marked as L and Z respectively, in the above figures.

3.5 Resistivity and magnetotransport properties of LSMO:ZnO VAN films

To investigate the effect of ZnO phase on the magnetotransport property of the composite thin films, the in-plane resistivity measurement has been conducted for all samples. Figure 3.3(a) shows a schematic drawing of $L_{1-x}Z_x$/STO/TiN/Si field effect device, which was used to measure the sheet resistance as a function of the magnetic

field and temperature. This spintronic device could act as a basic cell to be integrated for magnetic random access memory, which offers significant advantages such as nonvolatile memory, increased data processing speed and integration density, to conventional data storage device. The temperature dependence of the normalized zero-field resistivity of $L_{1-x}Z_x$ composite thin films with different ZnO concentrations is compared in Figure 3.3(b). Well-defined metal-insulator transitions (MIT) are observed for samples with ZnO molar ratio less than 50%, after which their resistivity becomes too large for measurement and exhibits insulating-like behavior in the entire test temperature range. It is reasonable to consider that ρ is significantly affected by the insulating ZnO phase as the overall resistivity increases as ZnO concentration increases. Meanwhile, the grain and phase boundaries play an important role as scattering regions for transport properties in the ZnO rich composite films, thus increasing the resistivity of VAN films. Figure 3.3(c) summarizes the variation of resistivity of $L_{1-x}Z_x$ VAN films at 160 K in the left y-axis as a function of ZnO compositions. And the percolation threshold in conductivity of our VAN films is estimated to be around 70 % of ZnO in molar ratio, above which the resistance grows drastically. The abrupt change of resistivity on conduction threshold has also been reported in other LSMO-based composites previously.[44,178] This behavior can be explained by a classical percolation theory. In this theory, the electrical conductivity σ of a "metal-insulator" composite obeys the power law:

$$\sigma \propto (x - x_c)^p \quad (1)$$

where x represents the volume fraction of conduction phase LSMO ("metal" in this system), and x_c is the critical percolation value and t is a critical exponent with a predicted universal value of 1.9 ± 0.2.[179,180] Figure 3.3(d) shows the fitting curve of Equation (1) to the experiment data. The fitting relationship shows that the conductivity exponent is very close to the predicted value and the calculated conduction threshold value for is 0.48 ± 0.05 of LSMO in volume fraction, which corresponds to 72.5 % ± 2.8 % of ZnO ("insulator" in this system) in molar ratio. The good agreement of this model with the conductivity variation of VAN films suggest that the electron transport in $L_{1-x}Z_x$ composite films is mainly determined by a conducting network mechanism. In this composite system with a sufficient amount of conducting phase (LSMO), conducting channels are formed through a coalescence of LSMO nanodomains, as shown in previous TEM images. On the other hand, as the amount of LSMO decreases below a critical value (percolation threshold value 70 % of ZnO in molar ratio), the conducting channels will vanish and then the composite system exhibits tunneling or insulating behavior. The MIT temperature (T_{MIT}) of $L_{1-x}Z_x$ VAN films is plotted as the right axis, which also displays a systematic change from 284 K to 150 K with the ZnO concentration when x increases from 0 to 50%. It is interesting to note that T_{MIT} of $L_{0.5}Z_{0.5}$ film on buffered Si substrates (~ 150 K) is lower than that (~ 182 K) of the same VAN system on STO single crystal substrates which we demonstrated in a previous report.[14] And the deposition of $L_{0.5}Z_{0.5}$ film on buffered Si substrates also leads to a larger resistivity compared to that on STO substrates. The above performance is possibly due to domain matching of STO and TiN buffer layer on Si substrates increases phase

boundaries and grain boundaries in upper VAN films, which suppressed the ferromagnetic (FM) double-exchange interaction between neighboring FM nanodomains.[40,181]

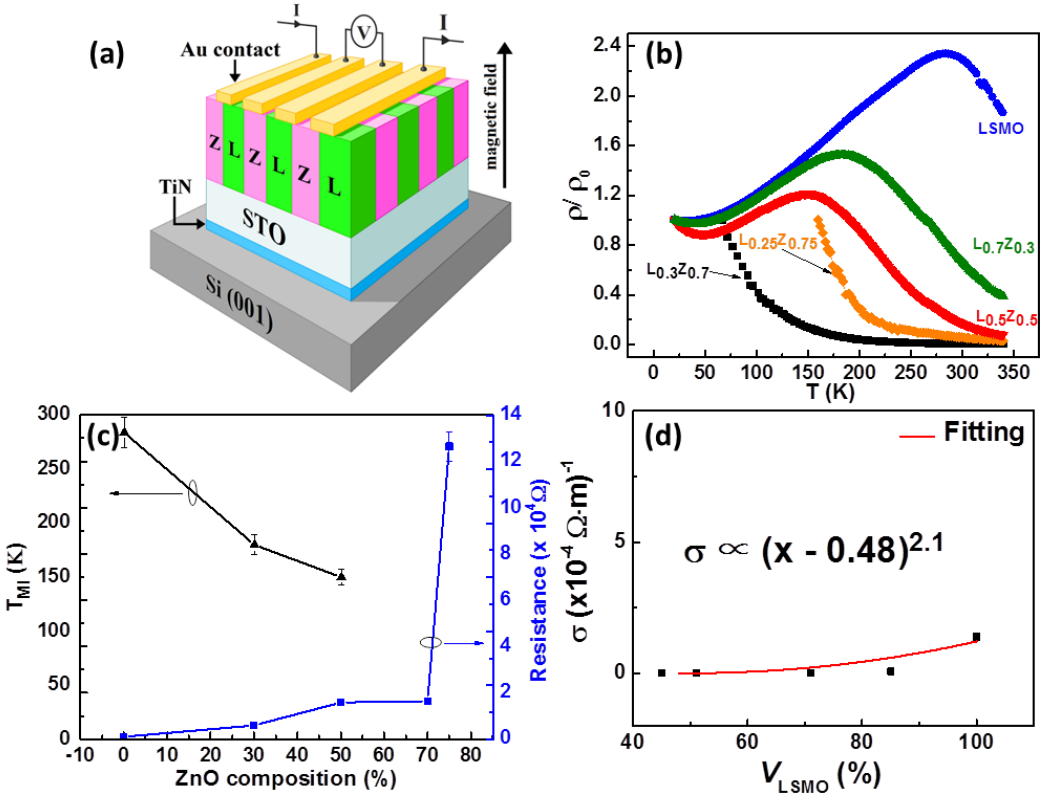

Figure 3.3. (a) A schematic drawing of $L_{1-x}Z_x$/STO/TiN/Si field effect device. (b) Temperature dependence of the normalized zero-field resistivity ρ/ρ_0 of the LSMO:ZnO composite thin films and of pure LSMO films at 0 T, ρ_0 represents resistivity at its lowest measured temperature. (c) The T_{MI} and resistance at 160 K and of VAN films are shown in the left and right axis respectively as a function of ZnO composition at 0 T. (d) Fitting results of conductivity of $L_{1-x}Z_x$ VAN films based on percolation conduction model.

3.6 Conduction mechanism and enhanced LFMR in LSMO:ZnO VAN films

A more detailed study on LFMR of samples with different compositions has been conducted to explore the relationships of LFMR of the whole VAN system as a function of the ZnO phase x. And the resistivity ratio of $L_{1-x}Z_x$ composite films (x=0, 0.3, 0.5, 0.7) was measured at 80 K with the external magnetic field from -1 T to 1 T, as shown in Figure 3.4(a). The LFMR property of $L_{0.25}Z_{0.75}$ is not shown here, whose resistivity is beyond the measurement limit and becomes noisy in the low temperature. It is interesting to note that all resistivity ratio curves show a sharp drop at a low field (0 - 0.5 T) for all compositions followed by a more gradual drop at a higher magnetic field (0.5 T - 1 T). The one with the maximum MR is the composite film with 70 % of ZnO in molar ratio, which corresponds to the critical conduction threshold discussed above. The MR ratios of all samples are plotted in Figure 3.4(b) as a function of temperature. The MR ratio here is defined by $MR= (\rho_0-\rho_H)/\rho_0$, where ρ_0 is the zero-field resistivity and ρ_H is the resistivity under applied magnetic field of 1 T. It is obvious that MR values of all samples increase gradually as the temperature decreases from room temperature to a low temperature range. And the peak MR value for $L_{0.3}Z_{0.7}$ composite thin films on Si is 55 % which is comparable or superior to previous reports on thin films on Si substrates, such as epitaxial LSMO thin films (MR=16 %; T=77 K, H=0.3 T),[176] polycrystalline LSMO films (MR≤20 %; T= 77 K, H=0.4 T),[182] polycrystalline LSMO:Al_2O_3 composite films (MR=15 %; T=86 K, H=0.3 T),[183] and bulk composites.[184,185] It is worthy pointing out that the peak MR value (~ 32 %) of $L_{0.5}Z_{0.5}$ film on buffered Si substrates is close to that (~ 30 %) deposited on STO single crystal substrates,[128] which also implies the success of

the integration of $L_{1-x}Z_x$ film on Si substrates. And the main difference between their LFMR performances is that the $L_{1-x}Z_x$ films on STO reached the peak MR value at a higher temperature, which relates to less spin-fluctuation depression due to decreased structural disorders, as discussed in the previous part. The enhanced and tunable LFMR of LSMO:ZnO composite thin films on Si substrates can be interpreted by spin-polarized tunneling based on magnetic tunnel junction structures. The large MR of LSMO:ZnO VAN films results from several aspects where non-magnetic insulating ZnO phase plays a significantly important role. First, the incorporation of ZnO creates artificial grain and phase boundaries where structural disorders contribute to separating neighboring FM domains, increasing the density of inter-grain spin polarization and promoting spin-polarized tunneling. Second, ZnO phase also serves as an insulating tunneling barrier, creating "ferromagnetic-insulator" (FM-I) state and inducing local spin disorder.[186] It is suggested that the epitaxial growth of LSMO:ZnO composite thin films on Si substrates contributes to increasing the spin-polarized tunneling effect, resulting in better LFMR performance in the VAN films.

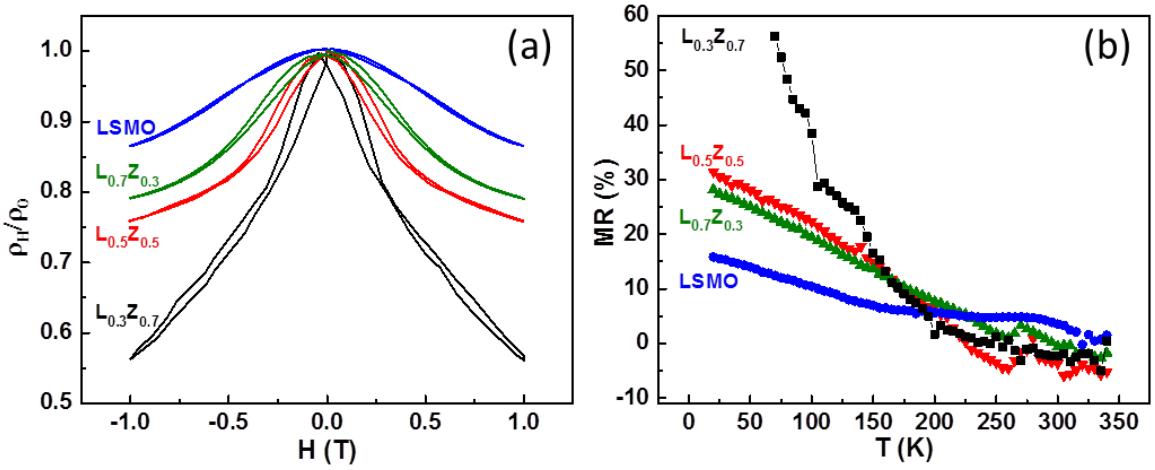

Figure 3.4. (a) Resistivity ratio ρ_H / ρ_0 composite films as a function of magnetic field at 80 K. (b) MR as a function of temperature with different compositions.

3.7 Summary

Highly epitaxial $(LSMO)_{1-x}:(ZnO)_x$ VAN thin films with various compositions were deposited on Si (001) substrates by PLD. The STO and TiN bi-layer buffer has been applied and proved to be effective to grow epitaxial VAN films on Si. The tunable and enhanced LFMR property has been achieved by varying the ZnO concentration in the VAN films. The LFMR value reaches the maximum value of 55 % with 70 % of ZnO in molar ratio at 70 K and 1T. The incorporation of ZnO phases contributes to creating artificial grain and phase boundaries, increasing spin disorder and generating spin-polarized tunneling for improved MR effect. Our results demonstrate that $(LSMO)_{1-x}:(ZnO)_x$ VAN architectures exhibit promising potential for future Si-based LFMR devices.

CHAPTER IV

STRAIN RELAXATION AND ENHANCED PERPENDICULAR MAGNETIC ANISOTROPY IN $BiFeO_3$:$CoFe_2O_4$ VERTICALLY ALIGNED NANOCOMPOSITE THIN FILMS[2]

4.1 Overview

Self-assembled BFO:CFO vertically aligned nanocomposite thin films have been fabricated on STO (001) substrates using pulsed laser deposition. The strain relaxation mechanism between BFO and CFO with a large lattice mismatch has been studied by X-ray diffraction and transmission electron microscopy. The as-prepared nanocomposite films exhibit enhanced perpendicular magnetic anisotropy as the BFO composition increases. Different anisotropy sources have been investigated, suggesting that spin-flop coupling between antiferromagnetic BFO and ferrimagnetic CFO plays a dominate role in enhancing the uniaxial magnetic anisotropy.

[2] This chapter is reprinted with permission from "Strain relaxation and enhanced perpendicular magnetic anisotropy in $BiFeO_3$:$CoFe_2O_4$ vertically aligned nanocomposite thin films" by W. Zhang, et al., Applied Physics Letters, 2014, 104, 062402.

4.2 Introduction

Self-assembled two-phase VAN thin films have recently stimulated significant research interests in understanding their basic growth mechanism and exploring advanced functionalities,[111,114,117,118,122-124,128,143,153,187-190] including effective interfacial coupling,[111] tunable phase and grain boundaries[187] and strain-stabilized structural transition.[114] The strong interaction between two phases plays a critical role in enhancing these physical properties.

Perpendicular magnetic anisotropy (PMA) is one of interesting physical properties demonstrated in some selected epitaxial nanocomposite systems, such as BFO:CFO,[191] BTO:CFO[54] and PTO:CFO[192] films. For high-density magnetic memory device applications, PMA is highly desirable owing to its large thermal stability and scaling capability.[26,193] However PMA in heteroepitaxial VAN systems is very sensitive to the lattice parameters of underlying substrates,[191] film composition[194] and thickness,[195] and the origin of the magnetic anisotropy in the CFO:BFO system is not yet clear. It was suggested that the large lattice mismatch (-5.79 %) between the two phases could yield a large vertical compressive strain in CFO,[118] inducing a dominant magnetoelastic stress anisotropy.[194] However, misfit dislocations are usually revealed across their interfaces by TEM study,[196] relaxing the mismatch strain and limiting the stress anisotropy effect. On the other hand, shape anisotropy was thought to dominate in BFO:CFO system through a morphology-controlled study of magnetic anisotropy.[191] Moreover, the interfacial exchange coupling between the ferromagnetic (or ferrimagnetic) and antiferromagnetic phases could also provide important uniaxial anisotropy

contributions.[197] In this letter, the epitaxial BFO:CFO films in VAN form have been fabricated to gain more insights into the origin of enhanced PMA effect. The stress evolution and relaxation have been investigated through structural characterization of BFO:CFO films with two different molar ratios of 33:67 and 67:33. Different sources of magnetic anisotropy have been explored and compared.

4.3 Experimental method

The BFO:CFO VAN films with molar ratios of 33:67 and 67:33 were deposited on single-crystal STO (001) substrates by pulsed laser deposition using a KrF excimer laser operated at 10 Hz with a fluence of 3 J cm^{-2}. A substrate temperature of 700 ℃ and a dynamic chamber pressure of 100 mTorr oxygen were maintained during deposition . After deposition, the composite thin films were cooled in 200 Torr oxygen at a cooling rate of 5 ℃/min. The chemical composition and microstructure of as-deposited films were investigated using XRD (PANalytical Empyrean), SEM (JEOL JSM-7500F) and STEM/TEM (FEI Tecnai G2 F20) operated at 200 kV. The magnetic property measurements were carried out using a VSM option in a commercial PPMS (Model 6000, Quantum Design).

4.4 Thin film growth and microstructure of BFO:CFO VAN films

The high quality growth of $(BFO)_x$:$(CFO)_{1-x}$ (B_xC_{1-x}) VAN films was first demonstrated in the θ-2θ XRD scans (Figure 4.1(a)). The local XRD scans of the VAN films around STO (002) are shown in Figure 4.1(b). It is interesting to notice that there is a systematic peak shift for both BFO (002) and CFO (004) as the film composition varies. The film thickness is ~700 nm and the substrate-induced strain is expected to be

fully relaxed in this case.[195] Thus the vertical strain control is responsible for the systematic peak shift, similar to several other VAN systems.[124,128] The out-of-plane compressive strain (ε_{001}) on CFO in $B_{0.33}C_{0.67}$ and $B_{0.67}C_{0.33}$ is determined to be ~ -0.29 % and ~ -0.31 % based on the local XRD scans. These results suggest significant strain relaxation across their vertical interfaces, compared to their calculated lattice mismatch (-5.79 %).[118] The Φ-scans of the BFO (202), CFO (404) and STO (202) in Figure 4.1(c) confirm the direct cube-on-cube epitaxial growth of these two phases on STO (001) substrates without any in-plane rotation.

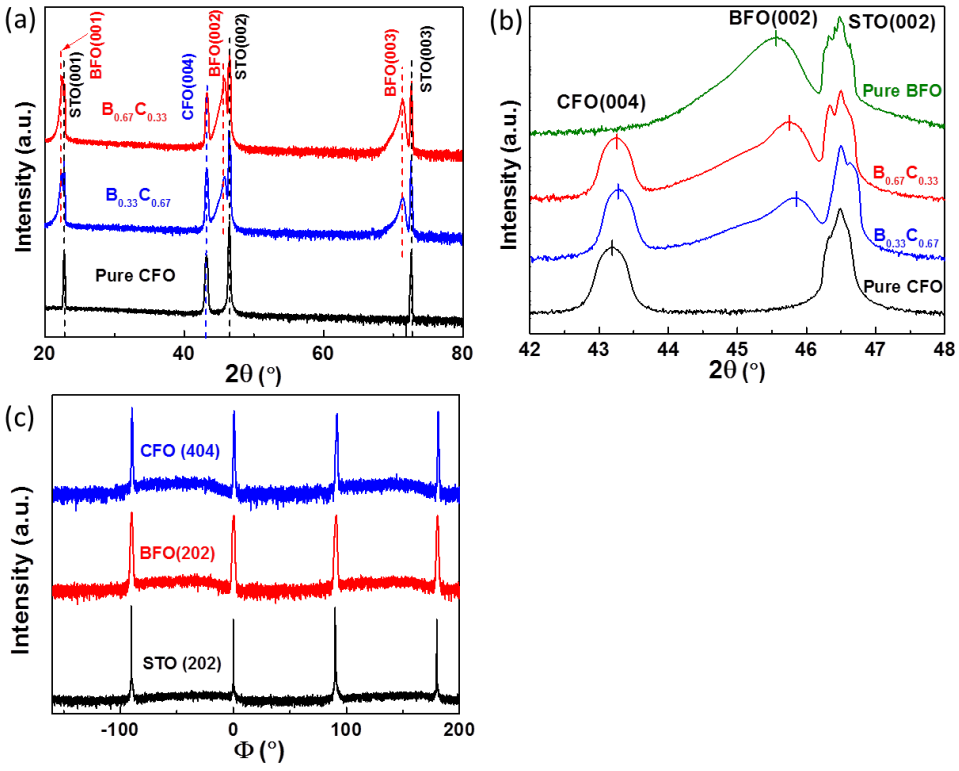

Figure 4.1. (a) The XRD θ-2θ full scans and (b) local scans near STO (002) of BFO:CFO VAN films and pure films. (c) Phi scans of STO (202), BFO (202) and CFO (404) in BFO:CFO VAN films.

The top view backscattered electron (BSE) image of pure CFO film reveals a smooth surface with various grain boundaries between CFO grains (Figure 4.2(a)), which is consistent with the observation from the corresponding secondary electron (SE) image as an inset in the top right. As the BFO is incorporated into the VAN films with a molar ratio of 33 %, uniformly distributed nanopillars are formed in the matrix as shown in Figure 4.2(b). The corresponding BSE image suggests that the observed nanopillars are the BFO phase, since the heavier element of Bi ($Z_{Bi} = 83$) in BFO could generate a stronger backscattering intensity than that of Fe ($Z_{Fe} = 26$) or Co ($Z_{Co} = 27$) in CFO. The insets in the bottom right of Figure 4.2(b) and Fig. 4.2(c) are the corresponding BSE images processed for volume ratio calculations. The volume ratios of BFO were estimated to be 58.3 % for $B_{0.67}C_{0.33}$ and 22.9 % for $B_{0.33}C_{0.67}$ films, which is consistent the original target composition. It is interesting to note that the observed microstructure is different compared to those previously reported ones, where CFO nanopillars were embedded in the BFO matrix on STO (001) substrates.[194,198] The resulted microstructures are closely related to the interfacial energy between these two phases and the underlying substrates, and growth kinetics under different growth conditions.[115] Further discussions are presented later along with TEM results. As the BFO molar ratio increases up to 67 %, it remains the same form of nanopillars with an obvious increase in density and average diameter (Figure 4.2(c)), suggesting an independent relationship of film morphology and its composition. The images of the pure BFO film in Figure 4.2(d) present a quite smooth surface morphology with few small voids, which were not seen in the composite samples.

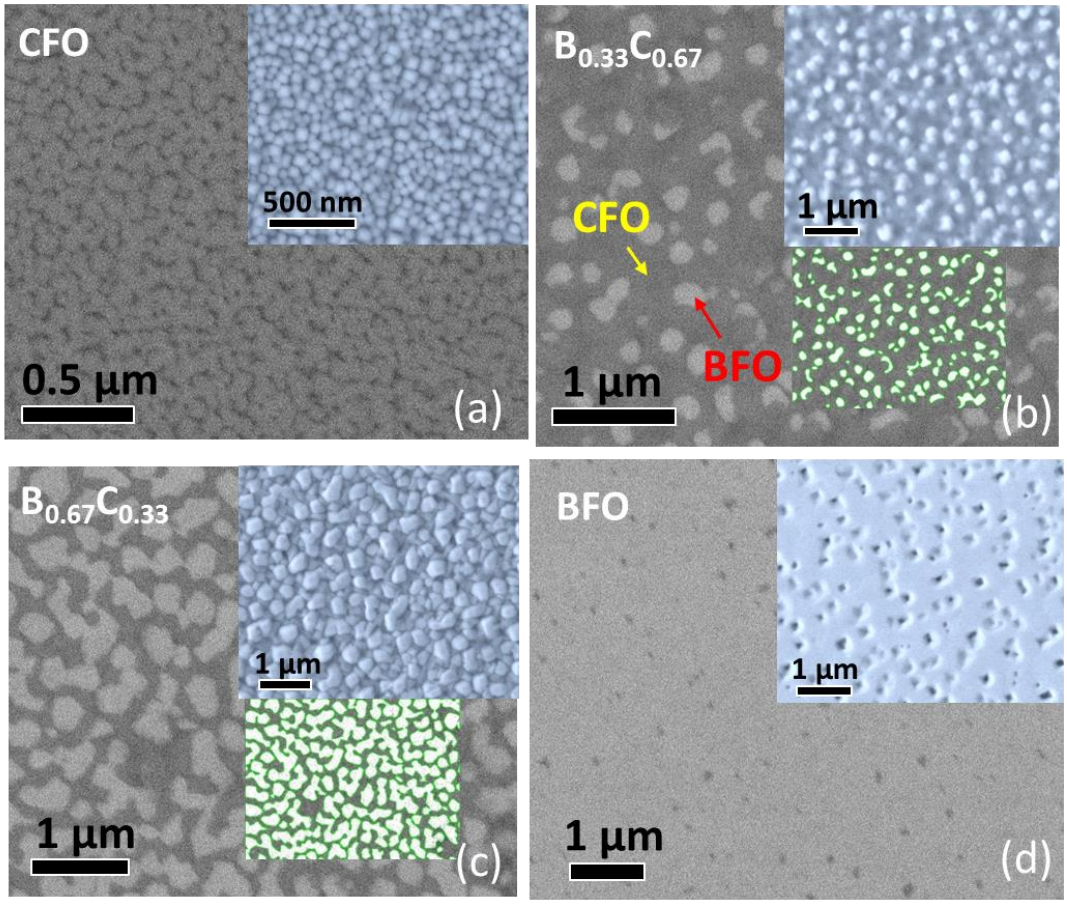

Figure 4.2. The top view backscattered electron (BSE) images of (a) CFO, (b) $B_{0.33}C_{0.67}$, (c) $B_{0.67}C_{0.33}$ and (d) BFO films. Insets in the top right are their corresponding secondary electron images. Insets in the bottom right of Figures 4.2(c) and 4.2(d) are corresponding processed images for volume ratio calculations.

Figure 4.3(a) shows the cross-sectional STEM image of $B_{0.67}C_{0.33}$ film, which confirms the vertically ordered growth of BFO nanopillars in the CFO matrix. It is clear that BFO shows a much brighter contrast than that of CFO, since Z_{Bi} is much higher than Z_{Co} and Z_{Fe}. In addition, the distinguished diffraction dots in the corresponding SAED pattern (inset of Fig. 4.3(a)) imply the epitaxial growth of the nanocomposite film. Figure 4.3(b) presents a HRTEM image at the triple junction where the two phases meet

the substrate. Moire patterns can be clearly seen from the initial growth of BFO, while CFO achieves a high quality epitaxial growth. The observed TEM results confirmed findings from the XRD data that suggests that CFO achieves a better epitaxial growth. This could partially explain the formation of the observed reversed VAN structures in this study. Although BFO (001) has a better wettability with STO (001) substrates, the intrinsic BFO lattice and grain reorientation partially disturbed the initial nucleation and therefore limited the lateral growth of BFO. In contrast, the highly ordered CFO phase could take the role of connecting each other during growth, surrounding the BFO nanopillars and forming the planar matrix. There is some variation in the morphology as a function of the film thickness and laser energy density which is still under investigation. The above results imply that the microstructure of VAN films is closely related to their growth kinetics and could be directly controlled by varying growth parameters.

In order to reveal the strain relaxation mechanism of BFO and CFO, the HRTEM image of the vertical heterointerfaces between the two phases is shown in Figure 4.3(c). The ordering observed in BFO Moiré fringes is represented by the alternative arrangement of dark and bright contrast regions in BFO, as noted using pink and blue dots, respectively. The corresponding SAED pattern obtained from BFO nanocolumns in Figure 4.3(d) provides more evidence for the existence of the ordering. The obvious double diffraction characteristics, i.e., a set of secondary diffractions, are found around the primary diffraction dots, confirming the orderings of BFO columns as shown in the enlarged area in Figure 4.3(e). These secondary diffractions are associated with the

periodic contrast in the BFO nanocolumns in Figure 4.3(c), which gives the calculated d-spacing of 4.53 nm and 4.71 nm, respectively, in two orthogonal-like directions. This agrees well with measured Moire fringe spacing of a (4.45 nm) and b (4.65 nm) in Figure 4.3(c). Figure 4.3(f) shows the local diffraction of CFO phases, demonstrating its high epitaxial quality.

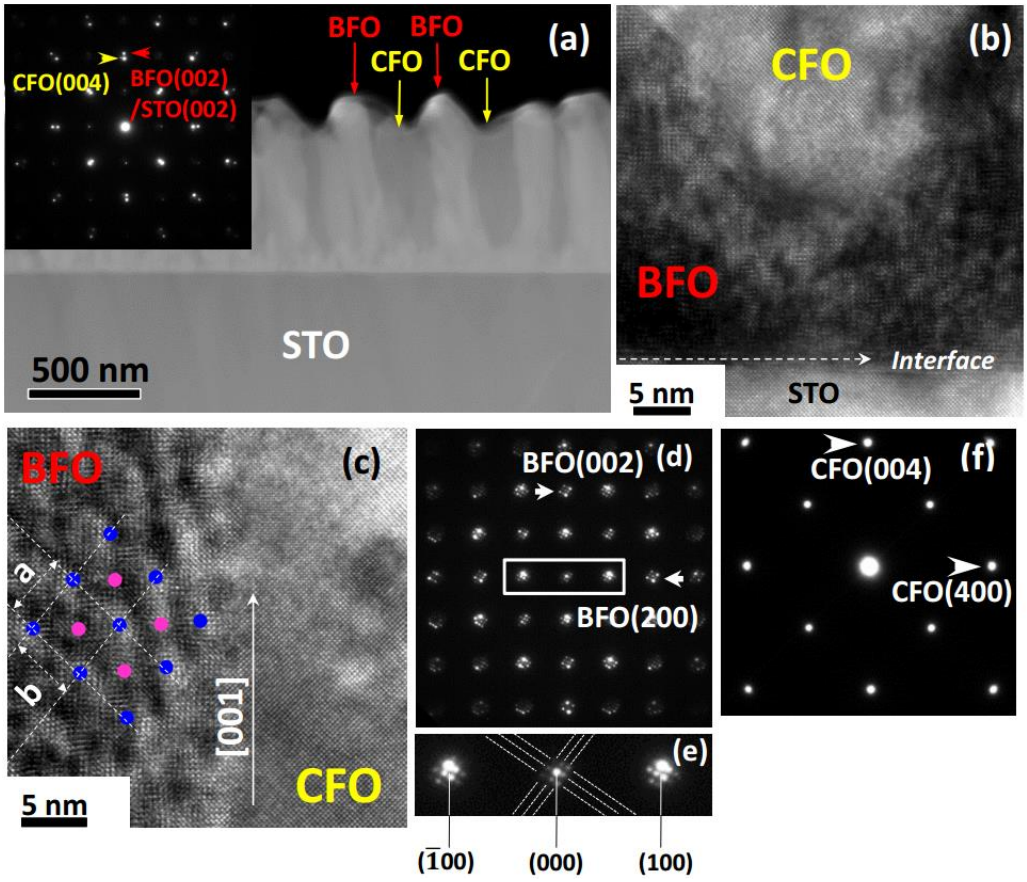

Figure 4.3. (a) Cross-sectional STEM images of $B_{0.33}C_{0.67}$ VAN film. Inset shows the corresponding SAED pattern. (b) HRTEM image of the triple junction including BFO, CFO and STO substrate. (c) HRTEM image of vertical heterointerface of BFO and CFO. (d) The corresponding SAED pattern of BFO nanocolumns showing double diffraction characteristic. (e) Enlargement of part of BFO SAED pattern in (d). (f) SAED pattern of CFO phase.

4.5 Enhanced perpendicular magnetic anisotropy

Figure 4.4(a)-(c) show the in-plane and out-of-plane M(H) loops of $(BFO)_x$:$(CFO)_{1-x}$ films measured at 300 K. The magnetization values were normalized to the volume fraction of CFO after subtracting the diamagnetic signals from STO substrates. The ratios of remanence to saturation magnetization (M_r/M_s) and corresponding coercivity values are summarized in Table 4.1, which are used to characterize their magnetic anisotropy. First, for the pure CFO film, the easy axis is not well defined, i.e., both the in-plane and out-of-plane M_r/M_s ratios ($(M_r/M_s)_{\parallel}$ and $(M_r/M_s)_{\perp}$) are smaller than 50%. Second, as soon as BFO is coupled with CFO in VAN films, a strong uniaxial magnetic anisotropy is observed with a larger $(M_r/M_s)_{\perp}$ value of 67.6 % in $B_{0.33}C_{0.67}$ and 78.6 % in $B_{0.67}C_{0.33}$ VAN films. This perpendicular anisotropy is also confirmed by the difference in their coercive fields, i.e., out-of-plane coercive field ($H_{c\perp}$) becomes almost twice or more than the in-plane value ($H_{c\parallel}$).

Table 4.1. Magnetic properties (H_c and M_r/M_s in out-of-plane and in-plane directions) and anisotropy energies of pure CFO, $B_{0.33}C_{0.67}$ and $B_{0.67}C_{0.33}$ films

Sample #	$H_{c\perp}$ (kOe)	$H_{c\parallel}$ (kOe)	$(M_r/M_s)_{\perp}$ (%)	$(M_r/M_s)_{\parallel}$ (%)	K_{me} (erg/cm^3)	K_s (erg/cm^3)
CFO	1.10	1.92	36.7	19.3	1.51×10^6	-1.67×10^6
$B_{0.33}C_{0.67}$	2.50	1.33	67.6	12.4	2.15×10^6	-1.57×10^6
$B_{0.67}C_{0.33}$	2.78	1.52	78.6	15.2	2.30×10^6	-2.21×10^6

4.6 Investigation of the origin of enhanced PMA effect

To elucidate the origin(s) of the enhanced PMA effect, several important anisotropy sources were examined, including magnetocrystalline anisotropy, shape anisotropy, stress anisotropy and interface exchange anisotropy. First, for the epitaxial CFO film oriented along its [001] direction, the magnetocrystalline anisotropy between its in-plane and out-of-plane directions is not expected. As for the shape anisotropy, its anisotropy energy (K_s) is calculated based on a two-dimensional model of $K_s = -2\pi M_s^2$.[199] Since the CFO phase is the planar matrix in the VAN film, its shape anisotropy contributes to the in-plane anisotropy. It is noted that the CFO matrix is actually a planar matrix with perpendicular columnar pores, which could decrease the overall in-plane anisotropy. With the pores in the CFO matrix, there is around 10 % - 15 % less of the original K_s. For simplicity, here we use K_s of a continuous and homogenous CFO matrix in the following calculations. The calculated anisotropy energy values are listed in Table I, where the negative and positive signs correspond to in-plane and out-of-plane anisotropy. The third anisotropy energy source stems from the stress anisotropy, which results from the magnetostriction effect of CFO. The magnetoelastic energy (K_{me}) is given by the equation of $K_{me} = -\frac{3}{2} * \lambda_{001} * \mathrm{Y} * \varepsilon_{001}$, where λ_{001} is the magnetostrictive coefficient of CFO (~ -350×10^{-6}), and Y is the Young's modulus (~141.6 GPa).[54] The calculated K_{me} of pure CFO film is 1.51×10^6 erg/cm^3, which contributes to the out-of-plane anisotropy. Thus the small overall anisotropy energy of pure CFO film (-0.16×10^6 erg/cm^3) explains the fact that its magnetic anisotropy is not well defined. Similar calculations have also been conducted for the $B_{0.33}C_{0.67}$ and

$B_{0.67}C_{0.33}$ films, which results in a total anisotropy energy of 0.58×10^6 erg/cm^3 and 0.09×10^6 erg/cm^3, $B_{0.33}C_{0.67}$ and $B_{0.67}C_{0.33}$, respectively. The anisotropy fields are estimated for the as-prepared films according to $H_s = 2K/M_s$, [54] which yields a value of 2.32 kOe for $B_{0.33}C_{0.67}$ and 0.303 kOe for $B_{0.67}C_{0.33}$, respectively. These values, however, are much smaller than the experimentally observed saturation field (~20 kOe) in this work, which is determined by extrapolating the linear magnetization regime along its in-plane direction. This suggests that the strong PMA effect in BFO:CFO film may arise from other important sources, e.g., interfacial exchange energy between ferrimagnetic CFO and antiferromagnetic BFO could be another important source.

It is well known that the presence of AFM-FM interfaces could generate strong coupling effects, resulting in intriguing phenomena. Exchange bias effect is expected if the uncompensated spins in AFM phase are pinned at the AFM-FM interfaces.[24] However, if the spins in AFM were fully compensated, or if the uncompensated spins were rotatable with FM spins, the exchange bias vanishes. No observable exchange bias is obtained in the field cooling measurement of BFO:CFO films (Figure 4.4(d)), confirming the existence of rotatable AFM spins in BFO reported by others.[198,200,201] Schulthess *et al*. proposed that an effective AFM-FM interfacial coupling, spin-flop coupling, induces a uniaxial anisotropy instead of exchange bias effect using a microscopic Heisenberg model.[56] For this coupling, part of the AFM spins around the FM-AFM interfaces are rotated with FM spins during field reversal, forming a domain wall in AFM and introducing exchange anisotropy energy. The intimately coupled antiferromagnetic and ferromagnetic orders in multiferroic BFO induce a strong ME

coupling in BFO with an inferred ME energy density of ~ 3×10^8 erg/cm^3.[6,202] Since partial AFM spins in BFO are rotated with FM spins in CFO as external magnetic field is applied, an extra anisotropy field is needed to accommodate the ME energy barrier induced by the intrinsic coupling between AFM spins and electrical polarization in BFO. For the observed saturation field of 20 kOe and an average M_s value of 500 emu/cm^3, the interfacial AFM spins for the spin-flop coupling accounts for ~1.67 % of all the AFM spins in BFO. Similar cases of spin-dependent coupling and interfacial domain formation have also been reported in other BFO-based systems such as BFO/LSMO[203] and BFO/CoFe bilayers.[204] Based on the above discussions, the mechanism of spin-flop coupling is considered to be the major source responsible for the enhanced PMA effect in the BFO:CFO VAN films.

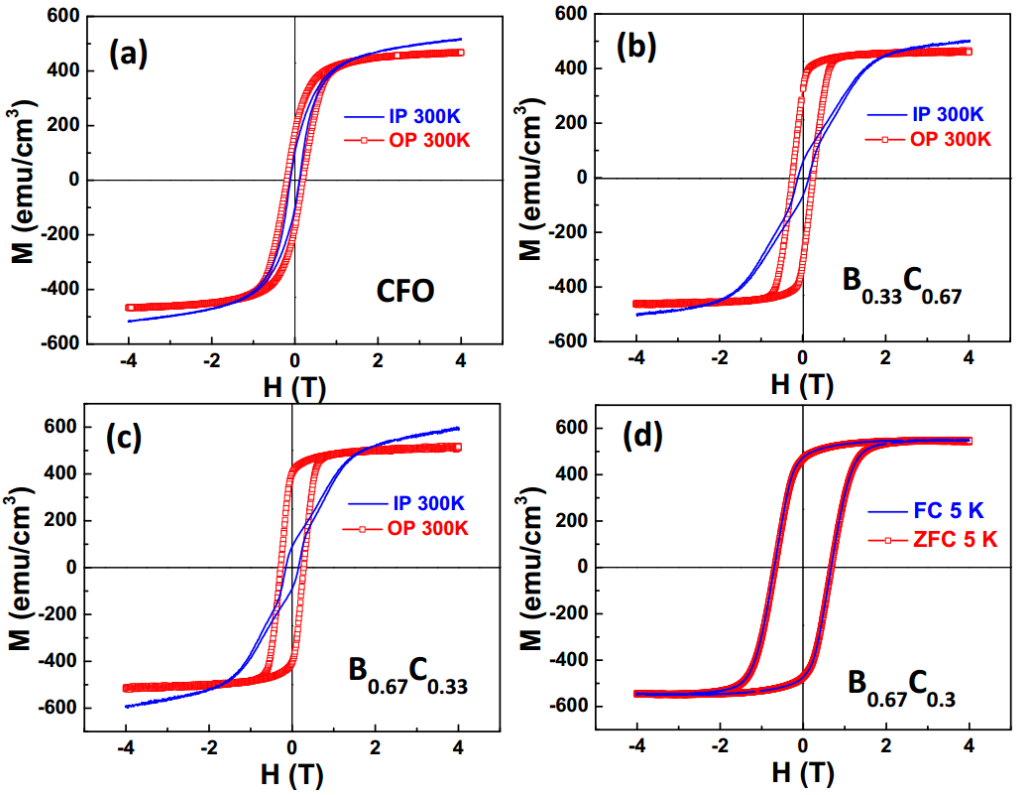

Figure 4.4. In-plane (IP, blue lines) and out-of-plane (OP, red squares) M(H) loops of (a) CFO, (b) $B_{0.33}C_{0.67}$ and (c) $B_{0.67}C_{0.33}$ VAN films measured at 300 K. (d) The OP M(H) loops of $B_{0.67}C_{0.33}$ film after zero field cooling (ZFC, red squares) and field cooling (FC, blue lines) from 300 K to 5 K. The cooing field for FC is 1 T.

4.7 Summary

Vertically aligned BFO:CFO nanocomposite films have been grown by PLD. XRD and TEM studies indicate that strain relaxation between these two phases stems from that BFO lattices reorientation and interfacial dislocations. Enhanced PMA effect is observed as BFO is incorporated in the VAN films. The vertical aligned structure favors the spin-flop coupling between BFO and CFO, which is identified as the major contributor for the enhanced PMA effect in VAN films.

CHAPTER V

STRONG PERPENDICULAR EXCHANGE BIAS IN EPITAXIAL $La_{0.7}Sr_{0.3}MnO_3$:$BiFeO_3$ NANOCOMPOSITE FILMS THROUGH VERTICAL INTERFACIAL COUPLING[3]

5.1 Overview

EB effect with perpendicular anisotropy is of great interest for potential applications such as read heads in magnetic storage devices with high thermal stability and reduced dimension. Here we report a novel approach to achieving perpendicular exchange bias by orienting the ferromagnetic/antiferromagnetic coupling in the vertical geometry through a unique VAN design. Our results demonstrate robust perpendicular exchange bias phenomena in micrometer-thick films employing a prototype material system of AFM BFO and FM LSMO. The unique response of exchange bias to perpendicular magnetic field reveals the existence of exchange coupling along their vertical heterointerfaces, which exhibits strong dependence on their strain states. This VAN approach enables a large selection of material systems for achieving perpendicular exchange bias, which could lead to advanced spintronic devices.

[3] This chapter is reprinted with permission from "Strong perpendicular exchange bias in epitaxial $La_{0.7}Sr_{0.3}MnO_3$:$BiFeO_3$ nanocomposite films through vertical interfacial coupling" by W. Zhang, et al., Nanoscale, **2015**, 7, 13808-13815.

5.2 Introduction

Interfaces of epitaxial oxide heterostructures have exhibited novel physical phenomena because of the strong electron correlations and symmetry constrains.[118,169,205] Representative functionalities include two-dimensional electron gas,[7] interface superconductivity,[206] quantum Hall effect,[207] magnetotransport and magnetoelectrics.[115,153,208] Arising from the FM-AFM interfacial coupling,[209] EB is well exploited in magnetic memory and hard disk drives, and has been suggested to be critical elements for next-generation high-density non-volatile memory devices.[60,210,211] With recent advances in the atomic-scale synthesis techniques and characterization methods, the dimensions of EB research are explored in new types of heterostructures, where a ferromagnet is layered with non-magnetic MgO,[61] paramagnetic $LaNiO_3$,[69] spin glass of CuMn,[68] as well as multiferroic systems.[27,72]

Most EB effect occurs in layered structures where the exchange coupling pins the magnetization of FM layers in the in-plane direction.[27,61,68,69,72,211] However, perpendicular anisotropy is more desirable for many applications requiring high thermal stability at reduced dimension.[26,46,74] Commonly reported material systems with perpendicular anisotropy are based on layers of noble metals with high spin-orbital interaction, such as Co/(Pd,Pt) multilayers,[75] $DyCo_5$-[74] and CoFeB-based spin valves.[26] Although there has been some progress in obtaining PEB by constructing multilayers of these metals or alloys, the material selection is still very limited. In addition, the limited thickness range of the coupled ferromagnetic layer is another drawback which hinders the practical applications requiring high sensitivity and large storage density, as the

strength of EB is inversely proportional to the ferromagnetic layer thickness (t_{FM}) in the layered geometry.[60]

In this work, we demonstrate a pronounced PEB effect through vertical interfacial coupling in a prototype $La_{0.7}Sr_{0.3}MnO_3$:$BiFeO_3$ (LSMO:BFO) system with a unique VAN structure. The reasons of selecting LSMO and BFO for the VAN growth include several aspects. (1) LSMO and BFO have a good in-plane lattice matching (a_{LSMO} = 3.870 Å; a_{BFO} = 3.962 Å) with the underlying $SrTiO_3$ substrate (a_{STO} = 3.905 Å), and thus simultaneous epitaxial growth of both phases is possible; (2) The growth kinetics of these two phases are similar and high crystallinity could be obtained for both phases at 700 ℃; (3) Both LSMO and BFO are thermodynamically stable at the selected growth temperature and thus the intermixing between the two phases could be minimized. Different from the chemically compatible $BiFeO_3$-Fe_3O_4 nanocomposite films with metastable morphologies,[201] the vertical, clean and strained FM-AFM heterointerfaces in this work have enabled the exchange coupling OP, giving rise to a very systematic vertical strain tuning and tunable exchange bias effects. With detailed strain analysis and interface characterization, a possible mechanism driven by the strain-controlled spin reorientation is proposed to explain the observed PEB effects with a robust perpendicular anisotropy maintained up to the micrometer thickness range.

5.3 Thin film growth and vertical strain tuning of LSMO:BFO VAN films

Figure 5.1(a) shows the full θ-2θ XRD scan of a representative $LSMO_{0.5}$:$BFO_{0.5}$ ($L_{0.5}B_{0.5}$) VAN film compared with the pure LSMO film, indicating high epitaxial growth of both pure and nanocomposite films. The local (002) XRD patterns in Figure

5.1(b) compares the results of the $LSMO_{1-x}$:BFO_x ($L_{1-x}B_x$) (x = 0, 0.2, 0.25, 0.5 and 0.67) VAN films. As x increases, both LSMO (002) and BFO (002) peaks shift to lower angles, which suggests a strong and coherent strain tuning between these two phases in the vertical direction. Figure 5.1(c) presents the variation of out-of-plane lattice parameters of LSMO (c_{LSMO}) and BFO (c_{BFO}) versus the film composition. A systematic vertical strain tuning has been obtained in the $L_{1-x}B_x$ VAN films by adjusting the film composition (Figure 5.2). The vertical strain states of LSMO have been switched from *compressive* to *tensile* through the vertical interface coupling with the BFO, while a *converse* strain state transition has been observed in BFO. The in-plane relationships between the VAN film and the underlying substrate were investigated by the phi scan (Figure 5.1(d)), which indicates cube-on-cube growth of both phases on STO.

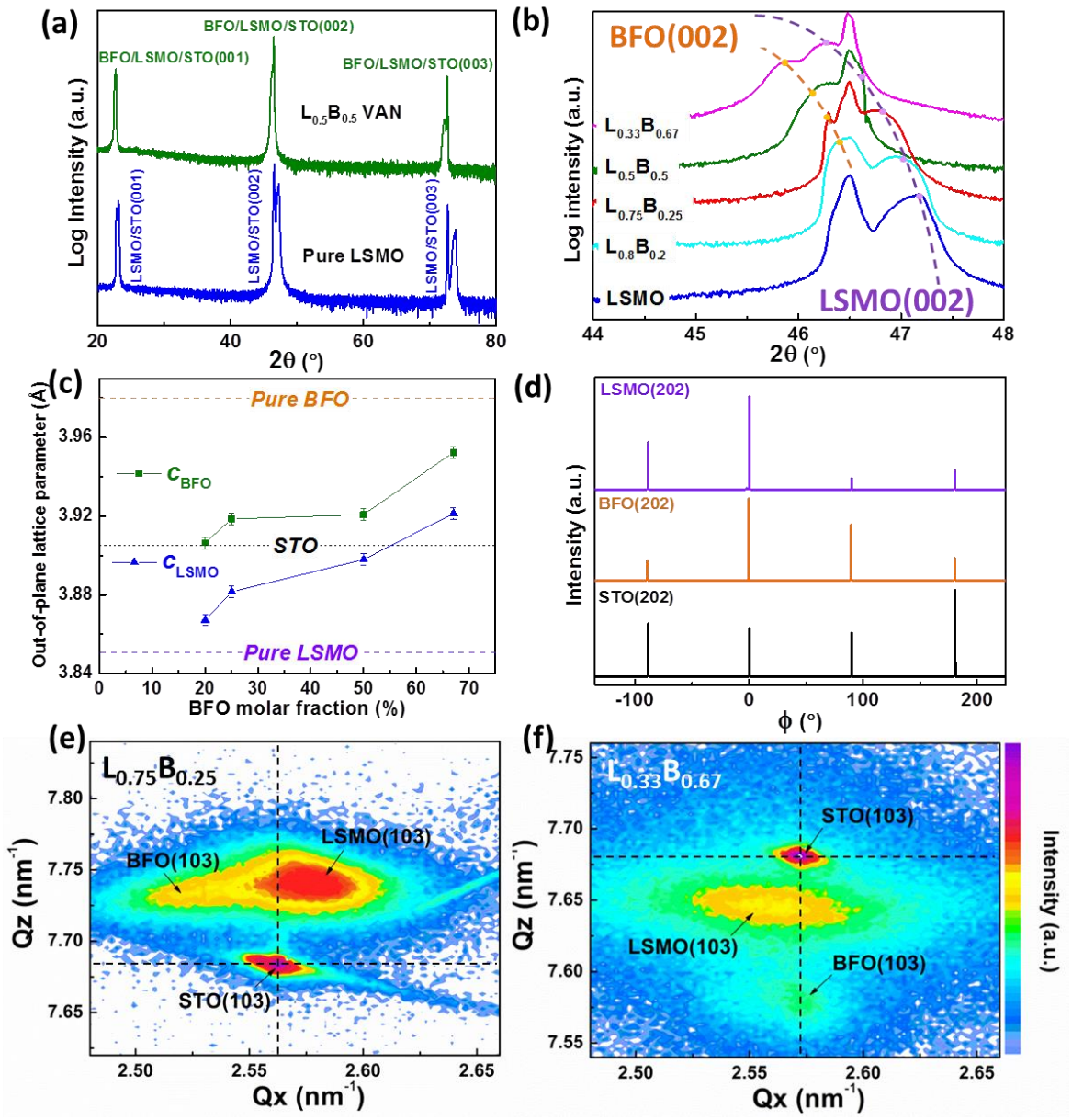

Figure 5.1 (a) θ-2θ XRD scans of pure LSMO and $L_{0.5}B_{0.5}$ VAN films. (b) Local (002) XRD scans of $L_{1-x}B_x$ (x = 0, 0.2, 0.25, 0.5, 0.67) VAN films. (c) The systematic tuning of out-of-plane lattice parameter of BFO and LSMO by BFO molar fraction. (d) ϕ scan results of $L_{0.5}B_{0.5}$ VAN film. Reciprocal space maps near STO (103) for (e) $L_{0.75}B_{0.25}$ and (f) $L_{0.33}B_{0.67}$ films.

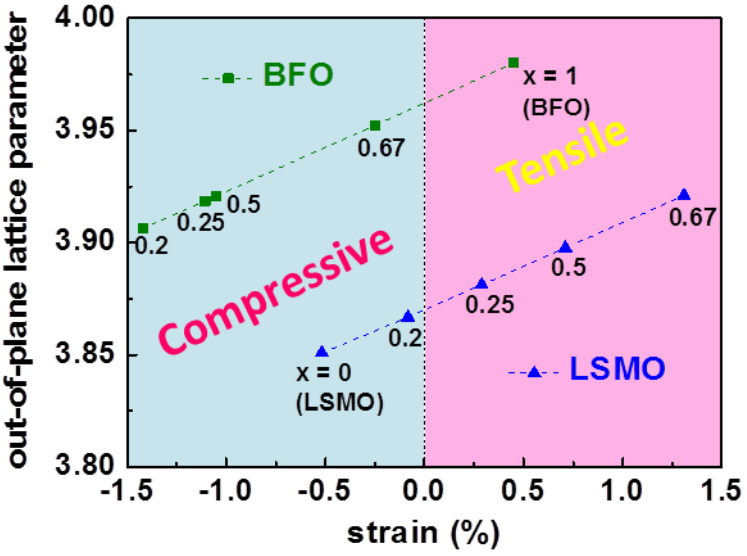

Figure 5.2. Out-of-plane lattice parameter versus strain for $L_{1-x}B_x$ films.

The vertical strain transition is further evidenced by the clear shift of both LSMO and BFO peak positions in reciprocal space maps (RSM) of the $L_{0.75}B_{0.25}$ film to the $L_{0.33}B_{0.67}$ film (Figures 5.1(e) and 5.1(f)). The in-plane strain for both films are also investigated, which suggests large in-plane strain (~1.2-1.4 %) in both BFO and LSMO for $L_{0.33}B_{0.67}$ films compared to their much relaxed strain (~0.2-0.4 %) for $L_{0.75}B_{0.25}$ films. The above results demonstrate effective strain tuning in LSMO:BFO films through adjusting the film composition, which have profound effects on their microstructure and physical properties.

5.4 Microstructure and vertical interface coupling of LSMO:BFO VAN films

Microstructure analysis of $L_{1-x}B_x$ VAN films was conducted using transmission electron microscopy (TEM) and aberration-corrected scanning transmission electron

microscopy (STEM) (Figure 5.3), showing columnar structures with vertical phase boundaries. Figure 5.3(a) shows the TEM images of a 1-μm-thick $L_{0.75}B_{0.25}$ VAN film, which shows the BFO nanopillar is embedded in the LSMO matrix. The corresponding top view AFM image in the inset of Figure 5.3(a) confirms this interesting morphology of self-assembled nanopillars in a planar matrix.

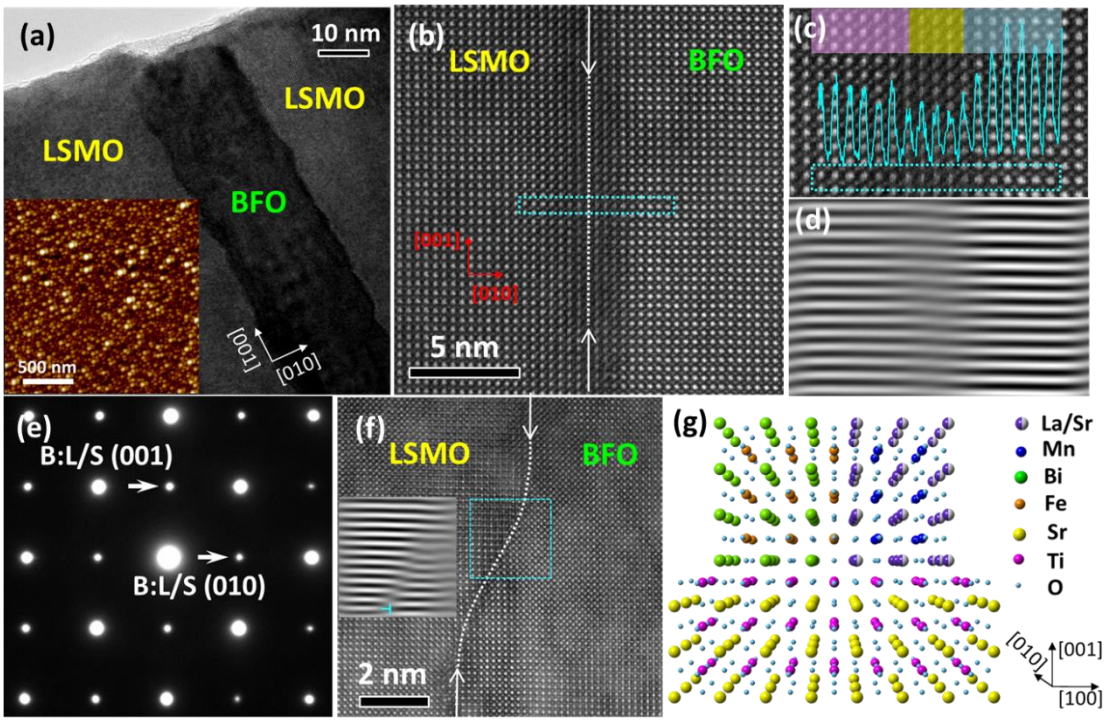

Figure 5.3. (a) Cross-sectional TEM image of the $L_{0.75}B_{0.25}$ VAN film showing a BFO pillar embedded in the LSMO matrix. Inset shows the corresponding top-view AFM image. (b) High-resolution STEM image of the vertical heterointerface between LSMO and BFO. (c) Enlarged view of the atomic lattice across the heterointerface. The intensity line profile is inserted along the marked rectangular region. The interfacial region (yellow) shows a weaker intensity than either LSMO (pink) or BFO (aqua) possibly due to a strain confinement effect. (d) FFT image of (c) showing the coherent one-to-one lattice matching without any dislocations. (e) Corresponding SAED pattern showing the high epitaxy of the $L_{0.75}B_{0.25}$ film. (f) High-resolution STEM image of the heterointerface in the $L_{0.33}B_{067}$ film, showing increased interface roughness. The inset shows the FFT image of the marked region identifying dislocations. (g) Crystallographic model of the $L_{1-x}B_x$ VAN films.

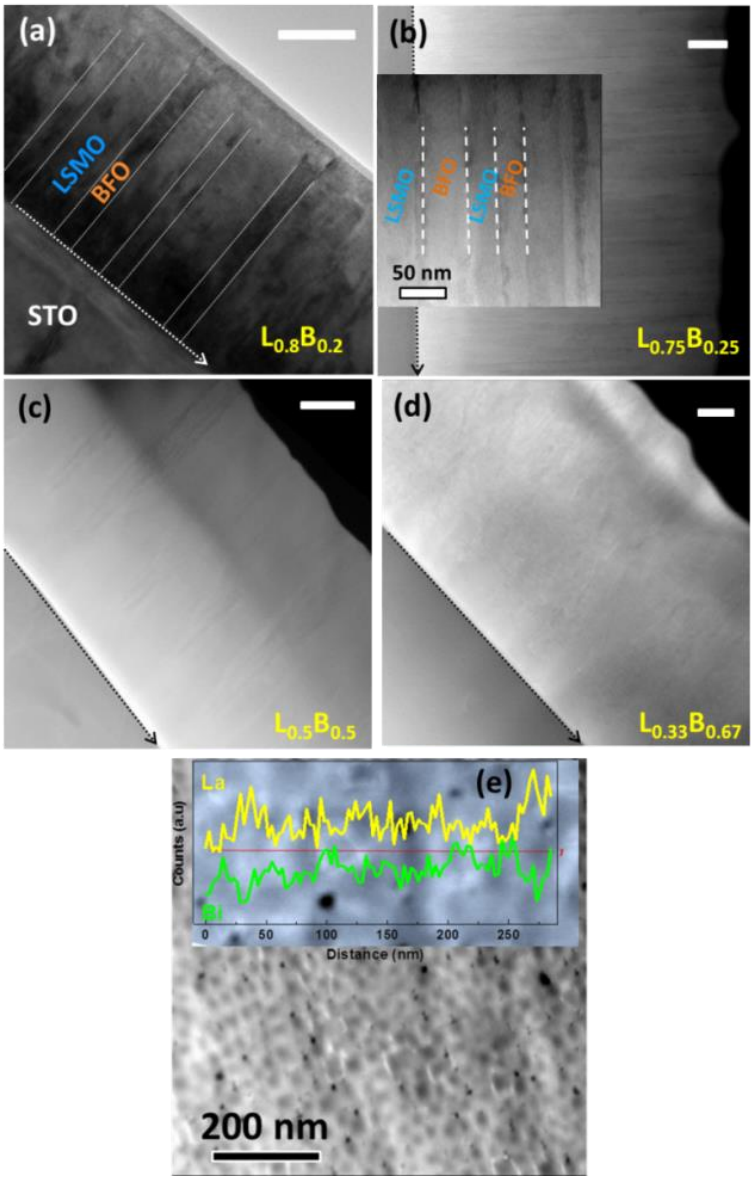

Figure 5.4. (a)-(d) Cross-sectional (S)TEM images of $L_{1-x}B_x$ (x=0.2, 0.25,0.5,0.67) films. Scale bars are 100 nm. Inset in Figure 5.4(b) shows enlarged VAN structure. (e) Plan view STEM image of $L_{0.75}B_{0.25}$ VAN films showing a clear pillar-in-matrix morphology. The inset shows the EDS line results across a pillar-matrix region.

Further composition analysis has been conducted by energy-dispersive X-ray spectroscopy in the STEM mode, which shows a clear phase separation between LSMO

and BFO (Figure 5.4(e)). Figure 5.3(b) shows a straight and ultraclean heterointerface between LSMO and BFO along the [001] direction. We further examined the phase distribution across this heterointerface using the intensity line profile (Figure 5.3(c)), which provides direct interpretation of different phases in the high angle annular dark field (HAADF) imaging mode. A clear phase separation was observed from their different contrasts, and the dark region between the two phases is attributed to a strain-confinement effect due to the lattice mismatch between LSMO and BFO. Figure 5.3(d) shows the fast Fourier transform (FFT) image of the area in Fig. 2c, indicating an exact one-to-one lattice matching between LSMO and BFO. The selected area electron diffraction (SAED) pattern of the $L_{0.75}B_{0.25}$ film in Figure 5.3(e) exhibits very high epitaxial quality of the film. When the BFO composition (x) changes from 0 to 0.67, vertical phase interfaces were maintained with more dislocations observed (See Figures 5.4(a)-(d)). Figure 5.3(f) shows the heterointerface in $L_{0.33}B_{0.67}$ films. The curved interface and the dislocation identified in the inset FFT image indicate increased interface roughness as x increases. The schematic atomic model in Figure 5.3(g) illustrates the crystallographic relationships of the $L_{1-x}B_x$ films on STO substrates. The one-to-one lattice matching is crucial for generating an effective vertical strain coupling between LSMO and BFO, as well as the magnetic exchange coupling and PEB effect demonstrated in the following sections.

ZFC and FC measurements have been carried out for as-prepared LSMO:BFO films using vibrating sample magnetometer (VSM). Fig. 3 shows the magnetization hysteresis curves of $L_{0.75}B_{0.25}$ and $L_{0.33}B_{0.67}$ films. Cooling the LSMO:BFO film in a 1 T

field perpendicular to the film surface results in a horizontal shift of the hysteresis loop towards the negative field direction accompanied with a strong enhancement of coercive field (H_c). The $L_{0.75}B_{0.25}$ film exhibits a remarkable exchange bias field (H_{EB}) of ~ -1020 Oe and ~ 700 Oe along the negative and positive field directions, respectively, as shown in Figure 5.5(a). In $L_{0.33}B_{0.67}$, similar loop shifts have been observed with a smaller H_{EB} (Figure 5.5(b)). The reduced magnetization in $L_{1-x}B_x$ VAN films could be explained by increased magnetic frustration states at the vertical LSMO-BFO heterointefaces. A kink behavior has been observed in the $L_{0.33}B_{0.67}$ hysteresis loop at the low magnetic field. Such behavior was previously reported in exchange-coupled FePt–Fe_3Pt nanocomposites,[212] which is related to the coexistence of both exchange-coupled and non-coupled states at the interface. Such a mixed interface state possibly occurs in $L_{0.33}B_{0.67}$ films because of the increased interface roughness.

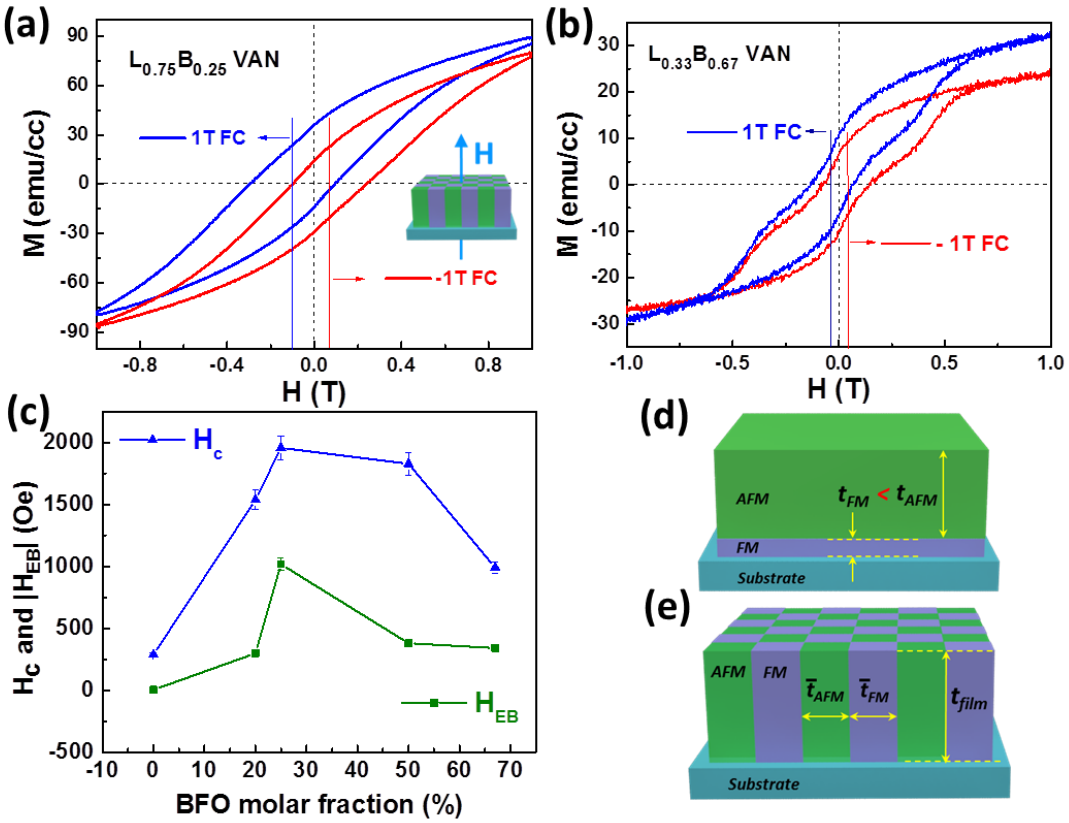

Figure 5.5. Magnetization hysteresis curves of (a) $L_{0.75}B_{0.25}$ and (b) $L_{0.33}B_{0.67}$ VAN films measured at 5 K after field cooling in +1 T (blue) and -1 T (red) field. The inset in Fig. 3a shows the cooling field direction of +1 T. (c) Dependence of exchange bias and coercive field on BFO molar fraction. The solid lines are a guide to eyes. Different requirements on film thickness for the occurrence of PEB effect in (d) bilayer and (e) VAN films. t_{FM} should be typically much smaller than t_{AFM} in bilayers, while no such limitation is applied in VAN structures.

Similar PEB results have also been observed with smaller magnitudes of H_{EB} in thinner $L_{1-x}B_x$ VAN films because of a smaller amount of AFM pinning centers for the vertical exchange coupling due to the reduced film thickness (Figures 5.6(a) and (b)). The pure LSMO film exhibits an in-plane magnetic anisotropy and no PEB effect (Figures 5.6 (c) and (d)). The magnetic behavior of pure BFO films was also carefully

examined, which shows very weak magnetization and a small coercive field (~270 Oe at 5 K).

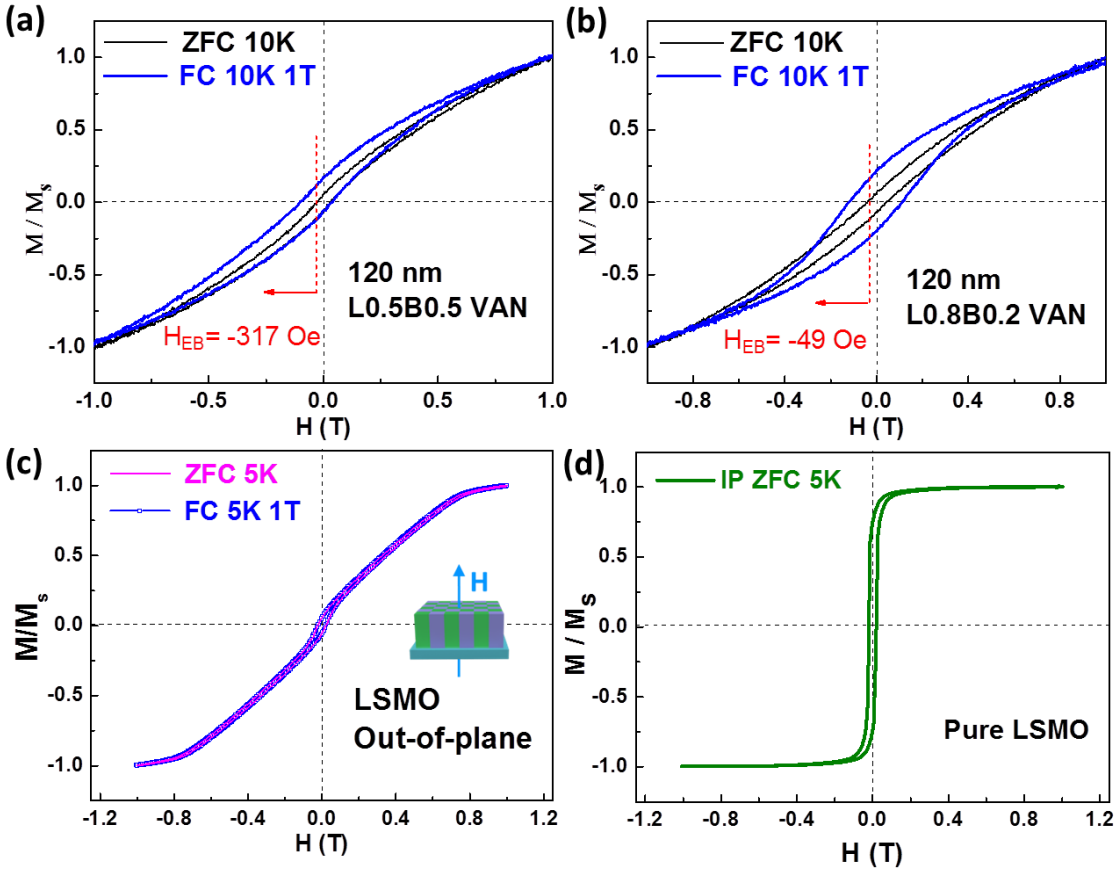

Figure 5.6. Normalized magnetization hysteresis curves of 120-nm-thick (a) $L_{0.5}B_{0.5}$ and (b) $L_{0.8}B_{0.2}$ VAN films measured at 10 K after field cooling from 300 K in +1 T (blue) and 0 T (black) field. (c) Normalized magnetization hysteresis curves of pure LSMO (out-of-plane) measured at 5 K after ZFC (pink line) and FC (blue line with squares) procedure with an out-of-plane magnetic field. (d) IP magnetization hysteresis loop of pure LSMO measured at 5 K.

In Figure 5.5(c), a large enhancement of H_c has been observed for all VAN films compared to pure single phase films, which indicates a strong coupling strength between BFO and LSMO. Both H_c and H_{EB} exhibit an initial increase with increasing BFO concentration and reach maximum values at x = 0.25. The observed H_{EB} values show a 1.4-4.5 fold enhancement of H_{EB} compared with the conventional LSMO/BFO bilayer structures depending on the specific layer structure and measurement conditions.[72,213] The above observations confirm the presence of robust PEB effects in $L_{1-x}B_x$ VAN films, providing a key evidence of strong magnetic coupling across vertical LSMO:BFO interfaces.

5.5 Proposed VAN-based model for the PEB effect

Based on the classical model studying bilayer/multilayer structures from Meiklejohn and Bean,[66,209] the H_{EB} is commonly estimated as Equation 1.6. Thus a stronger J_{ex} is typically associated with a thin FM material (within 10 nm) and a thick AFM layer (over 100 nm) in bilayer structures (Figure 5.5(d)). However, in $L_{1-x}B_x$ VAN architectures, an unexpected larger J_{ex} was observed in FM-rich films (x<0.5) given its larger H_{EB} and M_{FM}, which is unexpected from the conventional bilayer observations. It is difficult to apply the thickness concept of t_{FM} and t_{AFM} in bilayers to VAN structures, since AFM and FM phases are simultaneously grown in the vertical direction and have the same film thickness (Figure 5.5(e)). The observed enhanced H_{EB} with perpendicular anisotropy over a broad range of VAN film composition indicate effective exchange coupling in the vertical manner.

Figure 5.7 proposes a schematic model to explain the microscope origin of the vertical coupling in PEB effects in the LSMO:BFO VAN films. The detailed spin coupling structure across the vertical heterointerfaces is shown in Figure 5.7(a) and 5.7(b), where AFM spins in BFO are confined in {111} plane because of the strong ME coupling between their polarization and antiferromagnetic order.[202,203] The novel interface state is composed of uncompensated and pinned AFM spins, and coupled FM spins. The strong interactions between AFM and FM spins ate the vertical interface leads to the occurrence of PEB effect. Thus the overall exchange coupling strength (J_{ex}) is calculated by $J_{ex} = J_{AFM-w} + J_{Int} + J_{FM-w}$, where J_{AFM-w}, J_{Int} and J_{FM-w} are the spin interactions between the major compensated AFM spins and domain/interface AFM spins (J_{AFM-w}), the interfacial AFM-FM spins (J_{Int}), the domain FM spins and the major FM spins (J_{FM-w}), respectively.

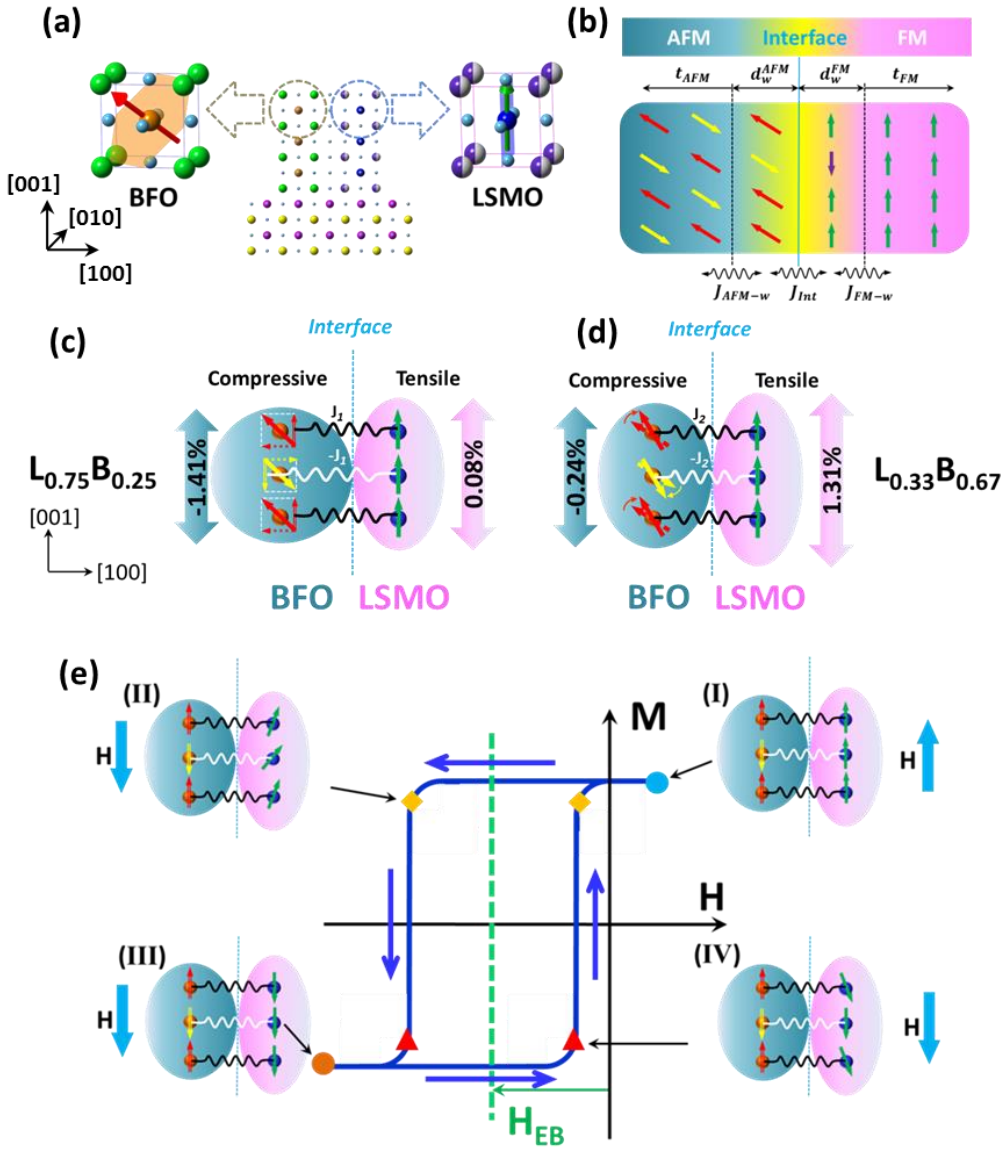

Figure 5.7. Schematic diagrams of proposed PEB mechanism induced by vertical interfacial coupling. (a) Models of spin alignment in epitaxial BFO and LSMO phases. (b) Domain formation and spin states near the interfacial region. (c) AFM spin projection in the [001] direction for vertical exchange couplings with FM spins in the $L_{0.75}B_{0.25}$ film. The red and yellow arrows depict the antiparallel AFM spins in BFO, while the green arrows represent FM spins in LSMO. The double-line and dash red arrows are the projection of AFM spins in [001] and [100] directions, respectively. BFO and LSMO unit cells are represented by the light aqua and pink ellipsoids. (d) AFM spin reorientation tuned by vertical strain in the $L_{0.33}B_{0.67}$ film. (e) Proposed spin configurations and couplings of an exchange biased hysteresis loop (I-IV).

Because of the spin canting effect in BFO, only spin vectors along the c-axis (J_1) contributes to the perpendicular anisotropy (Figure 5.7(c)). In $L_{1-x}B_x$ VAN films, as x increases, the vertical compressive strain in BFO is reduced as observed in previous XRD results. Such vertical strain tuning contributes to the AFM spin reorientation to the out-of-plane direction and enhances the perpendicular anisotropy ratio (β) of the exchange coupling strength (Figure 5.7(d)). To confirm this strain-induced spin reorientation effect, we measured both the out-of-plane and in-plane H_{EB} and calculated β by the equation of $\beta = \frac{|H_{EB-OP}|}{\sqrt{(H_{EB-OP}{}^2 + H_{EB-IP}{}^2)}}$. β signifies the AFM spin canting ratio relative to the in-plane direction. It is based on the assumption that the exchange bias field is determined by the FM-AFM spin interaction strength, given as $\bar{S}_{FM}\bar{S}_{AFM} = S_{FM}S_{AFM}\cos\alpha$, where $\bar{S}_{FM}$ (S_{FM}) and $\bar{S}_{AFM}$(S_{AFM}) are effective (actual) spin vectors, and α is the angle between FM and AFM spin.[60] Such spin re-orientation effect is confirmed by the larger β in $L_{0.33}B_{0.67}$ (85.8 %) than that in $L_{0.75}B_{0.25}$ (73.4 %) (Figure 5.8), since the increased compressive strain in the BFO (-1.41 % for $L_{0.75}B_{0.25}$; -0.24 % for $L_{0.33}B_{0.67}$) align the AFM spins towards the in-plane direction. Figure 5.7(e) shows the proposed spin configurations for the entire PEB effects. The uncompensated pinned AFM spins exert a microscopic torque on FM spins toward one single (unidirectional) direction, providing a unidirectional anisotropy energy for the bias shift.

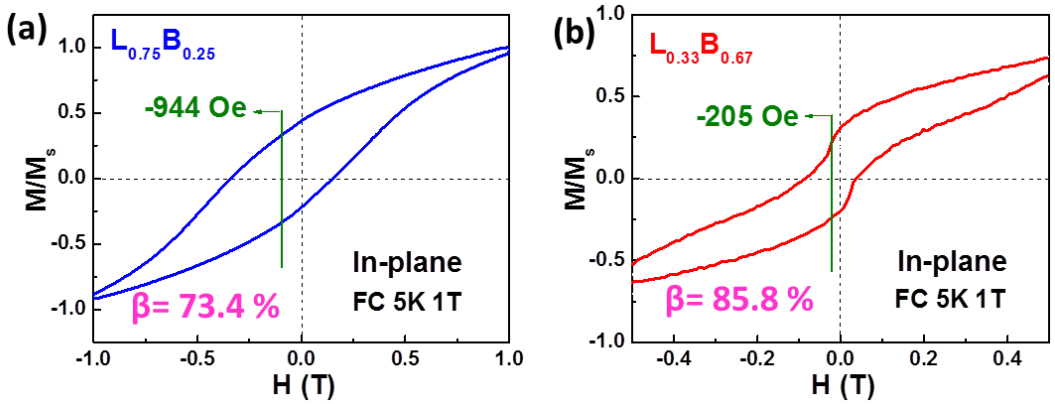

Figure 5.8. Normalized magnetization hysteresis curves of (a) $L_{0.75}B_{0.25}$ and (b) $L_{0.33}B_{0.67}$ VAN films measured at 5 K after field cooling from 300 K with +1 T field parallel to film surface.

5.6 Magnetic phase transition in LSMO:BFO VAN films

The temperature dependent behavior of the PEB effect has been investigated to obtain further insights on the interfacial exchange coupling. Figure 5.9(a) shows that the H_{EB} decreases as the temperature increases in all VAN samples and diminished to zero over the blocking temperature (T_B). With x less than 0.5, the T_B values are in the range of 20 K to 50 K, where a rapid decrease of H_{EB} was accompanied as increasing temperature to T_B. In comparison, in $L_{0.33}B_{0.67}$, a more gradual change of H_{EB} has been achieved with a T_B of ~ 100 K, strongly suggesting the significant vertical strain effect on T_B and exchange coupling strengths. Similar T_B (~100-120 K) has been reported in previous LSMO/BFO bilayer structures.[72,203] The temperature dependent behavior for H_c is shown in Figure 5.9(b).

Figure 5.9(c) shows the ZFC magnetization versus temperature (M-T) curve. It is clearly seen that the films with different compositions exhibit surprisingly different

behaviors as the temperature varies. Normalized magnetization of pure LSMO film shows an initial gradual decrease from 10 K to 300 K followed by a sharp drop as the temperature approaches its *Curie* temperature (~350 K). In $L_{0.8}B_{0.2}$ and $L_{0.75}B_{0.25}$, the ZFC curve shows a transition peak as a result of the magnetic ordering change in LSMO. With more BFO in $L_{0.5}B_{0.5}$ and $L_{0.33}B_{0.67}$, the magnetization changes more gradually in the entire temperature range. LSMO, $L_{0.75}B_{0.25}$ and $L_{0.33}B_{0.67}$ were selected as three representative samples and their corresponding dM/dT curves were plotted as the inset in Figure 5.9(c). The $L_{0.75}B_{0.25}$ film undergoes a second-order magnetic transition from paramagnetic to FM at T_c (~58 K) followed by a first-order transition from the FM to AFM at ~38 K.[214] Thus an increased amount of AFM states is expected in LSMO of the $L_{0.75}B_{0.25}$ film at 5 K, while the pure LSMO maintains more coherent FM states at low temperatures. Interestingly, this magnetic phase transition is not seen in the $L_{0.33}B_{0.67}$ film with the largest tensile strain (1.31 %) on LSMO. This could be explained by the strain-induced John-teller effect, where the large tensile strain contributes to maintain a tetragonal LSMO and stabilize its FM states over a wide temperature range.[215,216] The magnetic state transition explains the rapid decrease of its H_{EB} and H_c as the measurement temperature increases from 5 K to above 50 K with a rapidly reduced blocking temperature (T_B, ~20 K), while the $L_{0.33}B_{0.67}$ film exhibits more gradual magnetization decay with a higher T_B of ~100-120 K.

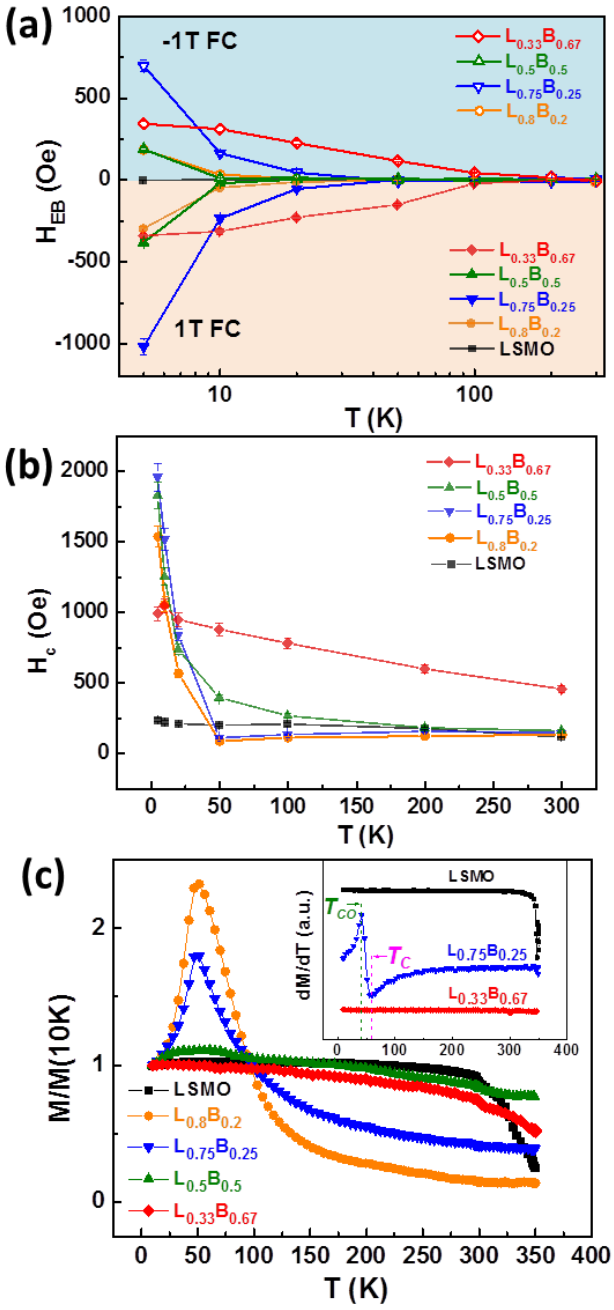

Figure 5.9. Temperature dependence of (a) H_{EB} and (b) H_c of $L_{1-x}B_x$ VAN films. The results of pure LSMO film are also shown for comparison. (c) Normalized Magnetization versus temperature for $L_{1-x}B_x$ VAN films. The inset shows derived dM/dT versus temperature for pure LSMO, $L_{0.75}B_{0.25}$ and $L_{0.33}B_{0.67}$ films.

The strain-induced magnetic phase transitions provide valuable insights on the anomalous PEB effect in VAN films: a stronger J_{ex} (or H_{EB}) but with thinner t_{AFM} in $L_{0.75}B_{0.25}$ at low temperatures. It is believed that FM and AFM domain states associated with magnetic phase transitions play an important role in the observed PEB effect. A spin-disordered/spin glass state has been observed from the bifurcation characteristics between the ZFC and FC M-T curves in both $L_{0.75}B_{0.25}$ and $L_{0.33}B_{0.67}$ films, which is because of the magnetic frustration competition between the AFM super-exchange (from BFO) and FM double-exchange (from LSMO) interactions at their interface. As shown in Figure 5.10, the larger bifurcation behavior in $L_{0.75}B_{0.25}$, as well as the transition peak in its ZFC curve, can be explained by the strain-induced mixed FM and AFM states in LSMO at low temperatures. As a result, the domain wall in LSMO (d_w^{FM}) is likely broadened with more AFM states, leading to reduced M_{FM} and t_{FM}, while J_{ex} and increase with larger d_w^{FM} based on their relationship of $d_w \propto \sqrt{J/aK}$, where a is the lattice parameter, and K is the anisotropy constant.[65] Thus larger H_{EB} and H_c are obtained with an additional source from spin-frustrate states in LSMO at low temperatures. As BFO concentration increases, the FM ordering in LSMO is stabilized by a larger out-of-plane tensile strain.[216] The spin-frustrated pinning centers for exchange coupling diminish correspondingly, which leads to smaller H_{EB} and H_c.

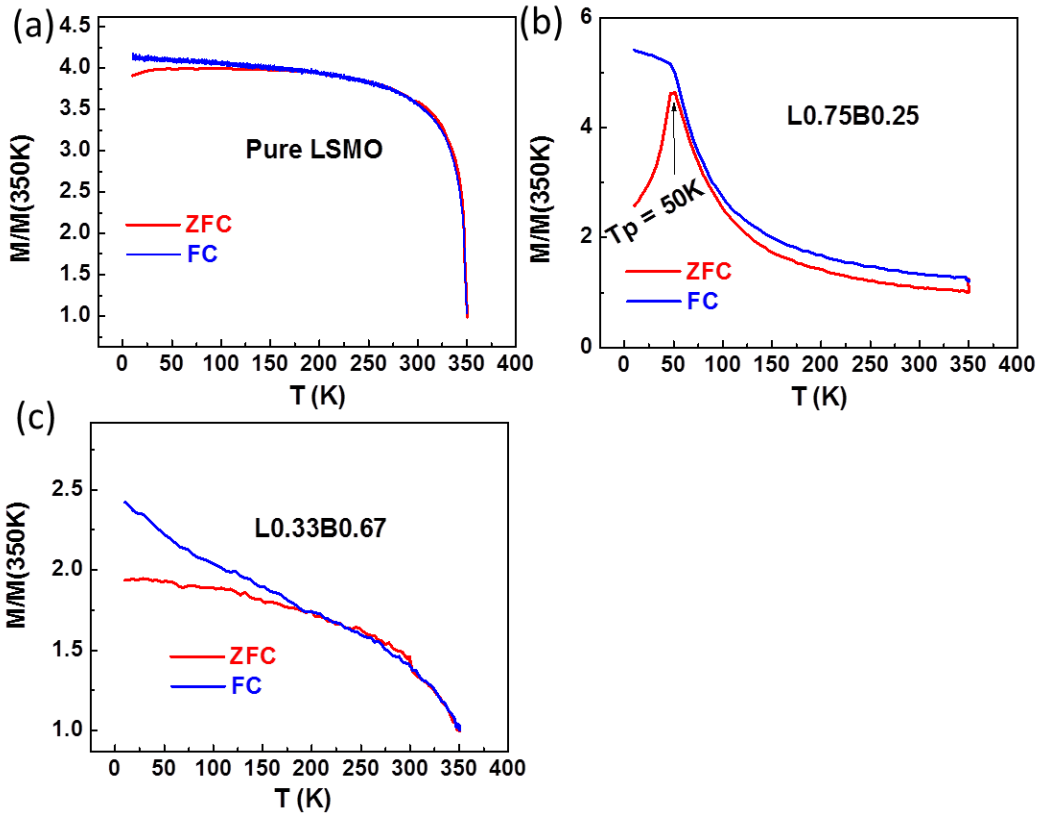

Figure 5.10. (a)-(c) ZFC and FC M-T curves of pure LSMO, $L_{0.75}B_{0.25}$ and $L_{0.33}B_{0.67}$ films.

The strong PEB effects over a wide range of film compositions in VAN structures suggest an important role of the vertical exchange coupling in obtaining the perpendicular anisotropy. The systematic variation of H_{EB} and H_c on VAN film composition suggests a promising way to manipulate the PEB effects. The film microstructure, including pillar diameters and interspacing, depends strongly on the film composition, which in turn determines the vertical interface density, strain accommodation and magnetic phase transition, and thus affects overall exchange coupling strength. Besides, a clear FE phase switching behavior has been observed in

LSMO:BFO VAN films (Figure 5.11), which suggests the possibility of using an electric field to control the exchange bias behavior. The perpendicular anisotropy achieved in micrometer thick VAN films addresses the major concern of relaxed perpendicular magnetic anisotropy found in noble metals, thus providing a feasible alternative for multifunctional devices.

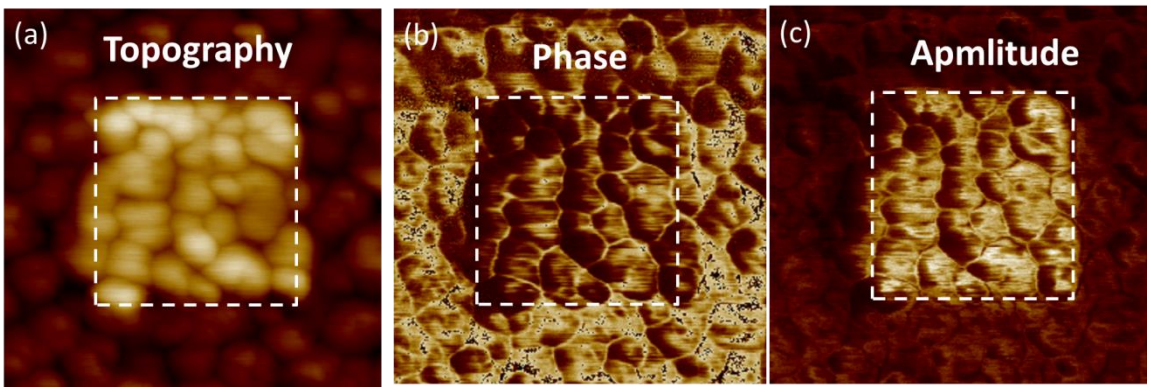

Figure 5.11. (a)-(c) The simultaneously acquired PFM topography, phase and amplitude images on an area of 1.7x1.7 μm^2 of the $L_{0.33}B_{0.67}$ film after writing the central area (0.8x0.8 μm^2) with a 5 V tip bias

5.7 Summary

We have demonstrated a strong perpendicular exchange bias effect in self-assembled LSMO:BFO vertically aligned nanocomposite films. Instead of layering thin noble metals, the vertical interfacial coupling between conventional ferromagnet and antiferromagnet has been exploited to obtain pronounced PEB effect in thick epitaxial films. The tunability of PEB effect has been achieved by careful control of the nanocomposite composition. The vertical lattice strain across the heterointerfaces has

significant effect on interfacial spin coupling orientation and domain formation, and thus influences the overall exchange bias behavior. The results demonstrate that this VAN approach holds a great promise to explore perpendicular EB effect in alternative vertical architecture towards high density memory devices.

CHAPTER VI

PERPENDICULAR EXCHANGE BIASED MAGNETOTRANSPORT AT THE VERTICAL HETEROINTERFACE OF $La_{0.7}Sr_{0.3}MnO_3$:NiO NANOCOMPOSITES[4]

6.1 Overview

Heterointerfaces in manganite-based heterostructures in either layered or vertical geometry are considered as one of the keys to manipulate and improve the magnetotransport properties. Instead of using the spin polarized tunneling *across* the interface, a unique approach based on the magnetic exchange coupling *along* the vertical interface to control magnetotransport properties has been demonstrated. By coupling ferromagnetic $La_{0.7}Sr_{0.3}MnO_3$ and antiferromagnetic NiO in an epitaxial VAN architecture, a dynamic and reversible switch of the resistivity between two distinct exchange biased states has been achieved. This study explores the use of vertical interfacial exchange coupling to tailor magnetotransport properties, which may serve as a viable route for spintronic applications.

[4] This chapter is reprinted with permission from "Perpendicular Exchange-Biased Magnetotransport at the Vertical Heterointerfaces in $La_{0.7}Sr_{0.3}MnO_3$:NiO Nanocomposites." by W. Zhang, et al., ACS Applied Materials & Interfaces, 2015, 7, 21646-21651.

6.2 Introduction

Heterointerfaces constructed in complex oxides add an extra degree of freedom for obtaining unexpected physical properties. Such heterointerfaces are typically achieved in a horizontal layered geometry such as bilayers, multilayers and superlattices.[169,205] Vertically-oriented heterointerfaces in self-assembled two-phase VAN films have emerged very recently as another promising pathway for enhanced and tunable functionalities.[118,119,122] For example, the vertical strain coupling, owing to the lattice mismatch between two component phases, could lead to enhanced physical properties and new functionalities which could be difficult to achieve via their single phase constituent. Representative examples include sizeable ME coupling in both BTO:CFO [55] and BFO:CFO films,[111] and increased *Curie* temperature in BTO:Sm_2O_3 films through nanocomposite-induced strain.[114] Besides, the increased spin scattering effect across the grain/phase boundaries have been employed to enhance the magnetotransport properties in LSMO:ZnO nanocomposite films.[153,188]

The LFMR in manganite-based materials is one of most intriguing phenomena with promising applications for magnetic memory devices. The nanocomposite approach has been widely used to improve the LFMR performance by introducing secondary phases such as ZnO,[153,188] MgO,[121] CeO_2,[130] NiO [132] and glass.[44] Despite different microstructures related to specific material systems, substrate lattice parameters and orientations, the magnetotransport properties in VAN films are mostly investigated in the current-in-plane geometry (simplified as IP in the following section), where the current transports perpendicular to the vertical heterointerfaces. However, the study on

electron transport along the vertical heterointerfaces (the current-perpendicular-to-plane geometry, simplified as OP), particularly the magnetotransport, is scarce. On the other hand, the exchange bias effect, i.e., originated from the interfacial magnetic coupling and pinning effects at the FM-AFM heterointerfaces, has been exploited as a cornerstone in commercial magnetic storage devices.[60,72] The strong interactions between the spin configuration and the electron transfer are expected to add another degree of control on the magnetotransport in the OP geometry. Here, we demonstrate perpendicular exchange biased magnetotransport using the strong magnetic exchange coupling at the vertical FM-AFM heterointerfaces. A LSMO:NiO (FM-AFM) VAN system has been selected for this demonstration. Besides the anisotropic electron transport behavior, the magnetotransport property of the VAN films could be reversibly switched between two distinct exchange biased states under an applied magnetic field through a field cooling procedure.

6.3 Experimental method

Pure LSMO and LSMO:NiO (with a molar ratio of 3:2) nanocomposite films with a thickness of 70~100 nm were grown on single-crystal $SrTiO_3$ (001) substrates at 750 ℃ in 200 mTorr of oxygen using pulsed laser deposition with a KrF laser (Lamda Physik, λ = 248 nm) at a repetition rate of 10 Hz. The laser energy density is 2.2 J/cm^2. After depositions, the samples were cool down in an oxygen pressure of 200 Torr at a cooling rate of 5 ℃/min. The epitaxial quality and microstructure of all samples were investigated with high-resolution XRD (PANalytical Empyrean diffractometer) using Cu-K_α radiation and TEM (FEI Tecnai G^2 F20). For high-resolution STEM and EDS

mapping, a FEI Titan G2 800-200 STEM with as a Cs probe corrector and ChemiSTEM technology (X-FEG and SuperX EDS with four windowless silicon drift detectors) operated at 200 kV was used. Au electrodes were deposited by sputtering on top of films for electrical property measurements. The sample resistivity was measured in a PPMS (Quantum Design, Model 6000). For the FC and ZFC measurements, the samples were cooled down from 300 K to target temperatures under the magnetic field of 1 T and 0 T, respectively. The substrate signals have been subtracted for all measured samples.

6.4 Epitaxial growth of LSMO:NiO VAN films

Figure 6.1(a) shows the typical θ-2θ XRD scans of both LSMO:NiO VAN and pure LSMO films with the same thickness. It is obvious that only the LSMO (00*l*) and NiO (00*l*) peaks are present along with the $SrTiO_3$ (STO) (00*l*) peaks, indicating the highly textured OP film growth. Figures 6.1(b) and 6.1(c) show the reciprocal space maps (RSM) near the substrate STO (113) peak of the pure LSMO and the LSMO:NiO films, respectively. The broad LSMO peak observed in the pure film indicates a systematic variation of lattice parameters as there is a gradual substrate-induced strain relaxation with increasing film thickness. In the VAN film, however, the LSMO (113) peak is shifted much closer to STO (113) peak with a much narrower lattice parameter variation as indicated by the sharper peak. A similar peak shift and narrower peak have also been observed in the RSM data near STO (002) for pure LSMO and LSMO:NiO films, respectively (Figure 6.2), suggesting a vertical strain coupling between LSMO ($d_{\mathrm{LSMO}<001>}$ = 3.87 Å) and NiO ($d_{\mathrm{NiO}<001>}$ = 4.17 Å). For the VAN films, the RSM peak

shift of LSMO corresponds to an OP *tensile* strain of 0.53 % (with respect to the pure film) and a more relaxed IP *tensile* strain of 0.08 %.

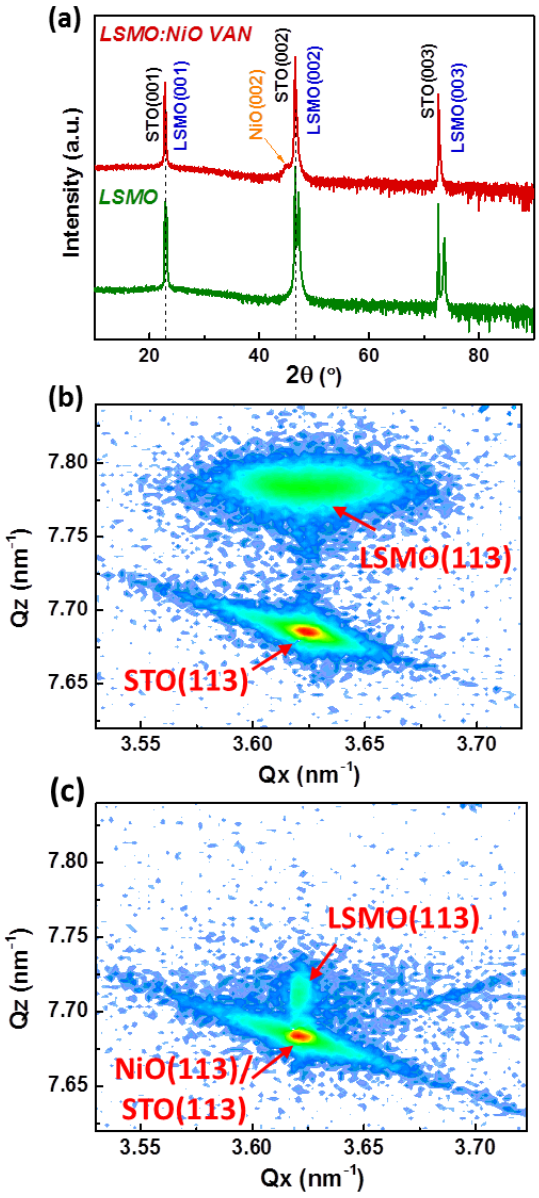

Figure 6.1. (a) θ-2θ XRD scans of pure LSMO and LSMO:NiO VAN films. (b,c) Reciprocal space maps near (113) STO for (b) pure LSMO and (c) LSMO:NiO nanocomposite films on the STO (001) substrate.

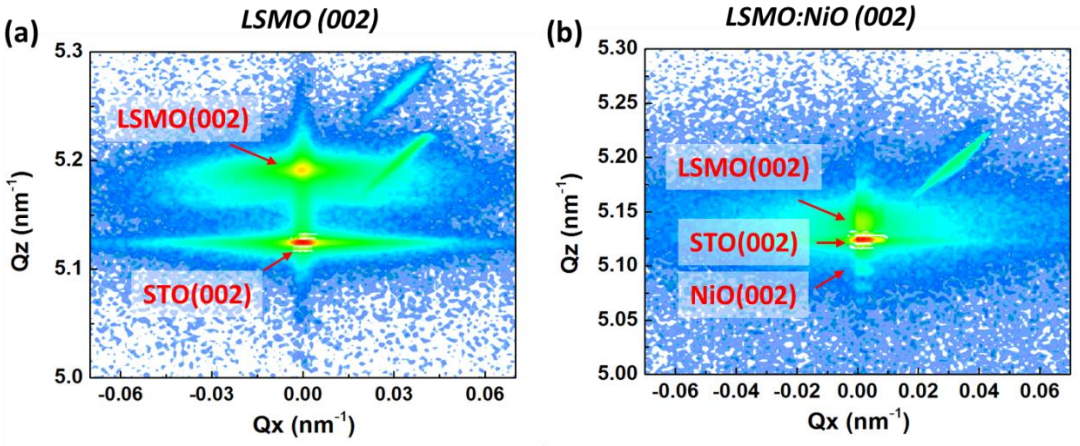

Figure 6.2. Reciprocal space maps near STO (002) for (a) pure LSMO and (b) LSMO:NiO nanocomposite films on the STO (001) substrate.

6.5 Microstructure and vertical interface of LSMO:NiO VAN films

Transmission electron microscopy (TEM) and scanning transmission electron microscopy (STEM) analyses in the high-angle annular dark-field (HAADF) mode were conducted to investigate the microstructure and phase distribution of the LSMO:NiO VAN films. Figure 6.3(a) shows the plan-view STEM image of a LSMO:NiO nanocomposite film. It is obvious that self-assembled NiO nanocolumns (*in dark contrast*) with an average diameter of 2 nm and an interspacing of 3.5 nm are uniformly distributed in the LSMO matrix (*in bright contrast*). The inset in the Figure 6.3(a) shows a high-resolution image of a single NiO nanopillar within the LSMO matrix, demonstrating very high epitaxial quality of these two phases and atomically sharp heterointerface between them. The energy-dispersive X-ray spectroscopy (EDS) mapping results demonstrate distinct phase separation between NiO and LSMO (Figure 6.3(b)). The self-assembled VAN structures can also be seen from their low

magnification cross-sectional STEM image and the high-resolution TEM image (Figures 6.3(c) and 6.3(d)). The corresponding selected area electron diffraction (SAED) pattern in Figure 6.3(e) combined with the above XRD results confirms the orientation relationships between LSMO and NiO with the underlying STO substrate, i.e., $(001)_{LSMO} \parallel (001)_{NiO} \parallel (001)_{STO}$ (*out-of-plane*) and $[100]_{LSMO} \parallel [100]_{NiO} \parallel [100]_{STO}$ (*in-plane*).

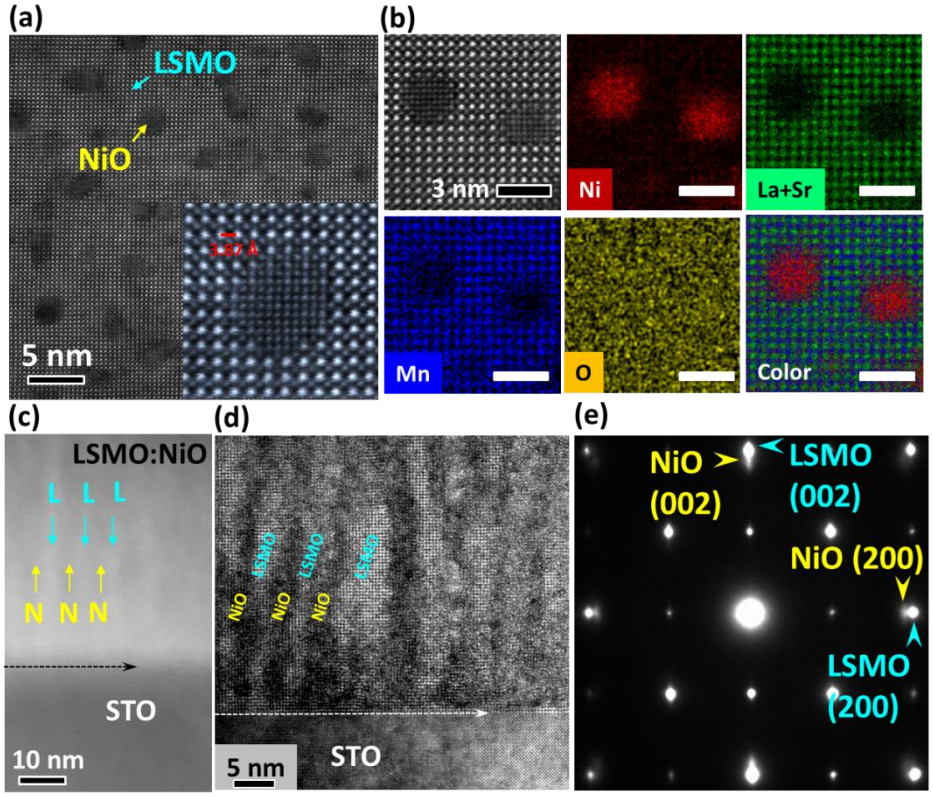

Figure 6.3. (a) Plan-view STEM image of the LSMO:NiO VAN film on the STO substrate. The inset shows a high-resolution image of a single NiO nanopillar embedded in the LSMO matrix. (b) EDS maps of Ni, La+Sr, Mn, O and color map obtained from the area of the selected plan-view STEM image. The scale bars are 3 nm. (c) Cross-sectional STEM image and (d) high-resolution TEM image of the LSMO:NiO nanocomposite film showing periodically arranged nanopillars. (e) The corresponding SAED pattern of the cross-sectional film.

6.6 Anisotropic electron transport of LSMO:NiO VAN films

Electrical transport measurements were carried out in both IP and OP configurations for pure LSMO and LSMO:NiO VAN films, as illustrated in the schematics in Figure 6.4(a) (OP, top left and IP, bottom right). The external magnetic field was applied along the OP direction for magnetotransport measurements. A 15-nm-thick $SrRuO_3$ (SRO) bottom electrode was applied for OP measurements. Figure 6.4(a) shows the temperature dependent IP and OP normalized resistivity (R(T)) of the LSMO:NiO VAN film (ρ_{OP-VAN} and ρ_{IP-VAN}). A metal-to-insulator transition has been observed in ρ_{IP-VAN} with a transition temperature (T_{MI}) of ~248 K, which could be attributed to the strong suppression of double exchange interaction between the neighboring LSMO grains decoupled by NiO. On the other hand, a continuous decrease in ρ_{OP-VAN} has been observed within the test temperature range. This can be explained by the fact that the electron transport is mainly through the conducting LSMO channels along the OP direction. Because of the series connection between the upper films and the SRO, the possible contribution from SRO on the entire film resistivity has been carefully examined. It is also noted that the effect from SRO is minor with the incorporation of NiO in VAN films, as evidenced by the increase of ρ(10 K)/ρ(340 K) ratio from the bare SRO layer (15.8 %) (Figure 6.5) to those in series connected with pure LSMO (25.4 %) and LSMO:NiO VAN films (62.2 %), as well as the 20-80 times larger ρ_{OP-VAN} than the pure SRO film resistivity depending on the measurement temperature. As a comparison, the R(T) curves of the pure LSMO film were also presented. In Figure 6.4(b), both $\rho_{IP-LSMO}$ and $\rho_{OP-LSMO}$ decrease monotonously with decreasing test temperature from

340 K to 10 K and exhibit a metallic-like behavior below its *Curie* temperature (~ 350 K).[17]

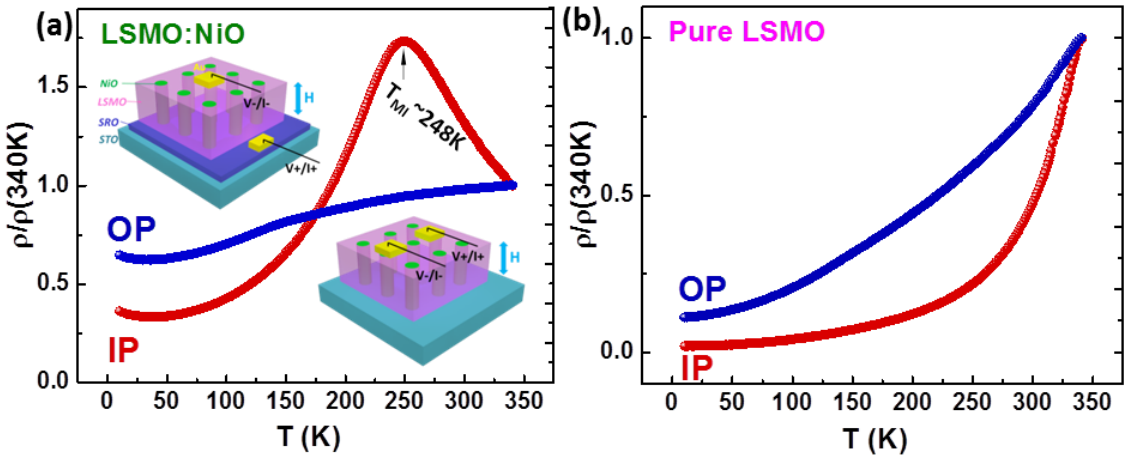

Figure 6.4. Temperature dependence of normalized OP and IP zero-field resistivity of (a) LSMO:NiO VAN and (b) pure LSMO films. Inset in Figure 6.4(a) shows the schematic drawings of out-of-plane (OP, top left) and in-plane (IP, bottom right) resistivity measurements, respectively. The magnetic field for magnetotransport measurements is applied perpendicular to the film surface.

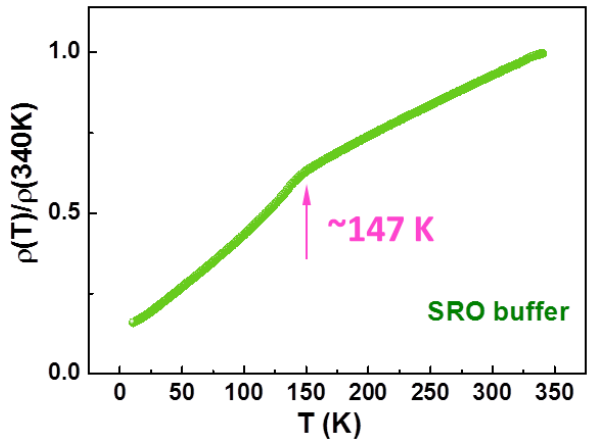

Figure 6.5. Normalized ρ_{IP} of a 15-nm-thick SRO layer as a function of temperature.

The temperature dependent MR data of both pure LSMO and LSMO:NiO VAN films show that ρ_{IP-VAN} has the largest MR value of -17.1 % at ~227 K under the field of 1 T (Figure 6.6), which could be explained by the largest spin-dependent scattering and tunneling effects obtained in the IP configuration of the nanocomposite film.[128]

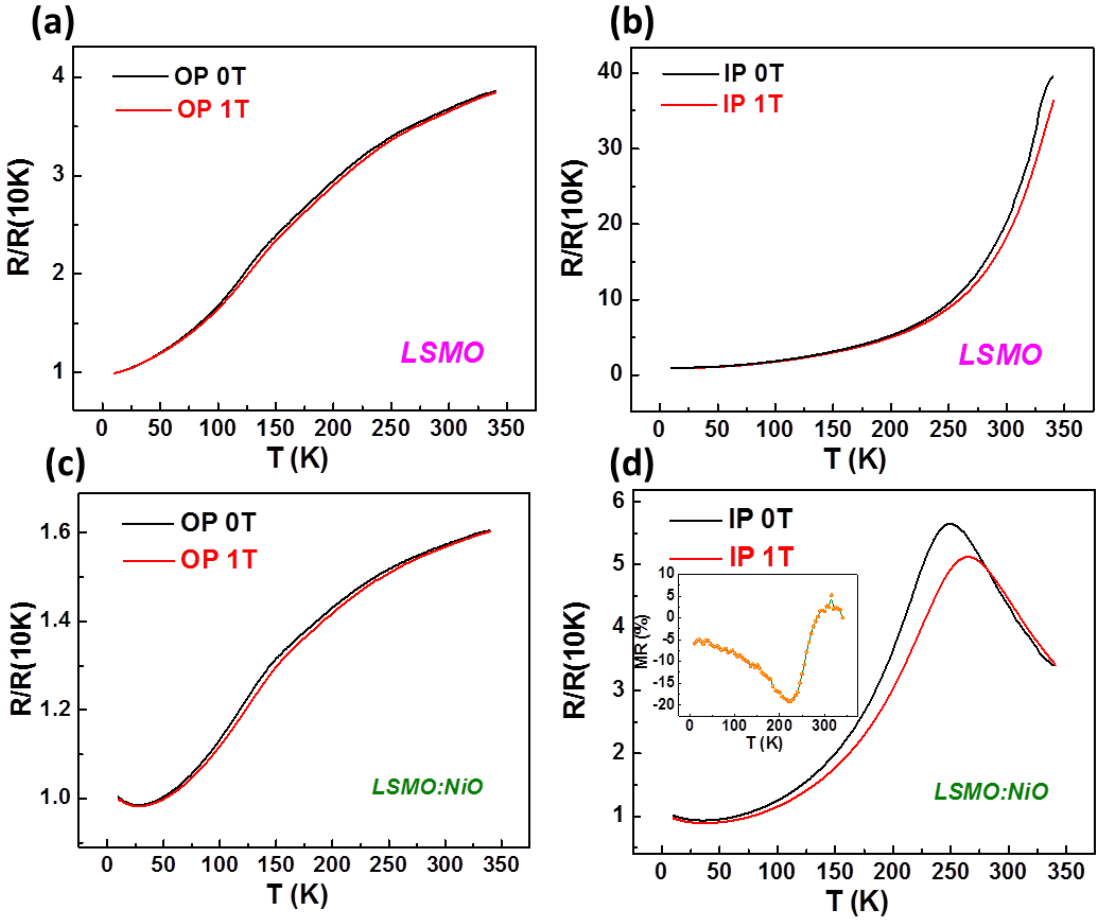

Figure 6.6. (a-d) Temperature dependence of normalized (a,c) ρ_{OP} and (b,d) ρ_{IP} of pure LSMO film and LSMO:NiO VAN films under 0 T and 1 T field. The inset in Figure 6.6(d) shows the corresponding temperature dependent MR data. The MR is defined as MR = (R(H)-R(0))/R(0), where R(H) is the resistivity under a magnetic field, and R(0) is zero-field resistivity.

6.7 Perpendicular exchange biased magnetotransport of LSMO:NiO VAN films

More importantly, the focus of this study is to investigate the effect of the magnetic exchange coupling at the vertical heterointerfaces on the dynamic tunability of the magnetotransport property. Such a dynamic tuning effect has not yet been demonstrated in epitaxial VAN architectures and could provide an alternative way for magnetotransport control. Figure 6.7(a) shows the normalized ρ_{OP-VAN} versus the magnetic field (R(H)) measured at 10 K after field cooling (FC) under a magnetic field of 1 T and -1 T. ρ(H) and ρ(0) represent the resistivity with and without a magnetic field, respectively. It is interesting to observe that the R(H) curves shift towards either the negative or positive field with a pronounced bias field of -584 Oe or 527 Oe, respectively depending on the cooling field direction. The asymmetric shape of R(H) curves is ascribed to the interfacial FM-AFM exchange coupling, which induces a unidirectional anisotropy (K_U) in the FM phase and influences its magnetotransport.[217]

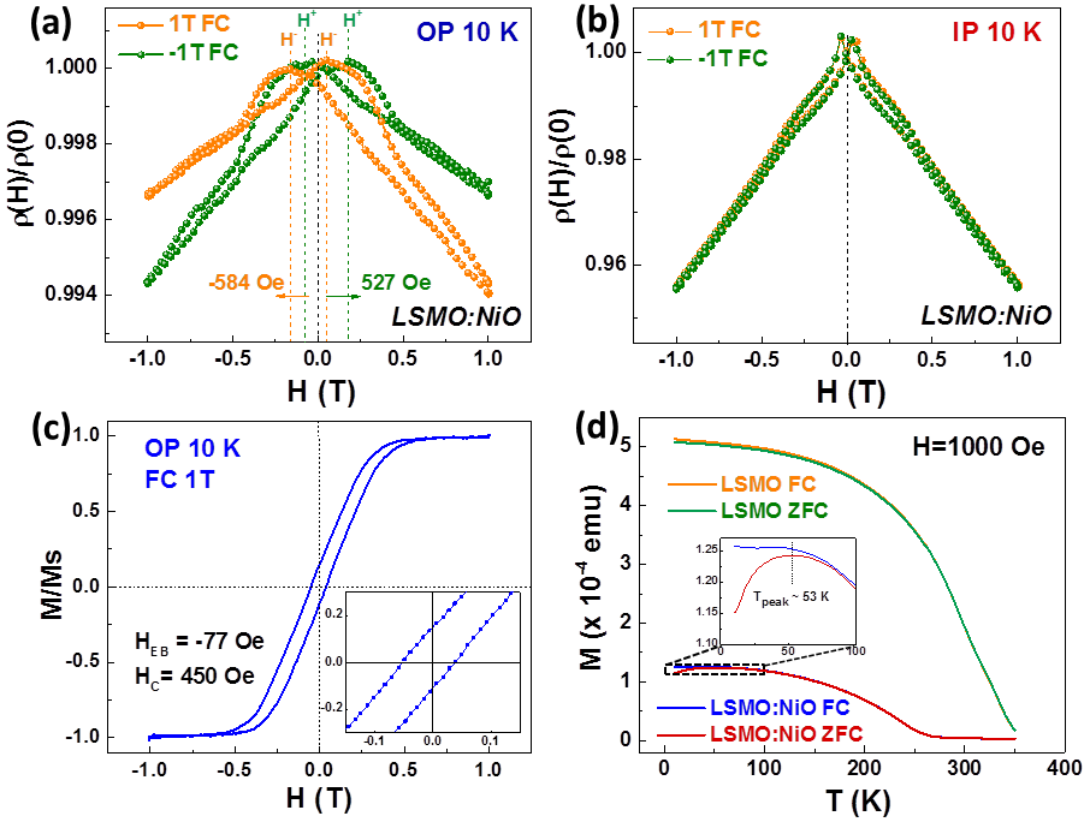

Figure 6.7. (a,b) Magnetic field dependence of normalized (a) ρ_{OP} and (b) ρ_{IP} of the LSMO:NiO VAN film after FC to 10 K in a 1 T and -1 T field. (c) Magnetic hysteresis curves of the LSMO:NiO film with the same FC procedure. The inset is the enlarged part of the bias shift. (d) Temperature dependence of ZFC and FC magnetization of pure LSMO and LSMO:NiO films measured with a IP magnetic field of 1000 Oe. The inset shows the enlarged part of the bifurcation behavior between ZFC and FC curves.

When the exchange coupling disappears under a zero field cooling, K_U vanishes and thus leads to a more symmetric R(H) curve (Figure 6.8(a)). To confirm the unique role of vertical exchange coupling in controlling the magnetotransport properties, the field-cooled R(H) data of ρ_{IP-VAN} (Figure 6.7(b)) and $\rho_{OP-LSMO}$ (Figure 6.8(b)) were carefully examined, and no shift behavior has been observed.

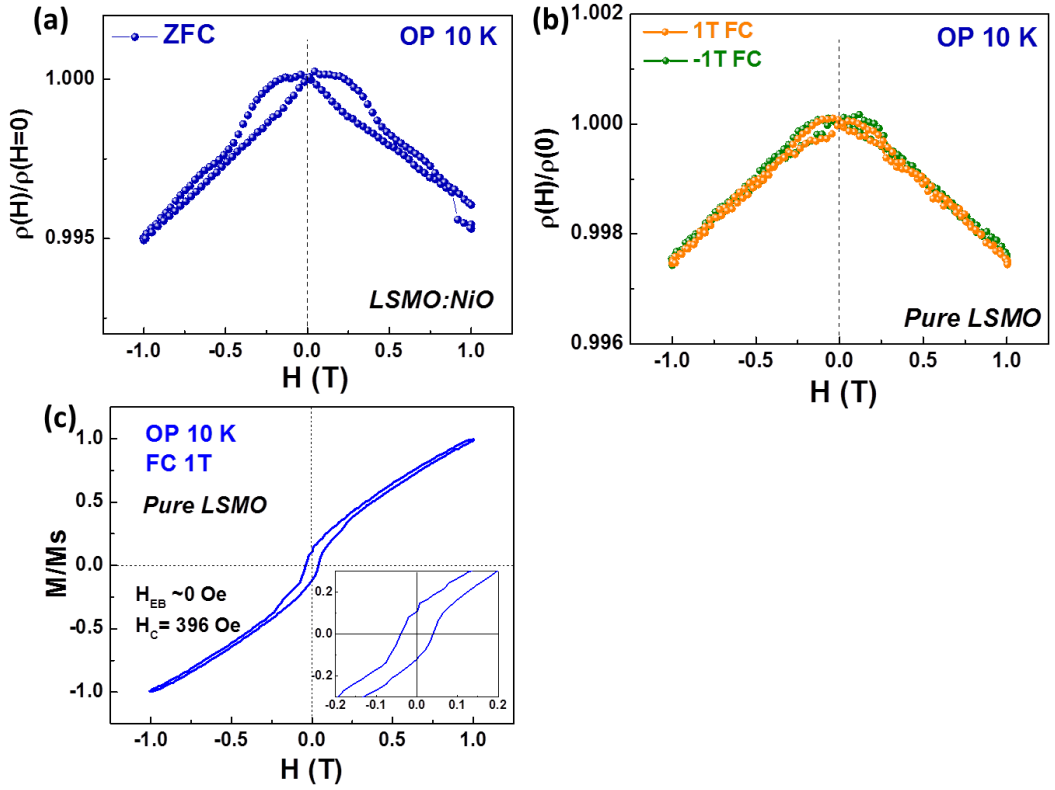

Figure 6.8.(a) Magnetic field dependence of normalized ρ_{OP} of the LSMO:NiO film under zero field cooling to 10 K. (b) Magnetic field dependence of normalized ρ_{OP} of the pure LSMO film after field cooling to 10 K in a 1 T and -1 T field. (c) Magnetic hysteresis curves of pure LSMO with the same FC procedure. The inset is the enlarged image of the center part.

The perpendicular exchange bias effect at LSMO:NiO vertical interfaces was further investigated by the magnetic hysteresis loops (M(H)) of the LSMO:NiO nanocomposite film measured at different temperatures. As shown in Figure 6.7(c), after 1 T FC to 10 K, the M(H) curve of the LSMO:NiO film exhibits a horizontal shift with an exchange bias field (H_{EB}) of -77 Oe and a coercive field (H_c) of 450 Oe. In comparison, the FC data of the LSMO film shows no bias shift and a smaller H_c of 396 Oe due to the lack of exchange coupling (Figure 6.8(c)). It is noted that the H_{EB} and H_c

obtained from the M(H) curves are much smaller than those from the R(H) results. The discrepancy can be understood by the difference between these two measurement techniques. The bias fields measured from R(H) tests are determined by the average pinning field of the entire FM-AFM interfaces, while the values from M(H) curves are dominated by the weakest site for the occurrence of nucleation during the magnetization reversal.[218,219] Hence the M(H) technique measures the lowest limit of the actual H_{EB} associated with the weakest pinned region, and thus gives much smaller values than those from R(H) tests. In the material systems with uniform exchange coupling at the interface, H_{EB} measured from M(H) and R(H) tests agrees with each other, as observed in FeMn/NiFe exchange biased spin valves [220] and high-quality CoO/Co and CoO/Fe bilayers. [221] On the other hand, the discrepancy of H_{EB} becomes significant in the presence of irreversible AFM domain formation and rearranged spin coupling, which strongly relates to the interface structure and geometry. Similar effects have also been observed in previous studies of exchange biased Co/CoO bilayers [222] and antidote arrays [218,223] probed with magnetization hysteresis and anisotropic MR techniques. In LSMO:NiO VAN films, the self-assembled high-density vertical interfaces give rise to larger interfacial spin fluctuations and thus leads to the observed discrepancy effect.

Figure 6.7(d) presents the zero field cooling (ZFC) and FC data of magnetization as a function of temperature (M(T)) measured with an in-plane magnetic field of 1000 Oe. First, it is noticed that the measured T_c (~234 K, defined as the temperature where the dM/dT reaches the minimum value) is consistent with the T_{MI} measured in Fig.3d (i.e. 248 K). The bifurcation between the ZFC and FC M(T) curves at T_{irr} (~75 K) and a peak

observed in ZFC MT data at T_{peak} (~53 K) indicates the existence of spin-disordered states in the VAN film, which is not seen in the pure LSMO film. This could be resulted from their competing magnetic orders and spin frustration at LSMO-NiO heterointerfaces, as seen in other LSMO-based heterostructures.[128,224] As the temperature increases, the magnetic exchange coupling strength between LSMO and NiO is significantly weakened with a rapid decay of the FM ordering in LSMO. As the measurement temperature increases to 150 K, the R(H) curve after 1 T cooling to 150 K presents no shift to either direction (Figure 6.9(a)), and the H_{EB} from the M(H) measurement decreases to 0 Oe accompanied with the decrease of the coercive field (Figure 6.9(b)), suggesting a full relaxation of the exchange coupling between LSMO and NiO.

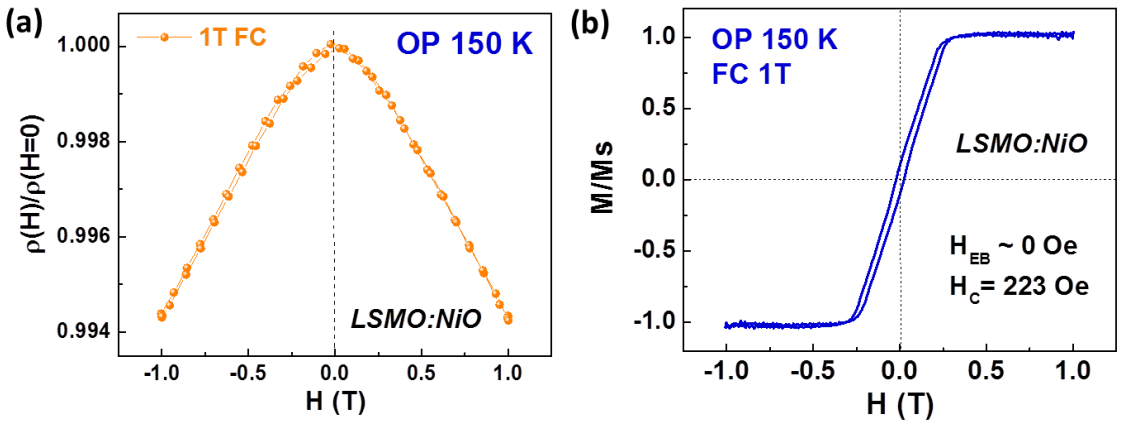

Figure 6.9. (a) Magnetic field dependence of normalized ρ_{OP} of the LSMO:NiO VAN film after 1 T cooling to 150 K. (b) The corresponding magnetic hysteresis loop with the same FC procedure.

The above experimental results demonstrate the unique role of the perpendicular exchange coupling at the vertical heterointerfaces on tuning the OP magnetotransport properties of the LSMO:NiO VAN films. The strong dependence of the OP electron transport on the interfacial exchange coupling indicates a different transport-controlled mechanism compared to those reported in bilayer/multilayers, polycrystalline nanocomposite and bulk materials. In conventional layered magnetic tunneling junctions (MTJs) or VAN structures for in-plane transport, the spin-polarized tunneling and spin filtering effects have been typically used to enhance the magnetotransport property. [225-227] On the other hand, for the OP transport of the VAN films, the spin-polarized tunneling effect becomes minor since the tunneling barrier (equivalent to the film thickness) is extremely high and electros are mainly transported through the conducting channels. Instead, the interfacial exchange coupling at the vertical interface introduces anisotropic constraints on the FM spin rotation during external perpendicular field switching, and thus influences magnetotransport properties. More importantly, by tuning the vertical interface density in the VAN structure, one can control the overall exchange coupling strength and resultant magnetotransprot properties. This has been evidenced by comparing the results of the LSMO:NiO VAN films with different nanopillar sizes and interspacings. As shown in Figure 6.10, when the deposition frequency was change to 1 Hz, the LSMO:NiO VAN film with a larger napillar size (~3.3 nm) and interspacing (~5.7 nm) has been obtained, which results in reduced pillar density and vertical interface density. As a result, the R(H) curves shows much smaller shift (~50 Oe) under the same FC procedure.

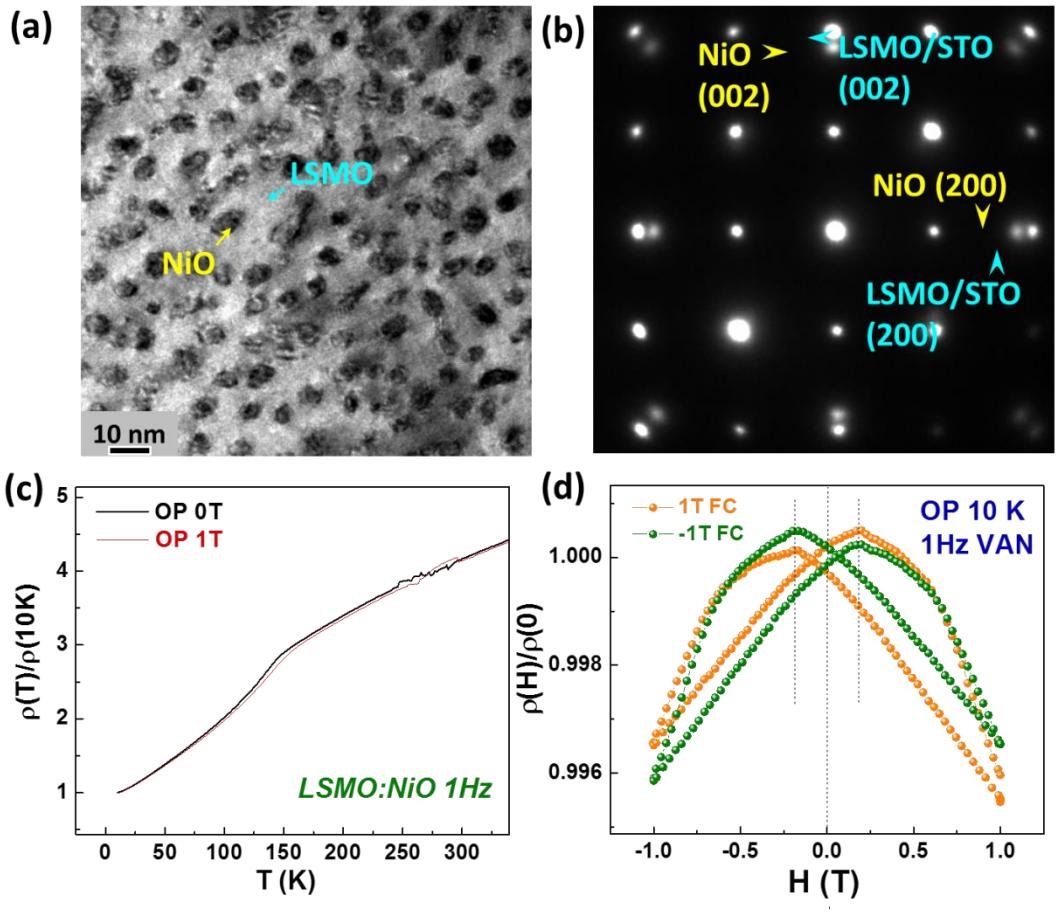

Figure 6.10. (a) Plan view TEM image and (b) corresponding selected area diffraction pattern of the LSMO:NiO VAN film deposited by 1 Hz. (c) Temperature dependent ρ_{OP} measured with 0 and 1 T field, and (d) magnetic field dependent resistivity after field cooling with an out-of-plane 1 T and -1T field of as-deposited VAN films under 1 Hz.

6.8 Summary

Self-assembled LSMO:NiO vertically aligned nanocomposite films have been grown using pulsed laser deposition with a uniform morphology of highly ordered, ultrafine NiO nanopillars embedded in the LSMO matrix. The anisotropic electron transport properties in both the current-in-plane (IP) and current-out-of-plane (OP) geometries have been investigated. The vertical LSMO-NiO heterointerfaces in the

nanocomposite films demonstrate pronounced magnetic exchange coupling at low temperatures, indicated by the observed exchange bias effect. More interestingly, such a vertical interface coupling enables a dynamic and reversible control of magnetotransport properties. This study demonstrates that the exchange coupling at the vertical FM-AFM heterointerfaces introduces an alternative approach to manipulate magnetotransport properties in epitaxial oxide nanocomposite films.

CHAPTER VII

HETEROINTERFACE DESIGN AND STRAIN TUNING IN EPITAXIAL $BiFeO_3$:$CoFe_2O_4$ NANOCOMPOSITE FILMS

7.1 Overview

The ability to control the morphology of heterointerfaces with coupled functionalities is fascinating from both fundamental and technological perspectives. Here, using BFO:CFO VAN films as a model system, we demonstrate a simple and effective method to modulate the heterointerface and its morphology in nanocomposite films using pulsed laser deposition. By tuning the deposition frequency through thickness during film growth, both vertically straight and gradient heterointerfaces have been achieved. The modulated heterointerface is strongly correlated with strain tuning and interface coupling, and thus modifies the magnetic anisotropy, coercive fields and FE switching behavior. This study provides viable approach for tailoring the interface strain and coupling in VAN and achieving tunable physical properties.

7.2 Introduction

Multiferroic heterostructures, composed of a ferromagnet/ferrimagnet and a FE material, have exhibited combined and/or enhanced physical properties through interface coupling.[2,81,109] Recently, vertically aligned nanocomposite (VAN) films have been exploited to create various multiferroic systems,[116,118] particularly the multiferroic perovskite-spinel nanocomposites, for example, BTO, PTO and BFO as the perovskite FE; CFO, $NiFe_2O_4$ and $MgFe_2O_4$ as the spinel ferromagnet/ferrimagnet,[55,134,227] the perovskite-layered oxide nanocomposites ($Bi_5Ti_3FeO_{15}$:CFO)[228] and others.[229] To engineer the multiferroic performance of VAN films, much efforts have been devoted to controlling the vertical heterointerfaces and lattice strain modulation, which is strongly correlated with the magnetic anisotropy, coercive filed, and FE polarization switching.[110,125,230,231] To control the nanocomposite film morphology and microstructure, one can vary the substrate orientation (thus the associated surface energy) and film composition,[115] or pattern a highly ordered seed layer.[155] Alternatively, adjusting the deposition frequency (*f*) in pulsed laser deposition is another effective way for the microstructure control, which can be complement to previous approaches.[117,124]

The growth of the multiferroic BFO:CFO system is dominated by a nucleation-and-growth mode,[115] in which surface diffusion of adatoms plays an important role in forming the VAN structure. At a constant temperature, the diffusion length of adatoms (L) can be estimated as $L = 2\sqrt{D\tau}$, where D is the diffusion coefficient and τ is the diffusion time.[117] Thus a lower f leads to a longer τ, which results in a longer L and larger pillar size. With gradual tuning of f from high to low (or vice versa), one could

achieve a modulated VAN structure with different interface shapes and pillar dimensions as illustrated in Figure 7.1. Therefore, continuously gradient CFO nanopillars in a planar BFO matrix can be obtained by careful control of *f* during deposition. Furthermore, the modulated VAN structure could also alter the interface coupling and vertical lattice strain accommodation, which in turn, affects overall physical properties. In this letter, we report the unique gradient heterointerfaces in BFO:CFO VAN films by such a modulated growth method. Detailed analysis of microstructure, magnetic and FE property suggests that such vertical interface control could be a viable approach in designing VAN films with tunable microstructures and functionalities.

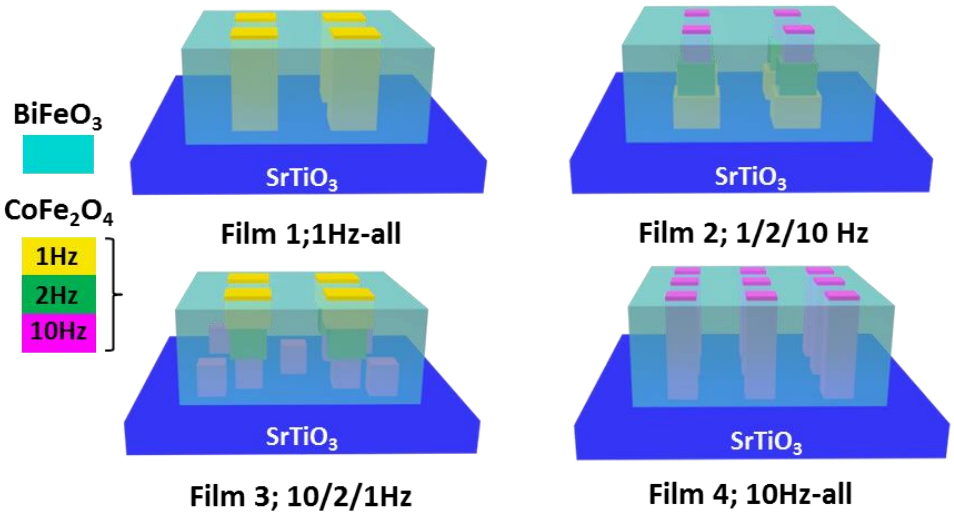

Figure 7.1. Schematic microstructure and heterointeface design.

7.3 Experimental section

The composite target containing BFO and CFO in a molar ratio of 67:33 was prepared by a conventional ceramic sintering process. The BFO:CFO VAN films were grown on single-crystal $SrTiO_3$ (STO) (001) substrates at 700 ℃ in 100 mTorr of oxygen by pulsed laser deposition using a KrF excimer laser (λ = 248 nm) with a laser fluence of 1.9 J/cm^2. Different laser frequencies *f* (1Hz, 2 Hz and 10 Hz) were used during growth and the total film thickness was kept at 100-120 nm. After deposition, all the films were cooled in 500 Torr oxygen at a cooling rate of 5 ℃/min. For electrical property test, 30-nm-thick $SrRuO_3$ films were first grown on STO as a bottom electrode at 700 ℃ in 200 mTorr of oxygen.

7.4 BFO:CFO VAN film growth and strain tuning

The film growth and strain tuning in BFO:CFO films deposited with different *f* were first analyzed by X-ray diffraction (XRD). The highly textured growth of Films 1-4 can be seen from θ-2θ XRD scans in Figure 7.2(a). Figure 7.2(b) shows the local XRD scans near STO (002) diffraction peak. The peak shift to a lower (higher) angle in CFO (BFO) suggests a compressive (tensile) strain along the out-of-plane direction. This systematic shift suggests an effective vertical strain coupling at the BFO:CFO interfaces, compared to the mostly relaxed substrate-induced strain in as-grown thickness. The wider BFO (002) peak suggests that BFO depends more sensitively on the vertical lattice mismatch, because the bulk moduli of bulk *rhombohedral* BFO (75.5±15.5 GPa)[232] are much smaller than that (~185.7 Gpa) in bulk *spinel* CFO.[233] It should be noted that the presence of mixed (tetragonal and rhombohedral) or twined phases could also play a role

in the peak spread. However, the tetragonal BFO corresponds to a diffraction peak at 38-39 degree,[101] which is not seen in their XRD patterns. In addition, the reciprocal space map (RSM) near STO (002) peak has been collected and doesn't show any obvious twinned peaks. Thus the broad BFO peak indicates a large lattice parameter variation along its out-of-plane direction.

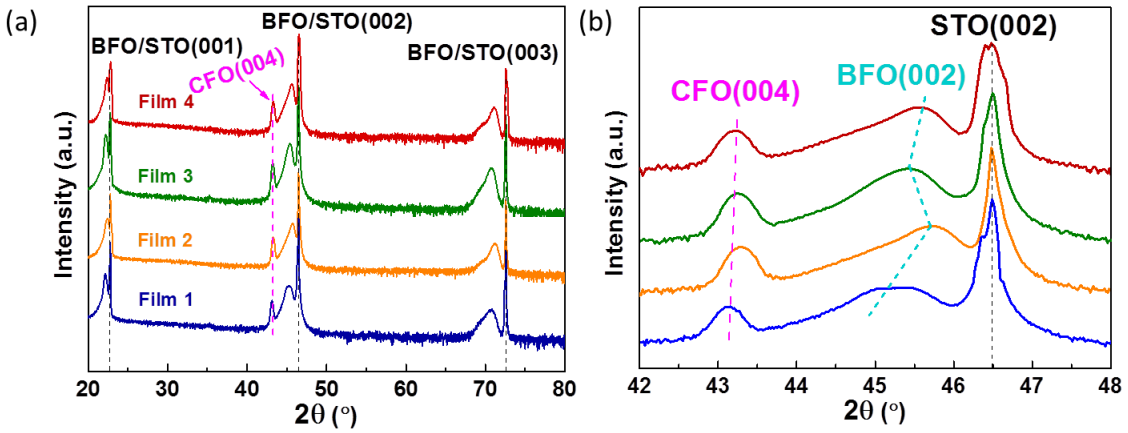

Figure 7.2. (a) Full θ-2θ XRD scans and (b) local scans near STO (002) of BFO:CFO VAN films with different deposition frequencies.

By measuring the lattice parameter variation, the peak spread in RSM provides a good estimation of the strain coupling/relaxation in VAN films. A large strain-induced lattice parameter variation can be seen from the broad BFO (103) RSM peak of Film 2 in Figure 7.3(a), compared to the much narrower peak in stiffer CFO. A more detailed comparison of the strain in BFO in different samples is presented in Figures 7.3(b). The BFO RSM peaks for Films 1 and 4 spread over a larger area than those with multiple

frequencies, indicating the important role of the heterointerface structure on the vertical strain accommodation. More detailed strain analysis results are summarized in Table 7.1.

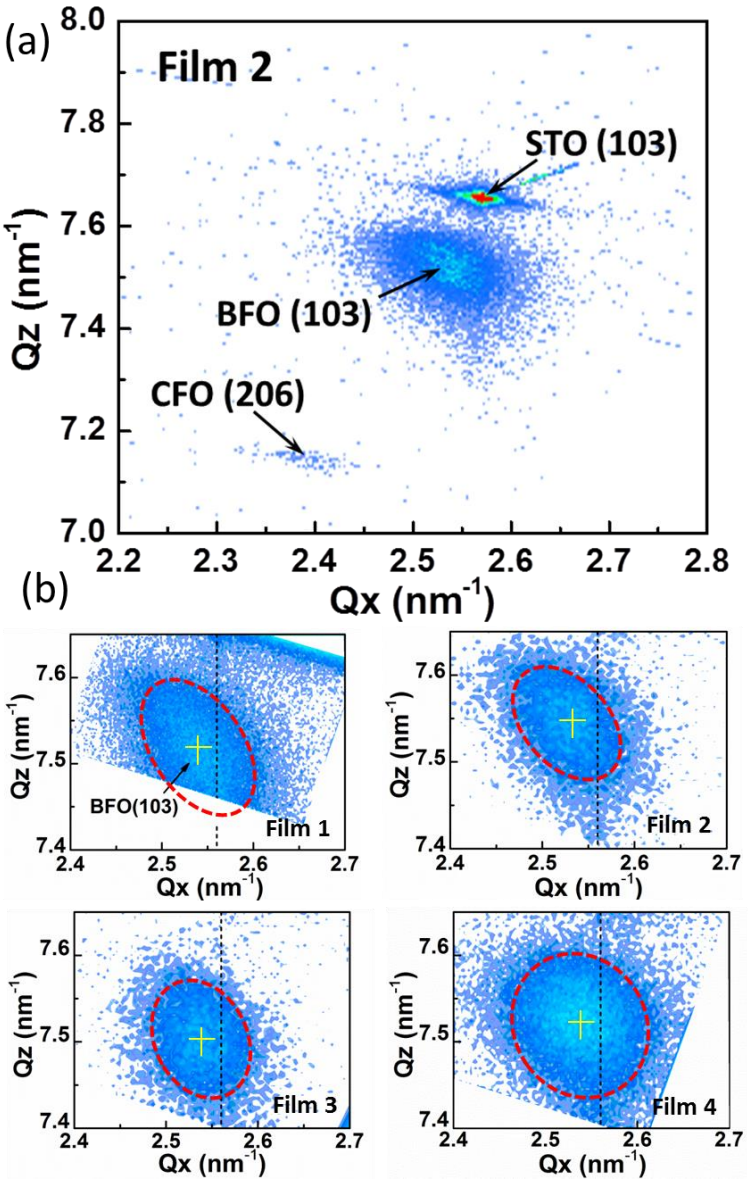

Figure 7.3. (a) Reciprocal space map (RSM) of Film 2 near the STO (103) peak. (b) RSM results of BFO (103) peak of all nanocomposite films.

Table 7.1 Growth parameters, microstructure and out-of-plane (OP) strain tuning in BFO:CFO VAN films deposited by different deposition frequencies

Film No.	Growth Sequence	Roughness Ra (nm)	Average CFO size (nm)	BFO (c/a) tetragonality	BFO-OP strain (%) (relaxed area; $Å^{-2}$) [a]	CFO-OP strain (%)
1	1Hz-30min	10.4	49	1.0175	0.85 (1.464)	-0.093 [b]
2	1st 1Hz-10min 2nd 2Hz-5min 3rd 10Hz-1min	9.71	66	1.0079	0.44 (1.120)	-0.48
3	1st 10Hz-1min 2nd 2Hz-5min 3rd 1Hz-10min	6.29	54	1.0158	1.01 (1.112)	-0.31
4	10Hz-3min	3.07	33	1.0163	0.69 (1.927)	-0.27

a) The strain-relaxed area is estimated from the marked ellipse region in RSM results.

b) The negative sign represents the compressive strain

7.5 Surface morphology of BFO:CFO VAN films

The film surface morphology has been investigated by scanning electron microscopy (SEM) and atomic force microscopy (AFM). Interestingly, very different surface features have been observed by tuning *f* through thickness. Figure 7.4(a) shows the top-view BSE image of Film 2 (10 Hz/2 Hz/1 Hz/STO). The inset in Fig. 2(a) shows that CFO becomes either square-like islands or irregular stripes surrounded by BFO. The AFM image in Figure 7.4(b) reveals similar morphology with a root mean square roughness (Ra) of 9.71 nm. Figure 7.4(c) shows the corresponding height profile. It is interesting to observe a stepped growth in CFO, and the stripes relate to the lower height. When *f* is reversed in Film 3 (1 Hz /2 Hz/10 Hz/STO), the film exhibits a well-defined morphology with highly ordered CFO nanopillars, as shown in Figures. 7.4(d) and 7.4(e).

Figure 7.4(f) shows a much sharper height variation with a smaller Ra of 6.29 nm. The BSE and AFM images of Films 1 (1 Hz) and 4 (10 Hz) are shown in Figures. 7.4(g-j). The disordered phase boundaries and the unexpected largest CFO pillar size in Film 2 can be attributed to a competition between interrupted atom diffusion with increased *f* and a tendency for nucleation of the same species to minimize surface energy. It is obvious that the morphology of this composite system depends strongly on growth conditions, similar to a previous report,[234] and CFO exchanges the role of matrix with BFO when grown at a higher laser energy density.[46]

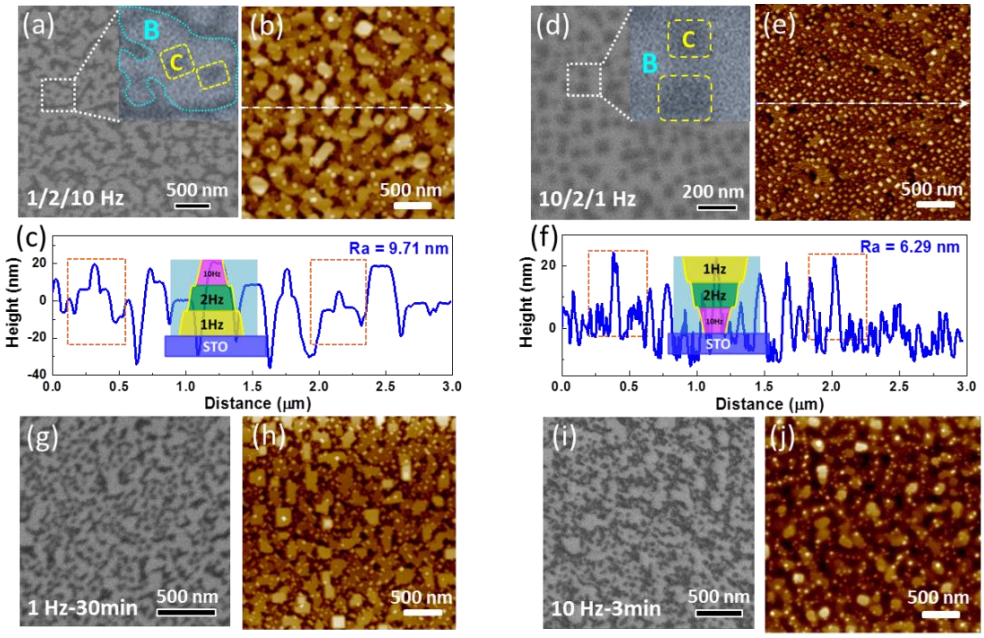

Figure 7.4. Top view SEM backscattered electron and AFM topography images of (a,b) Film 2, (d,e) Film 3, (g,h) Film 1 and (i,j) Film 4. Insets in Figs. 2(a) and 2(b) show the enlarged part of the film morphology. (c), (f) AFM height profiles along the line profiles in Figures. 7.4(b) and 7.4(e), respectively. Insets in Figures. 7.4(c) and 7.4(f) show the schematic heterointerface designs.

7.6 Microstructure and vertical interface of BFO:CFO VAN films

Figure 7.5(a) shows the cross-sectional scanning transmission electron microscopy ((S)TEM) image of Film 2. A continuously decreased column width in CFO has been observed. Conversely, when *f* was increased during growth (Film 3), the nanopillar width gradually increases (Fig. 7.5(b)). The gradient BFO:CFO heterointerface were further analyzed by Energy-dispersive X-ray spectroscopy (EDS) line scans in an area including two CFO nanopillars and BFO matrix in Film 2. Initially, CFO nanoislands were first grown on STO, forming a self-assembled seed layer (indicated by asterisk peaks in bottom EDS profile in Fig 7.5(c)). This layer acts as preferable nucleation sites for the following growth of CFO, resulting in more concentrated and cleaner Co signals observed in its middle and top scans. The larger CFO pillar on the left shows an obvious opposite composition trend of Co and Bi because of less isolated BFO islands interruption from bottom to top. However, for the smaller CFO pillar on the right, the composition variation between Bi and Co is less obvious, which is probably because the surrounding BFO matrix contributes to increased Bi signal with decreased nanopillar width. Figures. 7.5(d)-7.5(g) present the TEM images of a single CFO nanopillar embedded in BFO matrix from Films 1 to 4, which confirm the modulated heterointerfaces accomplished through tuning *f* in Figure 7.1.

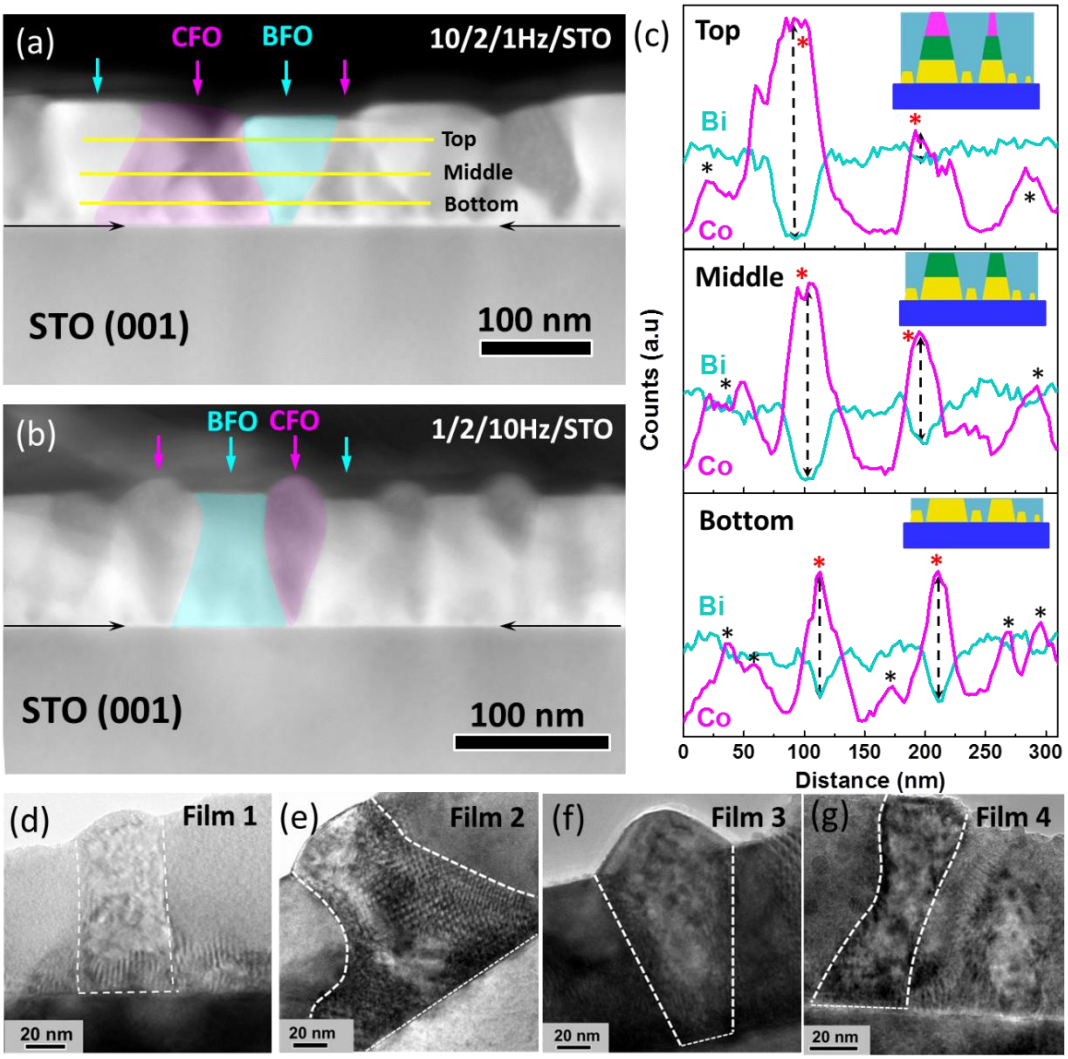

Figure 7.5.Cross-sectional STEM images of (a) Film 2 and (b) Film 3. (c) The EDS line profile across the top, middle and bottom regions in Fig. 3(a). (d)-(f) Cross-sectional TEM images of single CFO nanopillars in Films 1-4, respectively.

Compared to the vertical, clean interfaces in Films 1 and 4, moiré patterns and periodic lattice distortion have been observed at the gradient interfaces in Films 2 and 3. Figure 7.6 compares two types of interfaces using Film 3 and Film 4 as two presentative examples. In Film 3, the mismatch strain is partially relaxed by the periodic lattice

distortion of BFO at the vertical interface, which is seen from the formation of Moiré patterns (Figure 7.6(a)) and double diffraction characteristics in its FFT image (Figure 7.6(b)). On the other hand, the vertical interface of Film 4 shows a much cleaner lattice match between BFO and CFO (Figure 7.6(c)), which is also evidenced by the clear diffraction dots in the FFT image (Figure 7.6(d)). The above results indicate a highly strained state in Film 3 for BFO, which is partially relaxed by BFO lattice distortion at the BFO-CFO interface (the source of the mismatch strain). In Film 4, the mismatch strain is relaxed mainly by the overall lattice parameter variation, instead of local BFO lattice distortion. Therefore, a cleaner vertical interface (Figure 7.6(c)) and a large peak spread in RSM (Figure 7.3(b)) have been observed. Different interface structures and lattice mismatch strain accommodation have important effects on the magnetic and FE properties.

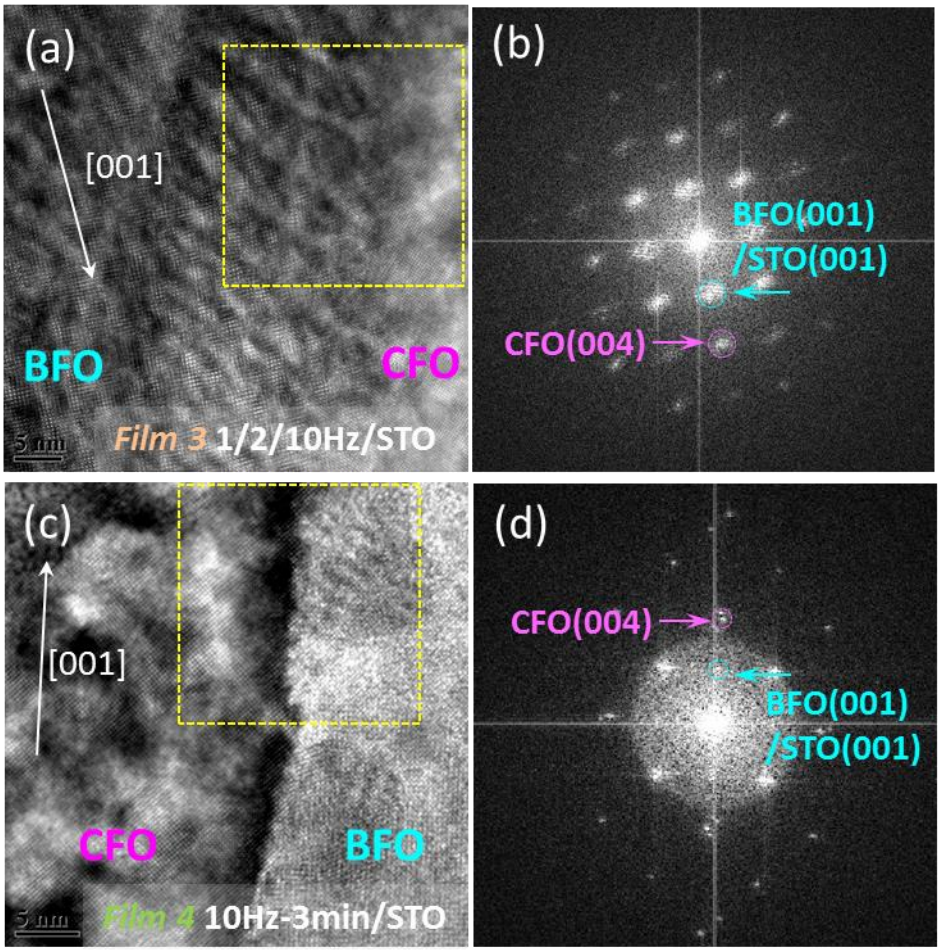

Figure 7.6. High resolution TEM images of the BFO-CFO interface of (a) Film 3 and (c) Film 4 showing different interface couplings. (b) and (d) Corresponding Fast Fourier transform (FFT) images of the marked area in (a) and (c), respectively.

7.7 Magnetic properties of BFO:CFO VAN films

The interface effect of magnetic properties of BFO:CFO VAN films have been measured first. Figures. 7.7(a) and 7.7(b) show the normalized out-of-plane (OP) and in-plane (IP) magnetic hysteresis (M-H) loops, respectively. Fig. 7.7(c) summarizes the coercive field (H_c) and the remanence to saturation magnetization ratios (M_r/M_s). Interestingly, the H_c in films deposited under single *f* are 1.3-3.4 times (for *in-plane*) and

1.6-1.8 times (for *out-of-plane*) larger than the ones under multiple *f*. The perpendicular anisotropy is gradually increased when *f* is decreased, as evidenced by the larger OP M_r/M_s ratios (from 49.4 % in Film 1 to 54.5 % in Film 4). Several important sources have been examined to explain the observed magnetic behavior. First, the magnetocrystalline anisotropy contributes equally to the OP and IP direction for the (00*l*)-oriented films. Second, CFO pillars introduce a shape anisotropy (K_s) favoring a perpendicular axis. K_s is calculated as $K_s = -2\pi(N_x - N_z)M_s^2$, where N_x and N_z are the demagnetization tensors, and $N_x = (1 - N_z)/2$.[54] CFO pillars are regarded as regular cylinders for a simplified estimation. For more accurate calculation of K_s of the less regular pillars in Films 2 and 3, we use the smallest and largest column width to calculate the range within which K_s varies. They have exhibited aspect ratios of 1.94, 1.06~1.77, 1.61~4.30, 3.03 and corresponding K_s values of (0.39, 0.16~0.42, 0.39~0.68, 0.64)$\times 10^6$ erg/cm^3 for Films 1-4, respectively.[235] Third, the magnetoelastic energy (K_{me}) is estimated by $K_{me} = -\frac{3}{2} \times \lambda_{001} \times \mathrm{Y} \times \varepsilon_{001}$, where λ_{001} is the magnetostrictive coefficient of CFO (~ -350×10^{-6}), and Y is the Young's modulus (~141.6 GPa).[54,192] The lattice strain on CFO is calculated from XRD results, which yields K_{me} of (0.69, 3.56, 2.32, 1.97)$\times 10^6$ erg/cm^3 for Films 1-4, respectively. Thus, the total anisotropy field (H_s) can be estimated by $H_s = 2K_{total}/M_s$, yielding H_s of 3.94 kOe,14.7~15.3 kOe, 10.0~10.3 kOe and 8.82 kOe for Films 1-4, respectively. The calculated H_s for Films 2 and 3 agrees well with the experimental observations (~10-15 kOe) to complete a saturate magnetization switching. It indicates a major role of combined shape and

magetoelastic anisotropy in controlling the magnetic behavior in films deposited under multiple *f*.

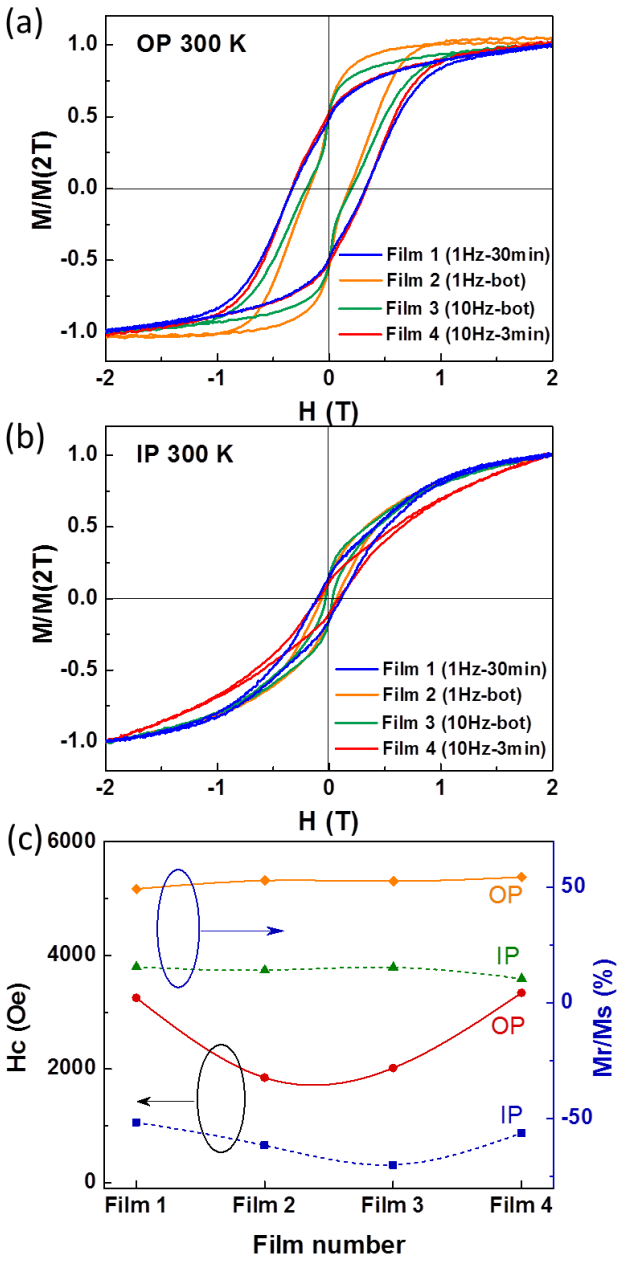

Figure 7.7. (a) Out-of-plane (OP) and (b) in-plane (IP) magnetic hysteresis loops of BFO:CFO VAN films. (c) Coercive fields (H_c) and remanence to saturation magnetization (M_r/M_s) ratios of the nanocomposite films.

For films deposited under single *f*, an extra anisotropy source is implied by much larger experimental H_s (~15-20 kOe) than calculated values (~3-8 kOe). This can be related to the spin exchange coupling between ferrimagnetic (FM) CFO and antiferromagnetic (AFM) BFO, which gives rise to a uniaxial anisotropy and coercivity enhancement.[56] To investigate the existence of such interaction, we measured the OP H_c of pure CFO films deposited at 1 Hz and 10 Hz, which shows that the H_c of BFO:CFO films is 4.1-11.5 times larger than the values of pure CFO films. The coupling effect is more pronounced in Films 1 and 4 with clean vertical heterointerfaces, which favors the uniaxial alignment of spin coupling and thus introduces the uniaxial anisotropy for enhanced H_c. In contrast, for Films 2 and 3, the significant lattice distortion at the gradient interfaces relaxes the spin coupling-induced anisotropy and results in the coexistence of exchange-coupled and non-coupled states. This leads to the kink behavior in their OP hysteresis loops.[212] Recent magnetization measurements comparing the individual CFO nanopillars and BFO:CFO coupled films also suggest the existence of the AFM-FM spin coupling.[236]

7.8 Ferroelectric properties of BFO:CFO VAN films

Local piezoelectric force microscopy (PFM) measurements were conducted to explore the heterointerface dependence of FE properties of BFO:CFO VAN films. Figures 7.8(a) and 7.8(b) show a PFM OP phase and amplitude image of Film 2, on which piezoresponse writing experiments were performed in a 0.8 x 0.8 μm^2 square area using +5 V bias followed by a central 0.4 x 0.4 μm^2 area using -5 V bias. The FE domain

switching is clearly seen in BFO matrix, while no phase contrast was observed in CFO because of its non-ferroelectric nature.

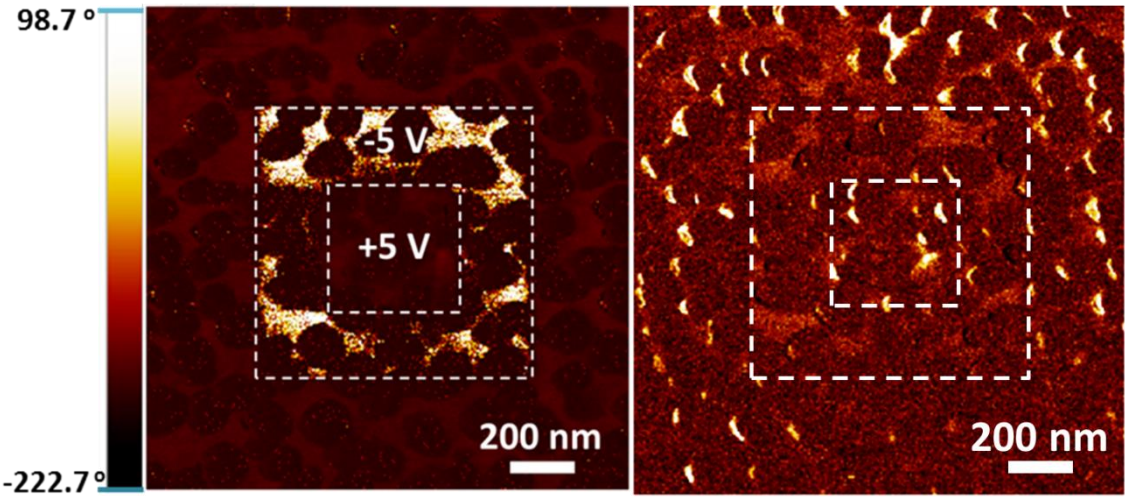

Figure 7.8. PFM (a) phase and (b) amplitude images of Film 2 after -5 V writing (0.8 x 0.8 μm^2) and +5 V rewriting (0.4 x 0.4 μm^2).

Figure 7.9 shows the phase and amplitude switching curves of all four films when the AFM tip was placed on BFO. Sharp phase switching by 180 ° is observed in all the films. The coercive electric fields for these films are 150-200 kV/cm, which is consistent with reported values for BFO films.[237,238] The slight asymmetry loop behavior could arise from the self-poling effect at the BFO/SRO interface or the internal built-in field effect in the film.[239] Interestingly, the amplitude in Film 3 exhibits ~2-fold enhancement of the piezoresponse at -3 V than that at -8 V (Figure 7.9(c)). This may be explained by the high tetragonal distortion in BFO (shown in Table I) which introduces an electric-field

induced rhombohedral-tetragonal mixed phase transformation corresponding to the kink change in its phase curve.[102,240] Films 1 and 4 exhibit a similar amplitude behavior to Film 3 but with a much larger hysteresis, which could be related to the larger strain relaxation and more gradual polarization switching in BFO. The phase switching direction is determined by the tip contact resonance frequency.

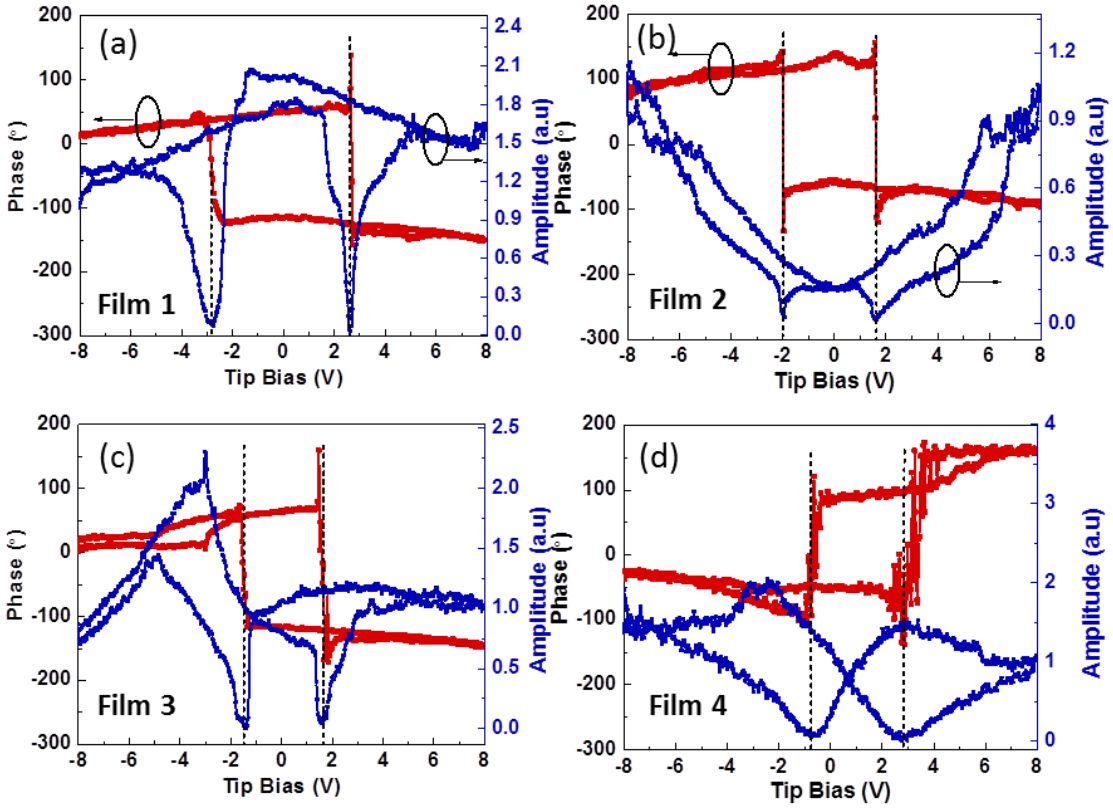

Figure 7.9. Phase and amplitude switching behavior as a function of tip bias of (a) Film 1 (b) Film 2, (c) Film 3 and (d) Film 4.

7.9 Summary

Both vertically straight and gradient heterointerfaces have been achieved by tuning deposition frequency through film thickness in BFO:CFO vertically aligned nanocomposite films. The strain and microstructure analysis reveals a strong dependence of the vertical strain tuning and heterointerface structure on the deposition frequency. The room-temperature magnetic anisotropy, coercive field and FE switching behavior are dominated by different mechanisms depending on the strain accommodation and interface coupling. The results demonstrate a promising approach in modulating the vertical heterointerface structure with tunable functionalities in heteroepitaxial vertical aligned nanocomposite films.

CHAPTER VIII

SUMMARY AND FUTURE WORK

In this dissertation, we systematically investigated the VAN architecture from the growth and interface control, to vertical strain tuning and interface coupling, as well as their effect on magnetotransport, magnetic anisotropy, exchange bias and FE properties. The VAN structure provides a versatile pathway to achieve enhanced and/or novel functionalities because of its simpler self-assembly, excellent structure compatibility in a variety of functional oxides, large vertical interfacial area and effective vertical strain tuning.

First, highly-textured LSMO:ZnO VAN films have been integrated on Si substrates with a bilayer STO/TiN buffer. The VAN films on Si have exhibited comparable LFMR results to those of films grown on single-crystal STO substrates, which provides an important step to enable the practical application of VAN films. Second, different types of magnetically coupled interfaces have been studied in BFO:CFO and BFO:LSMO VAN films. The enhanced perpendicular magnetic anisotropy has been obtained in BFO:CFO VAN films with significantly strain-relaxed interface. Detailed analysis indicates the spin-flop coupling at BFO-CFO interfaces introduces the observed enhanced anisotropy. In LSMO:BFO VAN films, the AFM-FM spin coupling at the vertical interface exhibits strong perpendicular exchange bias in micrometer-thick films. A systematic strain tuning has been achieved by varying the film composition, which affect the interface structure, AFM spin reorientation and magnetic

phase transition. Third, by employing the exchange coupling at the vertical LSMO-NiO interfaces, a dynamic and reversible control of the out-of-plane magnetotranport has been achieved, which provides a different way to study the magnetotransport property in VAN films along the vertical interface. Last, using BFO:CFO VAN system as an example, both vertical and gradient interfaces have been achieved by adjusting the film deposition frequency. The room-temperature magnetic anisotropy, coercive field and FE switching behavior of VAN films with different interfaces are dominated by different mechanisms depending on the strain accommodation and interface coupling.

VAN is a novel thin film platform with unique vertical interface coupling and strain tuning that can be used to achieve novel/enhanced multifunctionalities. Further research efforts are suggested to explore the following aspects:

(1) Fundamental growth mechanism. For example, can we come up with a general algorithm that guides the material selection for the growth of VAN structures either by nucleation and growth or by (pseudo-)spinodal decomposition? Can we integrate non-oxide materials and their additional wide-range functionalities in the VAN structure?

(2) Self-assembled or directed structure control. Can we achieve the exact control of VAN pillar size and interspacing in a long-range order by self-assembled or directed growth, and what are the limits on their length scales? Can we achieve a desired level of control of vertical interface defects and roughness for specific applications?

(3) Novel structure design. Can we integrate other nanostructure in the form of zero, one or two dimension to the VAN structure to further add functionality and tunability?

(4) Multifunctionality exploration. The coupling effect is not only limited in the ME and photomagnetic effects which have been demonstrated in VAN systems. Other parameters, including thermal and optical effect, can be explored for the mutually coupled multifunctionalities, such as thermoelectric, photochemical and so on.

(5) Interface effect. The structural discontinuity at the vertical semiconherent heterointerface of different phases in the VAN structure may generate a high concentration of structural disorders, such as misfit dislocations, grain and phases boundaries, which affects the electric and ionic transport, and in some cases the flux pinning properties in superconductors. Besides the transport performance, the interface effects on other related phenomena can be explored.

(6) Device integration. Can we incorporate the VAN structure in current devices or design new device structures based on the VAN architecture? This may require research efforts from the field of advanced device physics for the device application of the VAN structure.

REFERENCES

1. Bednorz, J. G.; Müller, K. A. *Z. Phys. Con. Mat.* **1986,** 64, 189-193.
2. Eerenstein, W.; Mathur, N. D.; Scott, J. F. *Nature* **2006,** 442, 759-765.
3. Ramirez, A. P. *J. Phys.: Condens. Matter* **1997,** 9, 8171.
4. Snyder, G. J.; Toberer, E. S. *Nat. Mater.* **2008,** 7, 105-114.
5. Garcia-Barriocanal, J.; Rivera-Calzada, A.; Varela, M.; Sefrioui, Z.; Iborra, E.; Leon, C.; Pennycook, S. J.; Santamaria, J. *Science* **2008,** 321, 676-680.
6. Catalan, G.; Scott, J. F. *Adv. Mater.* **2009,** 21, 2463-2485.
7. Ohtomo, A.; Hwang, H. Y. *Nature* **2004,** 427, 423-426.
8. Wang, J.; Neaton, J. B.; Zheng, H.; Nagarajan, V.; Ogale, S. B.; Liu, B.; Viehland, D.; Vaithyanathan, V.; Schlom, D. G.; Waghmare, U. V.; Spaldin, N. A.; Rabe, K. M.; Wuttig, M.; Ramesh, R. *Science* **2003,** 299, 1719-1722.
9. Martin, L. W.; Chu, Y. H.; Ramesh, R. *Mater. Sci. Eng., R* **2010,** 68, 89-133.
10. Benedek, N. A.; Rondinelli, J. M.; Djani, H.; Ghosez, P.; Lightfoot, P. *Dalton Trans.* **2015,** 44, 10543-10558.
11. Zener, C. *Phys. Rev.* **1951,** 82, 403-405.
12. Rao, C. N. R.; Raveau, B., *Transition metal oxides: structure, properties, and synthesis of ceramic oxides*. New York: Wiley-VCH, 2nd ed. 1998.
13. Thomson, W. *Proc. Royal Soc. London* **1856,** 8, 546-550.
14. Baibich, M. N.; Broto, J. M.; Fert, A.; Van Dau, F. N.; Petroff, F.; Etienne, P.; Creuzet, G.; Friederich, A.; Chazelas, J. *Phys. Rev. Lett.* **1988,** 61, 2472-2475.

15. Binasch, G.; Grünberg, P.; Saurenbach, F.; Zinn, W. *Phys. Rev. B* **1989,** 39, 4828-4830.

16. Alex-engraver, Spin vale with giant mangetoresistance. URL http://upload.wikimedia.org/wikipedia/commons/9/93/Spin-valve_GMR.svg. Accessed at September, **2015**.

17. Nesbet, R. K. *J. Phys.: Condens. Matter* **1994,** 6, L449.

18. Julliere, M. *Phys. Lett. A* **1975,** 54, 225-226.

19. Miyazaki, T.; Tezuka, N. *J. Magn. Magn. Mater*. **1995,** 139, L231-L234.

20. Chappert, C.; Fert, A.; Van Dau, F. N. *Nat. Mater*. **2007,** 6, 813-823.

21. Dexin, W.; Nordman, C.; Daughton, J. M.; Qian, Z.; Fink, J. *IEEE Trans. Magn.* **2004,** 40, 2269-2271.

22. Lee, Y. M.; Hayakawa, J.; Ikeda, S.; Matsukura, F.; Ohno, H. *Appl. Phys. Lett.* **2007,** 90, 212507.

23. Ikeda, S.; Hayakawa, J.; Ashizawa, Y.; Lee, Y. M.; Miura, K.; Hasegawa, H.; Tsunoda, M.; Matsukura, F.; Ohno, H. *Appl. Phys. Lett.* **2008,** 93, 082508.

24. Mao, S.; Yonghua, C.; Liu, F.; Xingfu, C.; Bin, X.; Puling, L.; Patwari, M.; Haiwen, X.; Clif, C.; Miller, B.; Menard, D.; Pant, B.; Loven, J.; Duxstad, K.; Li, S.; Zhengyong, Z.; Johnston, A.; Lamberton, R.; Gubbins, M.; McLaughlin, T.; Gadbois, J.; Ding, J.; Cross, B.; Song, X.; Ryan, P. *IEEE Trans. Magn.* **2006,** 42, 97-102.

25. Mangin, S.; Ravelosona, D.; Katine, J. A.; Carey, M. J.; Terris, B. D.; Fullerton, E. E. *Nat. Mater*. **2006,** 5, 210-215.

26. Ikeda, S.; Miura, K.; Yamamoto, H.; Mizunuma, K.; Gan, H. D.; Endo, M.; Kanai, S.; Hayakawa, J.; Matsukura, F.; Ohno, H. *Nat. Mater.* **2010,** 9, 721-724.

27. Gould, C.; Rüster, C.; Jungwirth, T.; Girgis, E.; Schott, G. M.; Giraud, R.; Brunner, K.; Schmidt, G.; Molenkamp, L. W. *Phys. Rev. Lett.* **2004,** 93, 117203.

28. Park, B. G.; Wunderlich, J.; Martí, X.; Holý, V.; Kurosaki, Y.; Yamada, M.; Yamamoto, H.; Nishide, A.; Hayakawa, J.; Takahashi, H.; Shick, A. B.; Jungwirth, T. *Nat. Mater.* **2011,** 10, 347-351.

29. Jonker, G. H.; Van Santen, J. H. *Physica* **1950,** 16, 337-349.

30. Haghiri-Gosnet, A. M.; Renard, J. P. *J. Phys. D: Appl. Phys.* **2003,** 36, R127.

31. Jahn, H. A.; Teller, E. *Proc. R. Soc. Lond. A: Math. Phys. Sci.* **1937,** 161, 220-235.

32. Ian , M. R.; Enrico , L. C.; Nava, S. *Jpn. J. Appl. Phys.* **1994,** 33, 3984.

33. Goodenough, J. B. *Phys. Rev.* **1955,** 100, 564-573.

34. Siwach, P. K.; Singh, H. K.; Srivastava, O. N. *J. Phys.: Condens. Matter* **2008,** 20, 273201.

35. de Gennes, P. G. *Phys. Rev.* **1960,** 118, 141-154.

36. Dagotto, E.; Hotta, T.; Moreo, A. *Phys. Rep.* **2001,** 344, 1-153.

37. Jin, S.; Tiefel, T. H.; McCormack, M.; Fastnacht, R. A.; Ramesh, R.; Chen, L. H. *Science* **1994,** 264, 413-415.

38. Subramanian, M. A.; Toby, B. H.; Ramirez, A. P.; Marshall, W. J.; Sleight, A. W.; Kwei, G. H. *Science* **1996,** 273, 81-84.

39. Varma, C. M. *Phys. Rev. B* **1996,** 54, 7328-7333.

40. Gupta, A.; Gong, G. Q.; Xiao, G.; Duncombe, P. R.; Lecoeur, P.; Trouilloud, P.; Wang, Y. Y.; Dravid, V. P.; Sun, J. Z. *Phys. Rev. B* **1996,** 54, R15629-R15632.

41. Uehara, M.; Mori, S.; Chen, C. H.; Cheong, S. W. *Nature* **1999,** 399, 560-563.

42. Gross, R.; Alff, L.; Büchner, B.; Freitag, B. H.; Höfener, C.; Klein, J.; Lu, Y.; Mader, W.; Philipp, J. B.; Rao, M. S. R.; Reutler, P.; Ritter, S.; Thienhaus, S.; Uhlenbruck, S.; Wiedenhorst, B. *J. Magn. Magn. Mater.* **2000,** 211, 150-159.

43. Mathur, N. D.; Burnell, G.; Isaac, S. P.; Jackson, T. J.; Teo, B. S.; MacManus-Driscoll, J. L.; Cohen, L. F.; Evetts, J. E.; Blamire, M. G. *Nature* **1997,** 387, 266-268.

44. Gupta, S.; Ranjit, R.; Mitra, C.; Raychaudhuri, P.; Pinto, R. *Appl. Phys. Lett.* **2001,** 78, 362-364.

45. Hueso, L. E.; Rivas, J.; Rivadulla, F.; López-Quintela, M. A. *J. Appl. Phys.* **2001,** 89, 1746-1750.

46. Zhang, W.; Jian, J.; Chen, A.; Jiao, L.; Khatkhatay, F.; Li, L.; Chu, F.; Jia, Q.; MacManus-Driscoll, J. L.; Wang, H. *Appl. Phys. Lett.* **2014,** 104, 062402.

47. Miyazaki, T.; Jin, H., *The physics of ferromagnetism*. Heidelberg; New York: Springer, 2012.

48. Gerrit van der, L. *J. Phys.: Condens. Matter* **1998,** 10, 3239.

49. Cullity, B. D.; Graham, C. D., *Introduction to magnetic materials.* Hoboken, N.J.: IEEE/Wiley, 2nd ed. 2009.

50. Limaye, M. V.; Singh, S. B.; Date, S. K.; Kothari, D.; Reddy, V. R.; Gupta, A.; Sathe, V.; Choudhary, R. J.; Kulkarni, S. K. *J. Phys. Chem. B* **2009,** 113, 9070-9076.

51. Berndt, L. M.; Balbarin, V.; Suzuki, Y. *Appl. Phys. Lett.* **2000,** 77, 2903-2905.

52. Brown, W. F., *Magnetostatic principles in ferromagnetism*. Amsterdam, North-Holland Pub. Co.; New York: Interscience Publishers, 1962.

53. Kusov, A. A.; Jaswal, S. S.; Shan, Z. S. *Phys. Rev. B* **1992,** 46, 3123-3124.

54. Zheng, H.; Kreisel, J.; Chu, Y.-H.; Ramesh, R.; Salamanca-Riba, L. *Appl. Phys. Lett.* **2007,** 90, 113113.

55. Zheng, H.; Wang, J.; Lofland, S. E.; Ma, Z.; Mohaddes-Ardabili, L.; Zhao, T.; Salamanca-Riba, L.; Shinde, S. R.; Ogale, S. B.; Bai, F.; Viehland, D.; Jia, Y.; Schlom, D. G.; Wuttig, M.; Roytburd, A.; Ramesh, R. *Science* **2004,** 303, 661-663.

56. Schulthess, T. C.; Butler, W. H. *Phys. Rev. Lett.* **1998,** 81, 4516-4519.

57. Miller, B. H.; Dahlberg, E. D. *Appl. Phys. Lett.* **1996,** 69, 3932-3934.

58. Koon, N. C. *Phys. Rev. Lett.* **1997,** 78, 4865-4868.

59. Meiklejohn, W. H.; Bean, C. P. *Phys. Rev.* **1956,** 102, 1413-1414.

60. Nogués, J.; Schuller, I. K. *J. Magn. Magn. Mater.* **1999,** 192, 203-232.

61. Fan, Y.; Smith, K. J.; LupkeG; Hanbicki, A. T.; GoswamiR; Li, C. H.; Zhao, H. B.; Jonker, B. T. *Nat. Nanotechnol.* **2013,** 8, 438-444.

62. Liu, K.; Baker, S. M.; Tuominen, M.; Russell, T. P.; Schuller, I. K. *Phys. Rev. B* **2001,** 63, 060403.

63. Nogués, J.; Sort, J.; Langlais, V.; Skumryev, V.; Suriñach, S.; Muñoz, J. S.; Baró, M. D. *Phys. Rep.* **2005,** 422, 65-117.

64. Nowak, U.; Usadel, K. D.; Keller, J.; Miltényi, P.; Beschoten, B.; Güntherodt, G. *Phys. Rev. B* **2002,** 66, 014430.

65. Kiwi, M. *J. Magn. Magn. Mater.* **2001,** 234, 584-595.

66. Meiklejohn, W. H. *J. Appl. Phys.* **1962,** 33, 1328-1335.

67. Berkowitz, A. E.; Takano, K. *J. Magn. Magn. Mater.* **1999,** 200, 552-570.

68. Ali, M.; Adie, P.; Marrows, C. H.; Greig, D.; Hickey, B. J.; Stamps, R. L. *Nat. Mater.* **2007,** 6, 70-75.

69. Gibert, M.; Zubko, P.; Scherwitzl, R.; Íñiguez, J.; Triscone, J.-M. *Nat. Mater.* **2012,** 11, 195-198.

70. Borisov, P.; Hochstrat, A.; Chen, X.; Kleemann, W.; Binek, C. *Phys. Rev. Lett.* **2005,** 94, 117203.

71. Lu, C.; Hu, W.; Tian, Y.; Wu, T. *Appl. Phys. Rev.* **2015,** 2, 021304.

72. Wu, S. M.; Cybart, S. A.; Yu, P.; Rossell, M. D.; Zhang, J. X.; Ramesh, R.; Dynes, R. C. *Nat. Mater.* **2010,** 9, 756-761.

73. Wu, S. M.; Cybart, S. A.; Yi, D.; Parker, J. M.; Ramesh, R.; Dynes, R. C. *Phys. Rev. Lett.* **2013,** 110, 067202.

74. Radu, F.; Abrudan, R.; Radu, I.; Schmitz, D.; Zabel, H. *Nat. Commun.* **2012,** 3, 715.

75. Maat, S.; Takano, K.; Parkin, S. S. P.; Fullerton, E. E. *Phys. Rev. Lett.* **2001,** 87, 087202.

76. Zhang, W.; Chen, A.; Jian, J.; Zhu, Y.; Chen, L.; Lu, P.; Jia, Q.; MacManus-Driscoll, J. L.; Zhang, X.; Wang, H. *Nanoscale* **2015,** 7, 13808-13815.

77. Ahn, C. H.; Rabe, K. M.; Triscone, J.-M. *Science* **2004,** 303, 488-491.

78. Cross, E. *Nature* **2004,** 432, 24-25.

79. Cochran, W. *Adv. Phys.* **1960,** 9, 387-423.

80. Kittel, C., *Introduction to solid state physics*. Hoboken, NJ: Wiley, 8th ed. 2005.

81. Ramesh, R.; Spaldin, N. A. *Nat. Mater.* **2007,** 6, 21-29.

82. Cheong, S.-W.; Mostovoy, M. *Nat. Mater.* **2007,** 6, 13-20.

83. Hill, N. A. *J. Phys. Chem. B* **2000,** 104, 6694-6709.

84. Ascher, E.; Rieder, H.; Schmid, H.; Stössel, H. *J. Appl. Phys.* **1966,** 37, 1404-1405.

85. Kimura, T.; Goto, T.; Shintani, H.; Ishizaka, K.; Arima, T.; Tokura, Y. *Nature* **2003,** 426, 55-58.

86. Ohring, M., *Materials science of thin films: deposition and structure*. San Diego, CA: Academic Press, 2nd ed. 2002.

87. Narayan, J.; Larson, B. C. *J. Appl. Phys.* **2003,** 93, 278-285.

88. Schlom, D. G.; Chen, L.-Q.; Fennie, C. J.; Gopalan, V.; Muller, D. A.; Pan, X.; Ramesh, R.; Uecker, R. *MRS Bull.* **2014,** 39, 118-130.

89. Schlom, D. G.; Chen, L.-Q.; Eom, C.-B.; Rabe, K. M.; Streiffer, S. K.; Triscone, J.-M. *Annu. Rev. Mater. Res.* **2007,** 37, 589-626.

90. Nguyen, L. D.; Brown, A. S.; Thompson, M. A.; Jelloian, L. M. *IEEE Trans. Electron. Devices* **1992,** 39, 2007-2014.

91. Ortuño-López, M. B.; Sotelo-Lerma, M.; Mendoza-Galván, A.; Ramírez-Bon, R. *Vacuum* **2004,** 76, 181-184.

92. Bozovic, I.; Logvenov, G.; Belca, I.; Narimbetov, B.; Sveklo, I. *Phys. Rev. Lett.* **2002,** 89, 107001.

93. Pertsev, N. A.; Tagantsev, A. K.; Setter, N. *Phys. Rev. B* **2000,** 61, R825-R829.

94. Beach, R. S.; Borchers, J. A.; Matheny, A.; Erwin, R. W.; Salamon, M. B.; Everitt, B.; Pettit, K.; Rhyne, J. J.; Flynn, C. P. *Phys. Rev. Lett.* **1993,** 70, 3502-3505.

95. Koukhar, V. G.; Pertsev, N. A.; Waser, R. *Phys. Rev. B* **2001,** 64, 214103.

96. Li, Y. L.; Hu, S. Y.; Liu, Z. K.; Chen, L. Q. *Appl. Phys. Lett.* **2001,** 78, 3878-3880.

97. Li, Y. L.; Choudhury, S.; Haeni, J. H.; Biegalski, M. D.; Vasudevarao, A.; Sharan, A.; Ma, H. Z.; Levy, J.; Gopalan, V.; Trolier-McKinstry, S.; Schlom, D. G.; Jia, Q. X.; Chen, L. Q. *Phys. Rev. B* **2006,** 73, 184112.

98. Li, Y. L.; Chen, L. Q. *Appl. Phys. Lett.* **2006,** 88, 072905.

99. Haeni, J. H.; Irvin, P.; Chang, W.; Uecker, R.; Reiche, P.; Li, Y. L.; Choudhury, S.; Tian, W.; Hawley, M. E.; Craigo, B.; Tagantsev, A. K.; Pan, X. Q.; Streiffer, S. K.; Chen, L. Q.; Kirchoefer, S. W.; Levy, J.; Schlom, D. G. *Nature* **2004,** 430, 758-761.

100. Choi, K. J.; Biegalski, M.; Li, Y. L.; Sharan, A.; Schubert, J.; Uecker, R.; Reiche, P.; Chen, Y. B.; Pan, X. Q.; Gopalan, V.; Chen, L.-Q.; Schlom, D. G.; Eom, C. B. *Science* **2004,** 306, 1005-1009.

101. Zeches, R. J.; Rossell, M. D.; Zhang, J. X.; Hatt, A. J.; He, Q.; Yang, C.-H.; Kumar, A.; Wang, C. H.; Melville, A.; Adamo, C.; Sheng, G.; Chu, Y.-H.; Ihlefeld, J. F.; Erni, R.; Ederer, C.; Gopalan, V.; Chen, L. Q.; Schlom, D. G.; Spaldin, N. A.; Martin, L. W.; Ramesh, R. *Science* **2009,** 326, 977-980.

102. Zhang, J. X.; XiangB; HeQ; SeidelJ; Zeches, R. J.; YuP; Yang, S. Y.; Wang, C. H.; Chu, Y. H.; Martin, L. W.; Minor, A. M.; Ramesh, R. *Nat. Nanotechnol.* **2011,** 6, 98-102.

103. Suzuki, Y.; Hwang, H. Y.; Cheong, S.-W.; van Dover, R. B. *Appl. Phys. Lett.* **1997,** 71, 140-142.

104. Chen, X. J.; Soltan, S.; Zhang, H.; Habermeier, H. U. *Phys. Rev. B* **2002,** 65, 174402.

105. Tokura, Y.; Nagaosa, N. *Science* **2000,** 288, 462-468.

106. Adamo, C.; Ke, X.; Wang, H. Q.; Xin, H. L.; Heeg, T.; Hawley, M. E.; Zander, W.; Schubert, J.; Schiffer, P.; Muller, D. A.; Maritato, L.; Schlom, D. G. *Appl. Phys. Lett.* **2009,** 95, 112504.

107. Yang, F.; Kemik, N.; Biegalski, M. D.; Christen, H. M.; Arenholz, E.; Takamura, Y. *Appl. Phys. Lett.* **2010,** 97, 092503.

108. Wang, B.; You, L.; Ren, P.; Yin, X.; Peng, Y.; Xia, B.; Wang, L.; Yu, X.; Mui Poh, S.; Yang, P.; Yuan, G.; Chen, L.; Rusydi, A.; Wang, J. *Nat. Commun.* **2013,** 4.

109. Nan, C.-W.; Bichurin, M. I.; Dong, S.; Viehland, D.; Srinivasan, G. *J. Appl. Phys.* **2008,** 103, 031101.

110. Wang, Y.; Hu, J.; Lin, Y.; Nan, C.-W. *NPG Asia Mater* **2010,** 2, 61-68.

111. Zavaliche, F.; Zheng, H.; Mohaddes-Ardabili, L.; Yang, S. Y.; Zhan, Q.; Shafer, P.; Reilly, E.; Chopdekar, R.; Jia, Y.; Wright, P.; Schlom, D. G.; Suzuki, Y.; Ramesh, R. *Nano Lett.* **2005,** 5, 1793-1796.

112. Lloréns, A.; Palau, A.; Gázquez, J.; Coll, M.; Vlad, R.; Pomar, A.; Arbiol, J.; Guzmán, R.; Ye, S.; Rouco, V.; Sandiumenge, F.; Ricart, S.; Puig, T.; Varela, M.; Chateigner, D.; Vanacken, J.; Gutiérrez, J.; Moshchalkov, V.; Deutscher, G.; Magen, C.; Obradors, X. *Nat. Mater.* **2012,** 11, 329-336.

113. Zhao, R.; Li, W.; Lee, J. H.; Choi, E. M.; Liang, Y.; Zhang, W.; Tang, R.; Wang, H.; Jia, Q.; MacManus-Driscoll, J. L.; Yang, H. *Adv. Funct. Mater.* **2014,** 24, 5240-5245.

114. Harrington, S.; Zhai, J.; Denev, S.; Gopalan, V.; Wang, H.; Bi, Z.; RedfernSimon, A. T.; Baek, S.-H.; Bark, C. W.; Eom, C.-B.; Jia, Q.; Vickers, M. E.; MacManus-Driscoll, J. L. *Nat. Nanotechnol.* **2011,** 6, 491-495.

115. Zheng, H.; Straub, F.; Zhan, Q.; Yang, P. L.; Hsieh, W. K.; Zavaliche, F.; Chu, Y. H.; Dahmen, U.; Ramesh, R. *Adv. Mater.* **2006,** 18, 2747-2752.

116. MacManus-Driscoll, J. L. *Adv. Funct. Mater.* **2010,** 20, 2035-2045.

117. Chen, A.; Bi, Z.; Jia, Q.; MacManus-Driscoll, J. L.; Wang, H. *Acta Mater.* **2013,** 61, 2783-2792.

118. Zhang, W.; Chen, A.; Bi, Z.; Jia, Q.; MacManus-Driscoll, J. L.; Wang, H. *Curr. Opin. Solid State Mater. Sci.* **2014,** 18, 6-18.

119. Liu, H.-J.; Liang, W.-I.; Chu, Y.-H.; Zheng, H.; Ramesh, R. *MRS Commun.* **2014,** 4, 31-44.

120. Zhang, W.; Ramesh, R.; MacManus-Driscoll, J. L.; Wang, H. *MRS Bull.* **2015,** 40, 736-745.

121. Lebedev, O. I.; Verbeeck, J.; Van Tendeloo, G.; Shapoval, O.; Belenchuk, A.; Moshnyaga, V.; Damashcke, B.; Samwer, K. *Phys. Rev. B* **2002,** 66, 104421.

122. MacManus-Driscoll, J. L.; Zerrer, P.; Wang, H.; Yang, H.; Yoon, J.; Fouchet, A.; Yu, R.; Blamire, M. G.; Jia, Q. *Nat. Mater.* **2008,** 7, 314-320.

123. Yang, H.; Wang, H.; Yoon, J.; Wang, Y.; Jain, M.; Feldmann, D. M.; Dowden, P. C.; MacManus-Driscoll, J. L.; Jia, Q. *Adv. Mater.* **2009,** 21, 3794-3798.

124. Bi, Z.; Lee, J. H.; Yang, H.; Jia, Q.; MacManus-Driscoll, J. L.; Wang, H. *J. Appl. Phys.* **2009,** 106, 094309.

125. Zavaliche, F.; Zhao, T.; Zheng, H.; Straub, F.; Cruz, M. P.; Yang, P. L.; Hao, D.; Ramesh, R. *Nano Lett.* **2007,** 7, 1586-1590.

126. Zhan, Q.; Yu, R.; Crane, S. P.; Zheng, H.; Kisielowski, C.; Ramesh, R. *Appl. Phys. Lett.* **2006,** 89, 172902.

127. Luo, H.; Yang, H.; Baily, S. A.; Ugurlu, O.; Jain, M.; Hawley, M. E.; McCleskey, T. M.; Burrell, A. K.; Bauer, E.; Civale, L.; Holesinger, T. G.; Jia, Q. *J. Am. Chem. Soc.* **2007,** 129, 14132-14133.

128. Chen, A.; Bi, Z.; Tsai, C.-F.; Lee, J.; Su, Q.; Zhang, X.; Jia, Q.; MacManus-Driscoll, J. L.; Wang, H. *Adv. Funct. Mater.* **2011,** 21, 2423-2429.

129. Kang, B. S.; Wang, H.; MacManus-Driscoll, J. L.; Li, Y.; Jia, Q. X.; Mihut, I.; Betts, J. B. *Appl. Phys. Lett.* **2006,** 88, 192514.

130. Chen, A.; Zhenxing, B.; Harshad, H.; Xinghang, Z.; Qing, S.; Li, C.; Quanxi, J.; Judith, L. M.-D.; Haiyan, W. *Nanotechnology* **2011,** 22, 315712.

131. Bi, Z.; Weal, E.; Luo, H.; Chen, A.; MacManus-Driscoll, J. L.; Jia, Q.; Wang, H. *J. Appl. Phys.* **2011,** 109, 054302.

132. Ning, X.; Wang, Z.; Zhang, Z. *Adv. Funct. Mater.* **2014,** 24, 5393-5401.

133. Ning, X.; Wang, Z.; Zhang, Z. *Adv. Mater. Inter.* **2015**, In press.

134. Levin, I.; Li, J.; Slutsker, J.; Roytburd, A. L. *Adv. Mater.* **2006,** 18, 2044-2047.

135. Cantoni, C.; Gao, Y.; Wee, S. H.; Specht, E. D.; Gazquez, J.; Meng, J.; Pennycook, S. J.; Goyal, A. *ACS Nano* **2011,** 5, 4783-4789.

136. Zhu, Y.; Tsai, C.-F.; Wang, J.; Kwon, J. H.; Wang, H.; Varanasi, C. V.; Burke, J.; Brunke, L.; Barnes, P. N. *J. Mater. Res.* **2012,** 27, 1763-1769.

137. Lee, S.; Sangle, A.; Lu, P.; Chen, A.; Zhang, W.; Lee, J. S.; Wang, H.; Jia, Q.; MacManus-Driscoll, J. L. *Adv. Mater.* **2014,** 26, 6284-6289.

138. Lee, S.; Zhang, W.; Khatkhatay, F.; Jia, Q.; Wang, H.; MacManus-Driscoll, J. L. *Adv. Funct. Mater.* **2015,** 25, 4328-4333.

139. Lee, O.; Harrington, S. A.; Kursumovic, A.; Defay, E.; Wang, H.; Bi, Z.; Tsai, C.-F.; Yan, L.; Jia, Q.; MacManus-Driscoll, J. L. *Nano Lett.* **2012,** 12, 4311-4317.

140. Liu, H.-J.; Chen, L.-Y.; He, Q.; Liang, C.-W.; Chen, Y.-Z.; Chien, Y.-S.; Hsieh, Y.-H.; Lin, S.-J.; Arenholz, E.; Luo, C.-W.; Chueh, Y.-L.; Chen, Y.-C.; Chu, Y.-H. *ACS Nano* **2012,** 6, 6952-6959.

141. Mohaddes-Ardabili, L.; Zheng, H.; Ogale, S. B.; Hannoyer, B.; Tian, W.; Wang, J.; Lofland, S. E.; Shinde, S. R.; Zhao, T.; Jia, Y.; Salamanca-Riba, L.; Schlom, D. G.; Wuttig, M.; Ramesh, R. *Nat. Mater.* **2004,** 3, 533-538.

142. Bonilla, F. J.; Novikova, A.; Vidal, F.; Zheng, Y.; Fonda, E.; Demaille, D.; Schuler, V.; Coati, A.; Vlad, A.; Garreau, Y.; Sauvage Simkin, M.; Dumont, Y.; Hidki, S.; Etgens, V. *ACS Nano* **2013,** 7, 4022-4029.

143. Su, Q.; Yoon, D.; Chen, A.; Khatkhatay, F.; Manthiram, A.; Wang, H. *Journal of Power Sources* **2013,** 242, 455-463.

144. Yoon, J.; Cho, S.; Kim, J.-H.; Lee, J.; Bi, Z.; Serquis, A.; Zhang, X.; Manthiram, A.; Wang, H. *Adv. Funct. Mater.* **2009,** 19, 3868-3873.

145. Cho, S.; Kim, Y. N.; Lee, J.; Manthiram, A.; Wang, H. *Electrochim. Acta* **2012,** 62, 147-152.

146. Winterbottom, W. L. *Acta Metall.* **1967,** 15, 303-310.

147. Ni, Y.; Khachaturyan, A. G. *Nat. Mater.* **2009,** 8, 410-414.

148. Park, S.; Horibe, Y.; Asada, T.; Wielunski, L. S.; Lee, N.; Bonanno, P. L.; O'Malley, S. M.; Sirenko, A. A.; Kazimirov, A.; Tanimura, M.; Gustafsson, T.; Cheong, S. W. *Nano Lett.* **2008,** 8, 720-724.

149. Ni, Y.; Rao, W.; Khachaturyan, A. G. *Nano Lett.* **2009,** 9, 3275-3281.

150. Wee, S. H.; Zuev, Y. L.; Cantoni, C.; Goyal, A. *Sci. Rep.* **2013,** 3, 2310.

151. Varanasi, C. V.; Burke, J.; Wang, H.; Lee, J. H.; Barnes, P. N. *Appl. Phys. Lett.* **2008,** 93, 092501.

152. Fix, T.; Choi, E.-M.; Robinson, J. W. A.; Lee, S. B.; Chen, A.; Prasad, B.; Wang, H.; Blamire, M. G.; MacManus-Driscoll, J. L. *Nano Lett.* **2013,** 13, 5886-5890.

153. Zhang, W.; Chen, A.; Khatkhatay, F.; Tsai, C.-F.; Su, Q.; Jiao, L.; Zhang, X.; Wang, H. *ACS Appl. Mater. Interfaces* **2013,** 5, 3995-3999.

154. Hsieh, Y.-H.; Liou, J.-M.; Huang, B.-C.; Liang, C.-W.; He, Q.; Zhan, Q.; Chiu, Y.-P.; Chen, Y.-C.; Chu, Y.-H. *Adv. Mater.* **2012,** 24, 4564-4568.

155. Aimon, N. M.; Choi, H. K.; Sun, X. Y.; Kim, D. H.; Ross, C. A. *Adv. Mater.* **2014,** 26, 3063-3067.

156. Choi, H. K.; Aimon, N. M.; Kim, D. H.; Sun, X. Y.; Gwyther, J.; Manners, I.; Ross, C. A. *ACS Nano* **2014,** 8, 9248-9254.

157. Kim, D. H.; Aimon, N. M.; Sun, X. Y.; Kornblum, L.; Walker, F. J.; Ahn, C. H.; Ross, C. A. *Adv. Funct. Mater.* **2014,** 24, 5889-5896.

158. Li, Y.; Wang, Z.; Yao, J.; Yang, T.; Wang, Z.; Hu, J.-M.; Chen, C.; Sun, R.; Tian, Z.; Li, J.; Chen, L.-Q.; Viehland, D. *Nat. Commun.* **2015,** 6, 6680.

159. Kawasaki, J. K.; Schultz, B. D.; Lu, H.; Gossard, A. C.; Palmstrøm, C. J. *Nano Lett.* **2013,** 13, 2895-2901.

160. Lu, H.; Ouellette, D. G.; Preu, S.; Watts, J. D.; Zaks, B.; Burke, P. G.; Sherwin, M. S.; Gossard, A. C. *Nano Lett.* **2014,** 14, 1107-1112.

161. Eason, R., *Pulsed laser deposition of thin films : applications-led growth of functional materials*. Hoboken, N.J.: Wiley-Interscience, 2007.

162. Warren, B. E., *X-ray diffraction*. Reading, Mass., Addison-Wesley Pub. Co. 1969.

163. Lee, W.; Han, S. H.; Jeong, H. *MOEMS* **2011,** 10, 023003-023003-7.

164. Reimer, L., *Scanning electron microscopy: physics of image formation and microanalysis*. Berlin; New York: Springer, 2nd ed. 1998.

165. Williams, D. B.; Carter, C. B., *Transmission electron microscopy. : a textbook for materials science*. New York: London: Springer, 2nd ed. 2009.

166. Eaton, P. J.; West, P., *Atomic force microscopy*. Oxford: Oxford University Press. 2010.

167. Salamon, M. B.; Jaime, M. *Rev. Mod. Phys.* **2001,** 73, 583-628.

168. Hambe, M.; Petraru, A.; Pertsev, N. A.; Munroe, P.; Nagarajan, V.; Kohlstedt, H. *Adv. Funct. Mater.* **2010,** 20, 2436-2441.

169. Yu, P.; Chu, Y.-H.; Ramesh, R. *Mater. Today* **2012,** 15, 320-327.

170. You, L.; Lu, C.; Yang, P.; Han, G.; Wu, T.; Luders, U.; Prellier, W.; Yao, K.; Chen, L.; Wang, J. *Adv. Mater.* **2010,** 22, 4964-4968.

171. Logvenov, G.; Gozar, A.; Bozovic, I. *Science* **2009,** 326, 699-702.

172. Weal, E.; Patnaik, S.; Bi, Z.; Wang, H.; Fix, T.; Kursumovic, A.; MacManus Driscoll, J. L. *Appl. Phys. Lett.* **2010,** 97, 153121.

173. Schlom, D. G.; Chen, L.-Q.; Pan, X.; Schmehl, A.; Zurbuchen, M. A. *J. Am. Ceram. Soc.* **2008,** 91, 2429-2454.

174. Wang, H.; Foltyn, S. R.; Arendt, P. N.; Jia, Q. X.; Li, Y.; Zhang, X. *Physica C Supercond.* **2005,** 433, 43-49.

175. Wang, J.; Zheng, H.; Ma, Z.; Prasertchoung, S.; Wuttig, M.; Droopad, R.; Yu, J.; Eisenbeiser, K.; Ramesh, R. *Appl. Phys. Lett.* **2004,** 85, 2574-2576.

176. Goh, W. C.; Yao, K.; Ong, C. K. *J. Appl. Phys.* **2005,** 97, 073905.

177. Kim, J.-H.; Khartsev, S. I.; Grishin, A. M. *Appl. Phys. Lett.* **2003,** 82, 4295-4297.

178. Balcells, L.; Carrillo, A. E.; Mart ńez, B.; Fontcuberta, J. *Appl. Phys. Lett.* **1999,** 74, 4014-4016.

179. Toker, D.; Azulay, D.; Shimoni, N.; Balberg, I.; Millo, O. *Phys. Rev. B* **2003,** 68, 041403.

180. Dubson, M. A.; Garland, J. C. *Phys. Rev. B* **1985,** 32, 7621-7623.

181. Imada, M.; Fujimori, A.; Tokura, Y. *Rev. Mod. Phys.* **1998,** 70, 1039-1263.

182. Yang, S. Y.; Kuang, W. L.; Liou, Y.; Tse, W. S.; Lee, S. F.; Yao, Y. D. *J. Magn. Magn. Mater.* **2004,** 268, 326-331.

183. Yan, L.; Kong, L. B.; Yang, T.; Goh, W. C.; Tan, C. Y.; Ong, C. K.; Rahman, M. A.; Osipowicz, T.; Ren, M. Q. *J. Appl. Phys.* **2004,** 96, 1568-1571.

184. Valencia, S.; Castaño, O.; Fontcuberta, J.; Martínez, B.; Balcells, L. *J. Appl. Phys.* **2003,** 94, 2524-2528.

185. Das, D.; Saha, A.; Russek, S. E.; Raj, R.; Bahadur, D. *J. Appl. Phys.* **2003,** 93, 8301-8303.

186. Gupta, A.; Sun, J. Z. *J. Magn. Magn. Mater.* **1999,** 200, 24-43.

187. Chen, A.; Zhang, W.; Jian, J.; Wang, H.; Tsai, C.-F.; Su, Q.; Jia, Q.; MacManus-Driscoll, J. L. *J. Mater. Res.* **2013,** 28, 1707-1714.

188. Chen, A.; Zhang, W.; Khatkhatay, F.; Su, Q.; Tsai, C.-F.; Chen, L.; Jia, Q. X.; MacManus-Driscoll, J. L.; Wang, H. *Appl. Phys. Lett.* **2013,** 102, 093114.

189. Chen-Fong, T.; Joon-Hwan, L.; Haiyan, W. *Supercond. Sci. Technol.* **2012,** 25, 075016.

190. Ma, J.; Hu, J.; Li, Z.; Nan, C.-W. *Adv. Mater.* **2011,** 23, 1062-1087.

191. Liao, S.-C.; Tsai, P.-Y.; Liang, C.-W.; Liu, H.-J.; Yang, J.-C.; Lin, S.-J.; Lai, C.-H.; Chu, Y.-H. *ACS Nano* **2011,** 5, 4118-4122.

192. Tsai, C. Y.; Chen, H. R.; Chang, F. C.; Tsai, W. C.; Cheng, H. M.; Chu, Y. H.; Lai, C. H.; Hsieh, W. F. *Appl. Phys. Lett.* **2013,** 102, 132905.

193. Meng, H.; Wang, J.-P. *Appl. Phys. Lett.* **2006,** 88, 172506.

194. Aimon, N. M.; Hun Kim, D.; Kyoon Choi, H.; Ross, C. A. *Appl. Phys. Lett.* **2012,** 100, 092901.

195. Comes, R.; Khokhlov, M.; Liu, H.; Lu, J.; Wolf, S. A. *J. Appl. Phys.* **2012,** 111, 07D914.

196. Dix, N.; Muralidharan, R.; Guyonnet, J.; Warot-Fonrose, B.; Varela, M.; Paruch, P.; Sanchez, F.; Fontcuberta, J. *Appl. Phys. Lett.* **2009,** 95, 062907.

197. McCord, J.; Mattheis, R.; Elefant, D. *Phys. Rev. B* **2004,** 70, 094420.

198. Chen, Y.-J.; Hsieh, Y.-H.; Liao, S.-C.; Hu, Z.; Huang, M.-J.; Kuo, W.-C.; Chin, Y.-Y.; Uen, T.-M.; Juang, J.-Y.; Lai, C.-H.; Lin, H.-J.; Chen, C.-T.; Chu, Y.-H. *Nanoscale* **2013,** 5, 4449-4453.

199. Dubowik, J. *Phys. Rev. B* **1996,** 54, 1088-1091.

200. Ohldag, H.; Scholl, A.; Nolting, F.; Arenholz, E.; Maat, S.; Young, A. T.; Carey, M.; Stöhr, J. *Phys. Rev. Lett.* **2003,** 91, 017203.

201. Choi, E.-M.; Weal, E.; Bi, Z.; Wang, H.; Kursumovic, A.; Fix, T.; Blamire, M. G.; MacManus-Driscoll, J. L. *Appl. Phys. Lett.* **2013,** 102, 012905.

202. Lebeugle, D.; Colson, D.; Forget, A.; Viret, M.; Bataille, A. M.; Gukasov, A. *Phys. Rev. Lett.* **2008,** 100, 227602.

203. Yu, P.; Lee, J. S.; Okamoto, S.; Rossell, M. D.; Huijben, M.; Yang, C. H.; He, Q.; Zhang, J. X.; Yang, S. Y.; Lee, M. J.; Ramasse, Q. M.; Erni, R.; Chu, Y. H.; Arena, D. A.; Kao, C. C.; Martin, L. W.; Ramesh, R. *Phys. Rev. Lett.* **2010,** 105, 027201.

204. Qiu, D. Y.; Ashraf, K.; Salahuddin, S. *Appl. Phys. Lett.* **2013,** 102, 112902.

205. Hwang, H. Y.; Iwasa, Y.; Kawasaki, M.; Keimer, B.; Nagaosa, N.; Tokura, Y. *Nat. Mater.* **2012,** 11, 103-113.

206. Gozar, A.; Logvenov, G.; Kourkoutis, L. F.; Bollinger, A. T.; Giannuzzi, L. A.; Muller, D. A.; Bozovic, I. *Nature* **2008,** 455, 782-785.

207. Xiao, D.; Zhu, W.; Ran, Y.; Nagaosa, N.; Okamoto, S. *Nat. Commun.* **2011,** 2, 596.

208. Valencia, S.; Crassous, A.; Bocher, L.; Garcia, V.; Moya, X.; Cherifi, R. O.; Deranlot, C.; Bouzehouane, K.; Fusil, S.; Zobelli, A.; Gloter, A.; Mathur, N. D.; Gaupp, A.; Abrudan, R.; Radu, F.; Barthélémy, A.; Bibes, M. *Nat. Mater.* **2011,** 10, 753-758.

209. Meiklejohn, W. H.; Bean, C. P. *Phys. Rev.* **1957,** 105, 904-913.

210. Skumryev, V.; Stoyanov, S.; Zhang, Y.; Hadjipanayis, G.; Givord, D.; Nogues, J. *Nature* **2003,** 423, 850-853.

211. Huijben, M.; Yu, P.; Martin, L. W.; Molegraaf, H. J. A.; Chu, Y. H.; Holcomb, M. B.; Balke, N.; Rijnders, G.; Ramesh, R. *Adv. Mater.* **2013,** 25, 4739-4745.

212. Zeng, H.; Li, J.; Liu, J. P.; Wang, Z. L.; Sun, S. *Nature* **2002,** 420, 395-398.

213. Rao, S. S.; Prater, J. T.; Wu, F.; Shelton, C. T.; Maria, J. P.; Narayan, J. *Nano Lett.* **2013,** 13, 5814-5821.

214. Bingham, N. S.; Phan, M. H.; Srikanth, H.; Torija, M. A.; Leighton, C. *J. Appl. Phys.* **2009,** 106.

215. Tsui, F.; Smoak, M. C.; Nath, T. K.; Eom, C. B. *Appl. Phys. Lett.* **2000,** 76, 2421-2423.

216. Fang, Z.; Solovyev, I. V.; Terakura, K. *Phys. Rev. Lett.* **2000,** 84, 3169-3172.

217. Camarero, J.; Sort, J.; Hoffmann, A.; Garcí a-Martí n, J. M.; Dieny, B.; Miranda, R.; Noguéś, J. *Phys. Rev. Lett.* **2005,** 95, 057204.

218. Tripathy, D.; Adeyeye, A. O. *Phys. Rev. B* **2009,** 79, 064413.

219. Gredig, T.; Krivorotov, I. N.; Dahlberg, E. D. *Phys. Rev. B* **2006,** 74, 094431.

220. Paul, A.; Buchmeier, M.; Bürgler, D. E.; Grünberg, P. *J. Appl. Phys.* **2005,** 97, 023910.

221. Gruyters, M. *J. Appl. Phys.* **2004,** 95, 2587-2592.

222. Gredig, T.; Krivorotov, I. N.; Dahlberg, E. D. *J. Appl. Phys.* **2002,** 91, 7760-7762.

223. Tripathy, D.; Vavassori, P.; Porro, J. M.; Adeyeye, A. O.; Singh, N. *Appl. Phys. Lett.* **2010,** 97, 042512.

224. Ding, J. F.; Lebedev, O. I.; Turner, S.; Tian, Y. F.; Hu, W. J.; Seo, J. W.; Panagopoulos, C.; Prellier, W.; Van Tendeloo, G.; Wu, T. *Phys. Rev. B* **2013,** 87, 054428.

225. Lu, Y.; Li, X. W.; Gong, G. Q.; Xiao, G.; Gupta, A.; Lecoeur, P.; Sun, J. Z.; Wang, Y. Y.; Dravid, V. P. *Phys. Rev. B* **1996,** 54, R8357-R8360.

226. Prasad, B.; Egilmez, M.; Schoofs, F.; Fix, T.; Vickers, M. E.; Zhang, W.; Jian, J.; Wang, H.; Blamire, M. G. *Nano Lett.* **2014,** 14, 2789-2793.

227. Chen, A.; Weigand, M.; Bi, Z.; Zhang, W.; Lu, X.; Dowden, P.; MacManus-Driscoll, J. L.; Wang, H.; Jia, Q. *Scientific Reports* **2014,** 4, 5426.

228. Imai, A.; Cheng, X.; Xin, H. L.; Eliseev, E. A.; Morozovska, A. N.; Kalinin, S. V.; Takahashi, R.; Lippmaa, M.; Matsumoto, Y.; Nagarajan, V. *ACS Nano* **2013,** 7, 11079-11086.

229. Hoffmann, J.; Schnittger, S.; Norpoth, J.; Raabe, S.; Kramer, T.; Jooss, C. *J. Mater. Res.* **2012,** 27, 1462-1470.

230. Wang, Z.; Li, Y.; Viswan, R.; Hu, B.; Harris, V. G.; Li, J.; Viehland, D. *ACS Nano* **2013,** 7, 3447-3456.

231. Wu, H.; Chai, G.; Zhou, T.; Zhang, Z.; Kitamura, T.; Zhou, H. *J. Appl. Phys.* **2014,** 115, 114105.

232. Shang, S. L.; Sheng, G.; Wang, Y.; Chen, L. Q.; Liu, Z. K. *Phys. Rev. B* **2009,** 80, 052102.

233. Fritsch, D.; Ederer, C. *Phys. Rev. B* **2010,** 82, 104117.

234. Dix, N.; Muralidharan, R.; Warot-Fonrose, B.; Varela, M.; Sánchez, F.; Fontcuberta, J. *Chem. Mater.* **2009,** 21, 1375-1380.

235. Bozorth, R. M.; Chapin, D. M. *J. Appl. Phys.* **1942,** 13, 320-326.

236. Wang, Z.; Viswan, R.; Hu, B.; Harris, V. G.; Li, J.-F.; Viehland, D. *Phys. Status Solidi RRL* **2012,** 6, 92-94.

237. Aimon, N. M.; Kim, D. H.; Sun, X.; Ross, C. A. *ACS Appl. Mater. Interfaces* **2015,** 7, 2263-2268.

238. Shelke, V.; Mazumdar, D.; Srinivasan, G.; Kumar, A.; Jesse, S.; Kalinin, S.; Baddorf, A.; Gupta, A. *Adv. Mater.* **2011,** 23, 669-672.

239. Barrionuevo, D.; Le, Z.; Ortega, N.; Sokolov, A.; Kumar, A.; Pankaj, M.; Scott, J. F.; Katiyar, R. S. *Nanotechnology* **2014,** 25, 495203.

240. Vasudevan, R. K.; Liu, Y.; Li, J.; Liang, W.-I.; Kumar, A.; Jesse, S.; Chen, Y.-C.; Chu, Y.-H.; Nagarajan, V.; Kalinin, S. V. *Nano Lett.* **2011,** 11, 3346-3354.